Title
Nanomachines on Porous Silica Nanoparticles for Cargo Delivery

Author
Tarn, Derrick

Publication Date
2013

Peer reviewed|Thesis/dissertation

UNIVERSITY OF CALIFORNIA

Los Angeles

Nanomachines on Porous Silica Nanoparticles for Cargo Delivery

A dissertation submitted in partial satisfaction

of the requirements for the degree

Doctor of Philosophy in Chemistry

by

Derrick Tarn

2013

ABSTRACT OF THE DISSERTATION

Nanomachines on Porous Silica Nanoparticles for Cargo Delivery

by

Derrick Tarn

Doctor of Philosophy in Chemistry

University of California, Los Angeles, 2013

Professor Jeffrey I. Zink, Chair

The field of nanomachines based on mesoporous and microporous silica nanoparticles is a relatively new one, but has quickly gained widespread popularity due to their large potential applications. These porous nanomaterials can both carry and release a therapeutic drug molecule at a targeted location. In order to regulate the movement of cargo, nanomachines are designed and assembled onto the silica nanoparticle, ultimately creating a delivery system on the nanoscale that is capable of a stimulus-responsive delivery of its cargo.

This dissertation focuses on the design, synthesis and assembly of nanomachines on both meso- and microporous silica nanoparticles to achieve the goal of cargo delivery. The six chapters of this dissertation are presented as follows: 1) the design, synthesis and modification of silica nanoparticles for their use in biology, 2) a light activated, reversible nanovalve assembled

on mesoporous silica nanoparticles to achieve a size-selective cargo delivery, 3) biological applications and the delivery of anti-cancer drugs using a pseudorotaxane-based light activated nanovalve, 4) a nanogate machine that is capable of the storage and delivery of both small metal ions and useful organic cargo molecules, 5) biological applications of the nanogate machine in order to deliver calcium ions to cancerous cells to induce cell apoptosis, and 6) thin wax coated microporous silica nanoparticles that are capable of delivering small ions including oxidizers.

The dissertation of Derrick Tarn is approved.

Heather D. Maynard

Fuyuhiko Tamanoi

Jeffrey I. Zink, Committee Chair

University of California, Los Angeles
2013

TABLE OF CONTENTS

Chapter 1	**Mesoporous Silica Nanoparticles as a Cargo Delivery Vehicle**	1
1.1	Silica Nanoparticles for Cargo Delivery	2
1.2	Introduction	4
	1.2.1 History of Mesoporous Silica Nanoparticles (MSN)	4
1.3	Synthetic Routes to Mesoporous Silica Nanoparticles	6
	1.3.1 Solution based synthesis of MSN	7
	1.3.2 Evaporation Induced Self-Assembly (EISA)	7
1.4	Methods of Modification	8
	1.4.1 Chemical Modification	8
	1.4.2 Co-condensation	8
	1.4.3 Post-synthetic grafting	8
	1.4.4 Surface Coating	9
1.5	Modified MSNPs for Biological Applications	9
	1.5.1 Imaging	10
	1.5.2 Dispersibility	10
	1.5.3 Targeting Specificity	11
	1.5.4 Cargo Loading and Delivery	12
1.6	Toxicity	13
	1.6.1 MSN Toxicity	13
1.7	Engineering MSNP to Store and Deliver Cargo	16
1.8	Figures	19
1.9	References	23

Chapter 2 A Reversible, Light-Operated Nanovalve on Mesoporous Silica Nanoparticles 32

2.1 Abstract 33

2.2 Introduction 34

2.3 Results and Discussion 36

2.3.1 Design of the nanovalves 36

2.3.2 Synthesis of MSN 38

2.3.3 Synthesis of the threads 38

2.3.4 Loading and sealing of cargo 39

2.3.5 Characterization 39

2.3.6 Operation of the machines 40

2.3.7 Light activated cargo delivery 41

2.3.8 FRS1 light activated release 41

2.3.9 EXT2 light activated release 43

2.4 Summary 45

2.5 Experimental 46

2.5.1 General Comments 46

2.5.2 Synthesis of MCM-41 Nanoparticles 46

2.5.3 Synthesis of 3-Aminopropyltriethoxysilane Modified MSN 47

2.5.4 Extraction of Templating Agent 47

2.5.5 Synthesis of 4,4'-Azobenzenecarboxylic acid 47

2.5.6 Synthesis of 2 48

2.5.7 Synthesis of 1-Adamantanecarbonyl chloride 48

2.5.8 Synthesis of 2b 49

2.5.9 Synthesis of 3a 50

2.5.10 Synthesis of 3b 50

2.5.11 Synthesis of 4a 51

2.5.12 Synthesis of 4b 51

2.5.13 Synthesis of FRS1 51

2.5.14 Synthesis of EXT2 51

2.5.15 Loading of Fluorescent Dye and Sealing in Cargo 52

2.5.16 Assessment of Light activated Cargo Release 52

2.5.17 Reloading and Reuse Assessment 53

2.6 Figures 54

2.7 References 75

Chapter 3 Application of a Pseudorotaxane-Based Azobenzene-Cyclodextrin Light Valve for the In Vitro Delivery of Doxorubicin and Hoechst 33342 79

3.1 Abstract 80

3.2 Introduction 81

3.3 Results and Discussion 82

3.3.1 Synthesis of TSUA MSN 82

3.3.2 *In Vitro* Release of Hoechst 33342 and Doxorubicin 83

3.4 Summary 86

3.5 Figures 87

3.6 References 93

Chapter 4 pH-Responsive Dual Cargo Delivery from Mesoporous Silica Nanoparticles with a Metal-latched Nanogate 96

4.1 Abstract 97

4.2 Introduction 98

4.3 Results and Discussion 99

4.3.1 Design of the Gate 99

4.3.2 Characterization 101

4.3.3 Loading and Release 101

4.3.4 Cobalt Latch 102

4.3.5 Acid Release 102

4.3.6 Competitive Binding Release 104

4.3.7 Nickel Latch 105

4.3.8 Calcium Latch 105

4.4 Summary 107

4.5 Experimental 108

4.5.1 General Comments 108

4.5.2 Synthesis of MCM-41 Nanoparticles 108

4.5.3 Extraction of Templating Agent 109

4.5.4 Synthesis of Dimethyl Iminodiacetate 109

4.5.5 Synthesis of (Dimethyl Iminodiacetate)propyltriethoxysilane 110

4.5.6 Synthesis of Dimethyl Iminodiacetate Modified Nanoparticles 110

4.5.7 Synthesis of Iminodiacetic Acid Modified Nanoparticles (IDA-MSN) 110

4.5.8 Loading of Hoechst 33342 111

4.5.9 Closing of the Nanogate and Loading of the Smaller Cargo 111

4.5.10 Assessment of the Cargo Release 111

4.5.11 pH Activation 112

4.5.12 Competitive Binding Activation 112

4.6 Figures 113

4.7 References 127

Chapter 5 *In Vitro* Delivery of Calcium Ions With Nanogated Mesoporous Silica Nanoparticles to Induce Cancer Cellular Apoptosis 131

5.1 Abstract 132

5.2 Introduction 133

5.3 Results and Discussion 134

5.3.1 Autonomous pH Activated Release of Cargo 134

5.3.2 Cell Killing with Calcium Delivery 134

5.3.3 Lysosomal Neutralization and Suppression of Cargo Release 135

5.4 Summary 136

5.5 Figures 137

5.6 References 142

Chapter 6 Coated Silicalite-1 Nanoparticles for the Controlled Delivery of Small Ions Including Oxidants 143

6.1 Abstract 144

6.2 Introduction 145

6.3 Results and Discussion 147

6.3.1 Synthesis of Silicalite-1 147

6.3.2 Loading of Cobalt 148

6.3.3 Choice of Surface Coating 148

6.3.4 Coating the Surface 149

6.3.5 Release of Cobalt 151

6.3.6 Release of $KClO_4$ 153

6.4 Summary 156

6.5 Experimental 157

6.5.1 General Comments 157

6.5.2 Synthesis of S1NP 157

6.5.3 Fluorescence Modification of S1NP 158

6.5.4 Removal of the Templating Agent 158

6.5.5 Rehydration of the S1NP Surface 158

6.5.6 Loading of Small Cargo 159

6.5.7 Coating with Paraffin Wax 159

6.5.8 Monitoring Release of Cobalt 159

6.5.9 Monitoring Release of Perchlorate 160

6.5.10 ICP-OES Measurement of Cobalt Release 160

6.5 Figures 161

6.6 References 180

ACKNOWLEDGEMENTS

There are many people who are responsible for getting me through this journey in graduate school. Without their continued support, suggestions and encouragement, I would never have been able to complete this dissertation. First and foremost I would like to thank my mentor, Dr. Jeffrey I. Zink for his continued support, guidance and teaching during my time here at UCLA. Thank you for teaching me how to apply the scientific thought process and for guiding me in producing solid science and ideas.

I am indebted to my committee members Prof. Richard B. Kaner, Prof. Heather D. Maynard and Prof. Fuyuhiko Tamanoi for serving on my oral exam committee and providing me valuable feedback as I advanced to candidacy, and for taking the time to both read and approve my dissertation.

I am fortunate to be blessed with the company of so many great minds, and the unique ways of thinking I have encountered in the Zink lab. I am grateful to have learned from all of my colleagues, and to have heard and taken part in their stories. To Dr. Courtney Thomas, thank you for your training my first year joining the Zink group. To Dr. Daniel Ferris, thank you your ongoing help ever since my first year here at UCLA. Thank you for training me and for getting me up to speed on silica sol-gel chemistry. I always enjoyed our conversations and discussions about science. It was a pleasure collaborating with you in the light valve experiments and azobenzene chemistry. Your perspectives on the world have always inspired me to remain hopeful towards science as a pure, politics-free entity. I look forward to both witnessing and taking part in great things you will accomplish. To Dr. Bryana Henderson and Dr. Yuen Lau, thank you both for our unique and insightful conversations. Thank you both for the constructive

feedback I have constantly received from you two over the years. To Dr. Sanaz Kabehie Gardner, thank you for your encouragement and for your genuinely caring attitude I have observed when we shared a lab office together. You taught me the importance of a positive outlook and attitude on life. Keep on being awesome, and congratulations again on your recent marriage! To Eunshil Choi, I am glad to be able to witness your transformation in coming back to UCLA. Thanks for being a part of my life here, and for your continued encouragement. I want to also acknowledge the visiting scholars that have contributed to my graduate school career—Arnaud Chaix and Sang-Wook Chu. Thank you for your invaluable help in the azobenzene light valve projects.

To the other group members of my year—Matt Kiesz, Tania Guardado, Melissa Russell and Min Xue, thank you for not only being encouraging friends to me, but for being great and brilliant minds that I can aspire towards. I am glad that we were able to share both our humble beginnings as graduate students our first year all the way to our graduation ceremonies. A special thanks to Min Xue, the colleague I have shared the lab office with for the last four years. It is an honor knowing someone who is as brilliant as you, but still willing to both help and teach others you. Thank you for all your lessons in general chemistry, for teaching me how to be a scientist and for teaching me the importance of hard work. I look forward to hearing about your great advances in the future and witnessing the number of lives you will inspire. To the younger students—Angela Hwang, Ivy Dong, Zilu Li and Janie Chen, thank you for your helpful discussions and for sharing part of my graduate experience with me. I know you guys will lead impactful lives in the future. I wish you guys the best of luck as you finish up your graduate school career.

I want to also thank my collaborators at CNSI— Dr. Haiyuan Zhang, Dr. Sijie Lin, Dr. Huan Meng, Dr. Zhaoxia Ji, and Dr. Chong Hyun Chang. Thank you for your willingness to try new ideas and experiments even if sometimes the result is somewhat unexpected. To Dr. Zhaoxia Ji, thank you for our discussions and for listening to my concerns. To Dr. Chong Hyun Chang, thank you again and again for your help with the ICP-OES instrument. Thank you for continually maintaining the instrument, troubleshooting with me if there are problems and suggestions when my results are ambiguous.

To my collaborators in the Stoddart group— Jonathan Barnes, Nathan L. Strutt, Dr. Michael W. Ambrogio, thank you for your work in synthesizing different azobenzene and/or alkoxysilane threads to create new nanomachines.

To my collaborators in the Tamanoi group— Dr. Jie Lu and Rolando Yanes, thank you for your continued work and conversations. To Rolando Yanes, thank you for your work in the cell exocytosis experiments. Dr. Jie Lu, thank you for both being a friend and collaborator, and for your willingness to try testing the more outlandish research ideas of mine. I learned much from you about life, biology, chemistry and medicine. I wish you the best of luck in your pursuit of a license to practice medicine in California.

In addition to those I have met while at UCLA, I want to thank my friends I have known outside of this program. To my old roommates Thomas Lin and Dennis Kuo, thank you for your encouragement during the lowest times of my career. Thanks for being both a friend and inspiration to me. Dennis Kuo, best of luck to you in your pursuit of a medical career; I know you will make a great doctor and save many lives. Thank you, Thomas Lin, for being a lifelong friend to me, and for your continued faith in me. I also want to thank Michael Liao for being a

friend and your continued support during my graduate school career. I am glad I was able to share my undergraduate chemistry experience with you here at UCLA. Best of luck in finishing up your graduate school studies in Arizona. I also want to thank Tiffany Lin for being a continued friend to me, and for your invaluable feedback in writing this dissertation. I want to thank Jessica Wong for her continued support, encouragement and belief in me. It has been a blessing to be part of your life, and to be able to walk by your side in our journey together.

To my parents, thank you again so much for your continued support of me in my pursuit of a PhD. Thank you for supporting me financially, emotionally, physically for all these years. Without you, I am nothing.

Lastly I want to thank my Lord and Savior Jesus Christ, for the strength and grace to get me this far in life. Without You, I would not be alive to write this today.

Soli Deo gloria.

VITA

2008	Bachelor of Science in Chemistry University of California Los Angeles, CA
2008	Ramsey Award, Excellence in Physical Chemistry
2008-2010, 2013	Teaching Assistant Department of Chemistry and Biochemistry University of California, Los Angeles
2010-2013	Research Assistant Zink Research Group University of California Los Angeles, CA

PUBLICATIONS

(1) **Tarn, D.**; Xue, M.; Zink, J. I. "pH-Responsive Dual Cargo Delivery from Mesoporous Silica Nanoparticles with a Metal-latched Nanogate." *Inorg. Chem.* **2013**, 52, 4, 2044-2049.

(2) **Tarn, D.**; Ashley, C. E.; Xue, M.; Carnes, E. C.; Zink, J. I.; Brinker, J. "Mesoporous Silica Nanoparticle Nanocarriers – Biofunctionality and Biocompatibility." *Acc. Chem. Res.* **2013**, 46, 792-801.

(3) Yanes, R. E.; **Tarn, D.**; Hwang, A. A.; Ferris, D. P.; Sherman, S. P.; Thomas, C. R.; Lu, J.; Pyle, A. D.; Zink, J. I.; Tamanoi, F. "Involvement of Lysosomal Exocytosis in the Excretion of Mesoporous Silica Nanoparticles and Enhancement of the Drug Delivery Effect by Exocytosis Inhibition." *Small* **2012**, 9, 697-704.

(4) Zhang, H.; Dunphy, D. R.; Jiang, X.; Meng, H.; Sun, B.; **Tarn, D.**; Xue, M.; Wang, X.; Lin, S.; Ji, Z.; Li, R.; Garcia, F. L.; Yang, J.; Kirk, M. L.; Xia, T.; Zink, J. I.; Nel, A. E.; Brinker, C. J. "Processing Pathway Dependence of Amorphous Silica Nanoparticle Toxicity: Colloidal vs Pyrolytic." *J. Am. Chem. Soc.* **2012**, 134, 15790-15804.

(5) Meng, H.; Xue, M.; Xia, T.; Ji, Z.; **Tarn, D.**; Zink, J. I.; Nel, A. E. "Use of Size and a Copolymer Design Feature To Improve the Biodistribution and the Enhanced Permeability and Retention Effect of Doxorubicin-Loaded Mesoporous Silica Nanoparticles in a Murine Xenograft Tumor Model." *ACS Nano* **2011**, 5, 4131–4144.

CHAPTER 1

Mesoporous Silica Nanoparticles as a Cargo Delivery Vehicle

1.1 Silica Nanoparticles for Cargo Delivery

The usefulness of silica is illustrated in its prevalence; it is a material that has found application in all facets of life. To be effective as a nanocarrier, silica must first be made into a well-defined, porous material. Recent advancements in the synthesis of mesoporous silica nanoparticles (MSN), including the ability to make them uniformly sized, porous, and dispersible using colloidal chemistry and evaporation-induced self-assembly has led to many applications of MSN as 'nanocarriers' for delivery of drugs and other cargos to cells. The exceptionally high surface area of MSN, often exceeding 1000 m^2/g, and ability to independently modify pore size and surface chemistry, enables the loading of diverse cargos and cargo combinations at levels exceeding those of other common drug delivery carriers such as liposomes or polymer conjugates. This is because non-covalent electrostatic, hydrogen-bonding and van der Waals interactions of the cargo with the MSN internal surface cause preferential adsorption of cargo to the MSN, allowing loading capacities to surpass the solubility limit of a solution or that achievable by osmotic gradient loading. The ability to independently modify the MSN surface and interior makes possible engineered bio-functionality and bio-compatibility.

In this thesis chapter (adopted from a recently published *Accounts of Chemical Research* review : Tarn, D.; Ashley, C. E.; Xue, M.; Carnes, E. C.; Zink, J. I.; Brinker, C. J. *Accounts* 2013, 46, 792-801), we detail our recent efforts to develop MSN as biocompatible nanocarriers (Figure 1.1) that simultaneously display multiple functions including: 1) high visibility/contrast in multiple imaging modalities, 2) dispersibility, 3) binding specificity to a particular target tissue or cell type, 4) ability to load and deliver large concentrations of diverse cargos, and 5) triggered/controlled release of cargo. Toward (1), we chemically conjugated fluorescent dyes or incorporated magnetic nanoparticles to enable in-vivo optical or magnetic resonance imaging.

For (2), we have made MSN with polymer coatings, charged groups or supported lipid bilayers, which decrease aggregation and improve stability in saline solutions. For (3) and (4), we have enhanced passive bioaccumulation via the enhanced permeability and retention effect by modifying the MSN surfaces with positively charged polymers. We have also chemically attached ligands to MSN that selectively bind to receptors over-expressed in cancer cells. Toward (4), we exploit the high surface area and tailorable surface chemistry of MSN to retain hydrophobic drugs. Finally, for (5), we have engineered dynamic behaviors by incorporating molecular machines within or at the entrances of MSN pores and by using ligands or polymers. These provide a means to seal-in and retain cargo and to direct MSN interactions with and internalization by target cells.

MSN's application as nanocarriers requires biocompatibility and low toxicity. Here the intrinsic porosity of the MSN surface reduces the extent of hydrogen bonding and/or electrostatic interactions with cell membranes as do surface coatings. Furthermore, the high surface area and low extent of condensation of the MSN siloxane framework promote a high rate of dissolution into soluble silicic acid species, which are found to be non-toxic. Potential toxicity is further mitigated by the high drug capacity of MSN, which greatly reduces needed dosages compared to other nanocarriers.

1.2 Introduction

1.2.1 History of Mesoporous Silica Nanoparticles (MSN)

In their classic paper, Kresge and co-workers[1] described a means of combining sol-gel chemistry with liquid-crystalline templating to create new classes of ordered porous molecular sieves characterized by periodic arrangements of uniformly sized mesopores (defined by IUPAC as pores with diameters between 2 and 50-nm) incorporated within an amorphous silica matrix. The first example of spherical MCM-41 developed by Grün and coworkers resulted in sub-μm spheres of MCM-41 and paved a path for its applications in biology in 1997.[2] Since the sub-micron material was still too large to be internalized by cells, MCM-41 needed to be further reduced in size in order to function as a drug delivery vehicle. In order to control the size and particle morphology, careful considerations of the ratio of surfactant, silica precursor,[3] temperature, stir speed,[4] and amount of base or acid catalyst must be made.[3] The mechanism of MCM-41 formation proposed by Davis and colleagues,[5] where a silicate layer is deposited on ordered, rod-like micelles and eventually arranged into a hexagonal phase with silica aging, suggests that the length and organization of these silica nanorods determines the overall particle aspect ratio and size. By changing the length of these silica nanorods, Cai et al. demonstrated that the packing of these longer nanorods leads to significantly larger primary particle sizes.[6] The addition of a co-surfactant can also stabilize packing of these nanorods, leading to nanomaterials with various aspect ratios.[7] Advances in morphology control were made by Lin and coworkers in 2003 by introducing an organoalkoxysilane group in a co-condensation method which stabilized shorter silica nanorods and resulted in nanometer sized materials (see synthetic routes to modification).[8] These 100-150 nm diameter well-ordered mesoporous spheres marked the beginnings of *in vitro* studies with a controlled delivery of antimicrobial drugs to E. coli K1

bacteria. Recently, it has been shown by Meng et al. that the use of co-surfactants and polymer coatings can achieve a MCM-41-type nanoparticle that is well-dispersed and 50-75 nm in diameter (see Stability section).[9] These materials have been shown to have an increased circulation time in animal models. In the past years, synthetic advances have been made to reduce the primary particle size of MCM-41 to 40 nm,[7] and MCM-41-like nanomaterials have been reported down to a 25 nm primary particle size.[10] The controlled synthesis of spherical and shaped mesoporous silica nanoparticles (MSN) has since been achieved by solution routes or by an aerosol-based evaporation induced self-assembly[11] (EISA) process (Gallery Figure 1.2), and the pore surfaces have been modified with a wide range of chemical moieties based mainly on silane coupling chemistries. Now there exist MSN with varied internal and external surface chemistries and quite sophisticated, environmentally responsive characteristics including optical or pH modulation of molecular transport.

A successful biocompatible nanocarrier must exhibit low toxicity combined with size uniformity, large capacity for diverse cargos, high traceability, colloidal stability, selective cell specific binding and internalization, and triggered cargo release. We show how specific, engineered chemical modifications of MSN result in functional and biocompatible nanocarriers (Figure 1.1). Both covalent modification and non-covalent encapsulation of MSN within polymers enable nanocarrier imaging in both *in vitro* and *in vivo* systems, dispersion stability in bio-relevant media, directed and cell specific uptake and internalization, high capacity loading and delivery of both hydrophilic and hydrophobic drugs.

1.3 Synthetic Routes to Mesoporous Silica

1.3.1 Solution based synthesis of MSN

The most widely used type of MSN is MCM-41, composed of ordered hexagonally arranged cylindrical mesopores.[1, 12] Since its introduction by the Mobil company as micrometer sized, amorphous aggregates, improved synthetic procedures enabled the formation of MCM-41 as successfully smaller particles with controlled shape: sub-μm spheres,[13] 100-150 nm nanoparticles suitable for *in vitro* studies,[14] mono-disperse 50-75 nm nanoparticles,[15] and recently, 25 nm MCM-41 like MSN.[16] The rapid progression of MCM-41 into a mono-disperse, <100 nm size MSN has been a close reflection of the emerging demand for a biocompatible, functional nanocarrier for biological applications.

The synthesis of MCM-41 involves liquid crystal templating using an alkylammonium salt, commonly cetyl trimethylammonium bromide (CTAB). In aqueous solution, above the critical micelle concentration, amphiphilic surfactant molecules self-assemble into spherical micelles and at higher concentrations, into periodic liquid crystal mesophases. Conducted in the presence of water and hydrophilic, soluble silica precursors (e.g., silicic acid, $Si(OH)_4$ or polysilicic acids), surfactant self-assembly results in hybrid nanocomposites. Through electrostatic and hydrogen bonding interactions, the silica precursors are concentrated at hydrophilic interfaces and condense to form an amorphous silica mold of the ordered periodic mesophase. Subsequent removal of the surfactant template by extraction or calcination results in the mesoporous product. The type of mesoporosity desired can be achieved by choosing a particular set of surfactants and/or varying the concentration. It is observed that the surfactant-water or surfactant-water-alcohol phase diagrams can largely be used to predict the corresponding silica mesophase, suggesting that their interaction with silicic acid species is

thermodynamically equivalent with water. Therefore, careful consideration of the micellular phases can illuminate the arrangement of the resultant silica mesopores.

Organization of the surfactant aggregates can be predicted by a model proposed by Israelachvili and colleagues, representing amphiphilic surfactant molecules as direct conical shape (ice cream cone).[17] Ultimately, the packing parameter g (as a function of the hydrophobic chain volume, the optimal polar head surface, and the length of the fully extended hydrophobic tail) determines the corresponding self-assembled micellular structure. It has been demonstrated that as the value of g increases, the mesopore motif for certain surfactants shows phase transitions from cubic, hexagonal, bicubic, and lamellar.[18, 19] These parameters have been applied to demonstrate a variety of mesoporous silica with a broad range of pore arrangements (Figure 1.2).

1.3.2 Evaporation Induced Self-Assembly (EISA)

EISA was established in 1997 as a means to direct the formation of continuous thin film mesophases via dip-coating.[20] EISA starts with a homogeneous solution of soluble silica and surfactant in ethanol/water with an initial surfactant concentration of co << cmc. Solvent evaporation during dip-coating or any evaporative process[11, 20, 21, 22] progressively increases surfactant concentration, driving self-assembly of silica/surfactant micelles and their further organization into liquid-crystalline mesophases. A logical extension of the EISA thin film process was to use aerosol processing to direct the formation of spherical mesoporous nanoparticles.[21] Compared to solution routes, a potential advantage of EISA is that any non-volatile component that can be introduced into an aerosol droplet is inevitably incorporated within the MSN, where the liquid-crystalline nature of the silica-surfactant mesophase allows the foreign object to be conformally encapsulated.

1.4 Methods of MSN Modification

1.4.1 Chemical Modification

MSN functionality can be introduced by modifying silanol groups present both within the pore interiors and the outer surface. These groups are chemically accessible and can be easily reacted with alkoxysilane derivatives to introduce organic functionality. Chemical moieties can also be adsorbed onto MSN, facilitated by the bond polarity of the Si-O bond, as a result of non-covalent electrostatic interactions (Figure 1.1). Generally, two main routes of modification exist: co-condensation, and post-synthetic grafting.

1.4.2 Co-condensation

The co-condensation method involves co-condensing hydrolyzed alkoxysilanes with organoalkoxysilanes ($R'_xSi(OR)_{4-x}$), which results in a directed modification of the interior pore surface.[23] The amphiphilic nature of the hydrolyzed organosilane allows it to serve as a cosurfactant that is incorporated into the surfactant micelle. As silica is condensed, the organoalkoxysilane is co-condensed positioning the organic moiety directly onto the pore walls.

An extension of the co-condensation method is the synthesis of MSN surrounding a metal or metal oxide nanoparticles in a core-shell architecture (Figure 1.2).[24] Core-shell MSN have seen many recent applications in theranostics – the combination of therapy and diagnostics.[25]

1.4.3 Post-synthetic grafting

A second method, post-synthetic grafting, involves modification of MSN after synthesis. This method employs surface accessible silanol groups both within the mesopore network as well as on the exterior MSN surfaces. Maximal surface coverage of interior mesopores is achieved via condensation with trifunctional organosilanes $R'Si(OR)_3$ in an organic solvent and produces a self-assembled monolayer.[26] To restrict/bias the deposition to the exterior surface of

the MSN, the modification can be performed prior to extracting the templating agent. The templating agent can then be removed, and the protected, unreacted silanol groups in the pore interiors can be further modified. In this way, functionalization can be directed. The various types of MSN modifications and their strategies for synthesis are summarized in Figure 1.3. Using these strategies, MSN can be engineered with functionalities to achieve specific bio-relevant properties.

1.4.4 Surface Coating

Introducing functional groups on the MSN exterior surface gives rise to additional surface properties. They can be further reacted as linkers to attach larger molecules or used to adsorb coatings through non-covalent interactions (Figures 1.1, 1.4). For the latter case, polymers are commonly employed on MSN.[15, 27, 28, 29] Due to the intrinsic negative charge of the silica surface resulting from deprotonation of surface silanols, bare nanoparticles can be electrostatically functionalized with a positively charged polymer. Polymers or other surface bound functional groups can also be used to retain cargo within the MSN.

1.5 Modified MSN for Biological Applications

A burgeoning area of MSN research has been their use as nanocarriers in biology.[30] Consequently, much of our present work has been directed towards tailoring MSN properties in order to improve their bio-functionality and bio-compatibility. To be effective and universally applicable, nanocarriers must *simultaneously* demonstrate multiple functions / characteristics including: 1) ease of imaging, 2) dispersibility, 3) specificity, 4) ability to load and deliver large concentrations of diverse cargos, and 5) biocompatibility/low toxicity. Their inherent high

surface area, versatile surface chemistry and low toxicity, confers to MSN the characteristics of an ideal nanocarrier platform.

1.5.1 Imaging

Direct imaging of MSN under bio-relevant conditions can be used to follow biodistribution, cancer cell targeting efficiency, internalization pathways, cytotoxicity, and the progress of therapy. MSN are multifunctional in that the core can be loaded or derivatized with fluorescent dyes, quantum dots, as well as therapeutic agents. Fluorescein isothiocyanate (FITC) and Rhodamine B isothiocyanate (RITC) are the most common fluorescent compounds that are incorporated into the MSN core. Near-IR dyes, such as AlexaFluor 700 and DyLight 680, have also been used in MSN for *in vivo* imaging. This type of fluorescent labeling is fairly robust and can be easily achieved. The resulting fluorescent MSN are capable of generating high-resolution, multi-channel images and can also provide quantitative data using flow cytometry techniques.[27]

Another relatively new method of imaging MSN is to incorporate magnetic nanoparticles e.g. magnetite Fe_3O_4 as cores of MSN, which allows T2-weighted MRI imaging.[27] Alternatively, T1-weighted imaging can be achieved using a chelated gadolinium compound.[31]

1.5.2 Dispersibility

For their use in biomedical applications, MSN must remain highly dispersed requiring colloidal stability. If aggregated, cell internalization suffers, biodistribution is difficult to control and larger effective particle sizes may lead to potentially higher toxicity (see MSN Toxicity). Particle agglomeration can be reduced by chemically modifying the surfaces,[32] introducing surface coatings with proteins and/or polymers,[15] and by coating with a supported lipid

bilayer. [33, 34, 35] These methods provide steric hindrance and electrostatic repulsion to achieve stable saline dispersions of MSN.

1.5.3 Targeting Specificity

To limit the degree of nonspecific binding while enhancing specific internalization by the target cell or tissue, MSN can be actively targeted towards an intended region. Despite the success in developing MSN that passively accumulate at the site of interest, active targeting also plays an important role in enhancing overall bioavailability. Passive targeting schemes rely on the enhanced permeability of tumor vasculature (the so-called enhanced permeability and retention (EPR) effect)[15] to direct accumulation of nanocarriers at tumor sites, but the lack of cell-specific interactions needed to induce nanocarrier internalization decreases therapeutic efficacy and can result in drug expulsion and induction of multiple drug resistance (MDR).[36] Selective targeting strategies employ ligands that specifically interact with receptors on the cell surface of interest to promote nanocarrier binding and internalization.[37] This strategy requires that receptors are highly overexpressed by cancer cells (10^4–10^5 copies/cell) relative to normal cells.

In terms of passive targeting, Xia et al demonstrated that cationic polymer (PEI) coating of MSN significantly facilitates their uptake.[28] Meng et al showed that through combined size-control and PEI/PEG copolymer coating, an enhanced EPR effect can be observed on a xenograft model.[15]

Active targeting employs ligands that bind specifically to receptors over-expressed on the cancer cell surface. Bio-active ligands, such as folate, RGD peptide and transferrin have been employed[38] due to their respective receptors being over-expressed on many different cancer cell types. In general, high specificity and binding affinity require a high concentration of surface

conjugated ligands to promote multivalent binding effects, which result in more efficient drug delivery through receptor-mediated internalization pathways (Figure 1.4).

1.5.4 Cargo Loading and Delivery

The high surface area and controllable chemistry of the MSN allow for simple loading of high concentrations[23, 34] of diverse classes and combination of cargos that can be delivered by endocytosis (Figure 1.4) or macropinocytosis. Early studies of drug delivery using MSN focused on drugs exhibiting low solubility in water, in particular, Ibuprofen and Aspirin.[39] Lu and Liong et al. later demonstrated the delivery of a hydrophobic chemotherapeutic agent, Camptothecin, into cancer cells using MSN.[32] The high interior volume and surface area of MSN allows hydrophobic compounds to be loaded into the pores from a non-aqueous solution and be retained in aqueous environments. When MSN are internalized through endocytosis (Figure 1.4), it is envisioned that lipid membrane components facilitate the phase-transfer of the stored hydrophobic payload enabling it to be gradually released.

When a hydrophilic cargo is involved, further modification of the MSN is often required. Meng and Liong et al. attached negatively charged groups onto MSN to enable the loading and retention of the positively charged hydrophilic drug, Doxorubicin (DOX).[29] Compared to FDA-approved Doxil, the Doxorubicin capacity in MSN can be nearly 1000-times greater due to the high surface area and attractive electrostatic interactions.[33]

For most nanocarrier delivery strategies, the cargo must be retained within the nanocarrier and released only upon delivery to the target cell. For MSN this generally requires that either the cargo be strongly adsorbed, as for DOX described above, or that the pores be 'sealed' after cargo loading. A method where quantum dots and small nanoparticles (caps) were used to block the entrance of pores was developed.[40] Numerous strategies have been

demonstrated where, by constructing a supramolecular nanovalve on the outer surface of MSN, one can achieve controlled release via a variety of stimuli, such as pH change, enzymatic ligand cleavage, light, and externally applied magnetic fields.[41, 42, 43, 44] Polymer coatings[45] have also been proven effective in sealing cargos within MSN.

1.6 Toxicity

1.6.1 MSN Toxicity

A critical issue for any nanocarrier application is nanoparticle toxicity. The toxicity of silicon dioxide, both crystalline and amorphous, has been studied for more than a century, especially as it relates to silicosis,[46, 47, 48, 49] and recently, the toxicity of silica nanoparticles has been extensively investigated, because the high surface to volume ratio of nanoparticles could lead to enhanced cellular interactions and different pathways of toxicity compared to coarse-grained silica.[15] In spite of hundreds of studies of the toxicity of amorphous and crystalline silicas,[46, 47, 48, 49] the mechanism(s) by which silica exposure leads to silicosis remain unclear, and literature reports are at times contradictory. Here it should be emphasized that *all silica are not created equal*. The amorphous silica framework and surface chemistry, in particular hydroxyl coverage[50] and size and distribution of siloxane rings that comprise the framework structure[51] can exhibit a wide range of configurations depending on processing conditions and environmental exposure. Consequently, there have been widely differing reports concerning the toxicity of MSN and amorphous silica in general.[16, 52, 53, 54] There is however, a general consensus that toxicity is associated in part with surface silanol (-SiOH) groups,[55] which can hydrogen bond to membrane components[56] or when dissociated to form SiO^- (above the isoelectric point of silica ~pH 2-3), interact electrostatically with the positively charged tetraalkylammonium-

containing phospholipids,[56] both processes leading to strong interactions, and possibly membranolysis. Such a process occurring at the cell surface could cause lysis, e.g. hemolysis, as shown for red blood cells.[16, 54, 56] Within a phagosome, damage to the membrane could cause release of hydrolytic enzymes from lysosomes into the cytoplasm. In support of the importance of silanols, it is known that treating the silica surface with polyvinylpyridine-N-oxide, aluminium salts, or surfactants can reduce or even switch-off hemolysis of red blood cells.[56] Based on the high surface to volume ratio of silica NPs, it might be anticipated that they would show in general higher toxicity compared to their bulk counterparts. However in the case of mesoporous silica NPs, the reduced solid fraction of the MSN surface serves to reduce the surface area normalized hydroxyl coverage, and therefore the extent of hydrogen bonding and electrostatic interactions between the MSN and the cell membrane.[55] Additionally, based on membrane curvature arguments, very small NPs are less likely to disrupt and/or become internalized by the cell membrane[55] because the membrane binding energy needed for the cell membrane to contact and fully envelop the NP scales quadratically with the NP curvature (1/diameter).

A second contribution to toxicity can be the reaction of radicals present on the silica surface with water to yield reactive oxygen species (ROS), in particular the hydroxy radical HO•, one of the most reactive species in nature.[57] ROS can cause cell death by disrupting cell membranes (necrosis) or initiating programmed cell death (apoptosis). In sublethal concentrations, ROS can upregulate production of cytokines and other inflammatory mediators and can promote mutagenesis and carcinogenesis. Although the ability of freshly ground crystalline silicas to serve as generators of ROS is generally recognized and has been linked to traces of iron suggesting a Fenton-like mechanism, the ability of iron-free and amorphous silicas to generate ROS is just beginning to be appreciated.[58] Here it is noteworthy that depending on

processing conditions, amorphous silicas can contain significant populations of strained three-membered siloxane rings.[51, 59] Strained siloxane rings could undergo homolytic cleavage to form surface associated radicals including the non-bridging oxygen hole center,[60] which react exothermically with water to form hydroxy radicals.[57] Whether, like defects generated by grinding of crystalline silica, strained 3-membered rings in amorphous silica could serve as ROS generators is a question we are currently addressing.[51] Notably, as-synthesized and surfactant-extracted MSN have a negligible concentration of three-membered rings.[51] For amorphous silica nanoparticles in general, dissolution results in monosilicic acid or oligosilicic acid which have been shown to have no intrinsic toxicity.[61]

Although based on numerous recent studies it is generally observed that MSN have much lower toxicity than corresponding non-porous silica colloids (Stöber silica or LUDOX), presumably due to the mesoporosity reducing the effective MSN/membrane contact area, conclusions concerning the role of particle size, shape, and charge are mixed. Notably Slowing et al[55] report reduced hemolysis of red blood cells, whereas Lin and Haynes[16] report increased hemolysis with decreasing MSN sizes over the range 25-260 nm diameters. Toxicity effects are also reported to be highly cell specific. Yu et al[54] show RAW264.7 macrophage cells to be more sensitive to ~115 nm solid or MSN than A549 cells, especially at very high doses of 250-500 μg/ml, and that solid Stöber silica colloids were more toxic and taken up into macrophage cells to a much greater extent than the corresponding MSN. Rationalization and unification of these varied findings requires a detailed understanding of possible internalization pathways. For endocytosis, membrane curvature arguments discussed above indicate that individual 50-60 nm diameter NPs should be most efficiently internalized as shown experimentally for targeted MSN.[33] Using spherical and rod-shaped MSN Meng et al[62] showed for HeLa and A549 cells that

particle shape (aspect ratio) is actively sensed and can stimulate efficient NP uptake by macropinocytosis in which multiple NPs are incorporated at once within pinosomes. Toxicity associated with both membrane damage and the fate of endocytosed or pinocytosed MSN must be clearly established and the role of NP aggregation on effective particle shape and membrane association or internalization elucidated.

The relevance of many recent MSN toxicity studies to *in vivo* applications of MSN may be questionable however as coating the MSN with polymers, lipid bilayers, or proteins (as could immediately occur *in vivo*) screens electrostatic interactions with surface silanols and is observed to effectively eliminate toxicity as demonstrated *in vivo*.[63] Additionally when considering drug delivery, we must bear in mind potential therapeutically administered doses. For example, for the hepatocellular carcinoma cell line Hep3B, the LC50 and LC90 values of free DOX are 150 ng/mL and 500 ng/mL, respectively. Those quantities could be delivered in 400 ng/mL and 1.3 ug/mL of MSN. As shown by Ashley et al,[33] when using targeted MSN, these values fall to 6 ng/mL and 20 ng/mL due to the MSN capacity, stability, and internalization efficiency. If only a few percent of MSN are delivered to the tumor microenvironment, relevant concentrations for the study of MSN toxicity are less than about 100 μg/ml, where most studies have shown insignificant toxicity.

1.7 Designing a System on MSN to Store and Deliver Cargo

The multifunctional modular design of MSN shown in Figure 1.1 suggests next generation nanocarriers where multicomponent cargos can be both stored and delivered to target cells through biologically triggered responses that actuate molecular valves. Synthesized MSN can be specifically engineered to store and deliver a variable cargo size triggered by either

internal modes of stimulation (pH change, enzymatic cleavage, redox chemistry) or external modes of activation (light irradiation, magnetic actuation). From here, we move on to discuss specific designs on silica nanoparticles to allow for the delivery both 1-2 nm sized organic molecules and small useful ions.

Chapter 2 discusses a redesign of a self-resealing azobenzene / α-cyclodextrin based nanovalve capable of an on / off response with light. Using this type of design, an all-or-nothing type of cargo release is achieved. Two azobenzene derivatized rotaxane threads were designed, synthesized and assembled onto MSN which show a size-selective cargo loading and delivery. The nanovalve is activated by light irradiation, where *trans*- to *cis*- photoisomerization of azobenzene causes α-cyclodextrin to slide away from the particle surface and allows cargo to release. Thermal relaxation of *trans*-azobenzene to *cis*-azobenzene allows for reformation of the α-cyclodextrin / azobenzene adduct and resealing of remaining cargo.

Chapter 3 is an ongoing application of a first-generation light activated nanovalve based on azobenzene / cyclodextrin (Ferris, D. P.; Zhao, Y.-L.; Khashab, N. M.; Khatib, H. A.; Stoddart, J. F.; Zink, J. I. *J. Am. Chem. Soc.* **2009**, 131, 1686-1688). The pseudorotaxane azobenzene / cyclodextrin nanovalve described in the *J. Am. Chem. Soc.* publication demonstrates the light-activated delivery of rhodamine B fluorescent dye. In this paper, β-cyclodextrin forms an adduct with the *trans*- isomer of azobenzene derivatized MSN. Upon light excitation, photoisomerization of *trans*- to *cis*-azobenzene unbinds the cyclodextrin macrocycle from the thread, allowing the loaded cargo molecules to release. Using this nanovalve, the light-activated delivery of Hoechst 33342 nuclear stain and an anti-cancer drug, Doxorubicin was demonstrated *in vitro*.

Chapter 4 is adapted from an article published in *Inorganic Chemistry* (Tarn, D.; Xue, M.; Zink, J. I. *Inorg. Chem.* **2013**, 52, 2044-2049). A system is designed, synthesized and assembled on MSN to allow it to deliver both chemotherapy sized organic molecules and small, biorelevant ions. By modifying iminodiacetic acid (IDA) and attaching it onto MSN, a nanogate is assembled in which two IDA moieties can be latched together to hold back cargo stored inside the MSN pores. Using this design, a dual-cargo release of Hoechst 33342 nuclear stain and transition metal ions cobalt, calcium and nickel were delivered.

Chapter 5 discusses ongoing biological applications of the IDA nanogate in collaboration with Dr. Jie Lu and Dr. Fuyuhiko Tamanoi. Here, we apply IDA modified MSN *in vitro*, and demonstrate the dual cargo delivery of both calcium and Hoechst to MiaPaCa-2 pancreatic cancer cells. IDA-MSN were found to be non-toxic to cells, and are shown to cause cancer cell death with delivery of calcium.

Chapter 6 illustrates a new method of introducing a surface coating on silicalite-1 (S1NP) to allow for its storage and delivery of both small cations and strong oxidizers. The zeolitic pore structure of S1NP allows for the loading of both cobalt and $KClO_4$. We introduce a new methodology for coating S1NP with a thin layer of chemically inert wax, which seals in the loaded cargo molecules. This wax coating is shown to be a thin layer (5 nm thickness) and is capable of sealing in the loaded cargo while being chemically inert against perchlorate. Upon melting the wax seal with heat, cargo can be made to release.

1.8 Figures

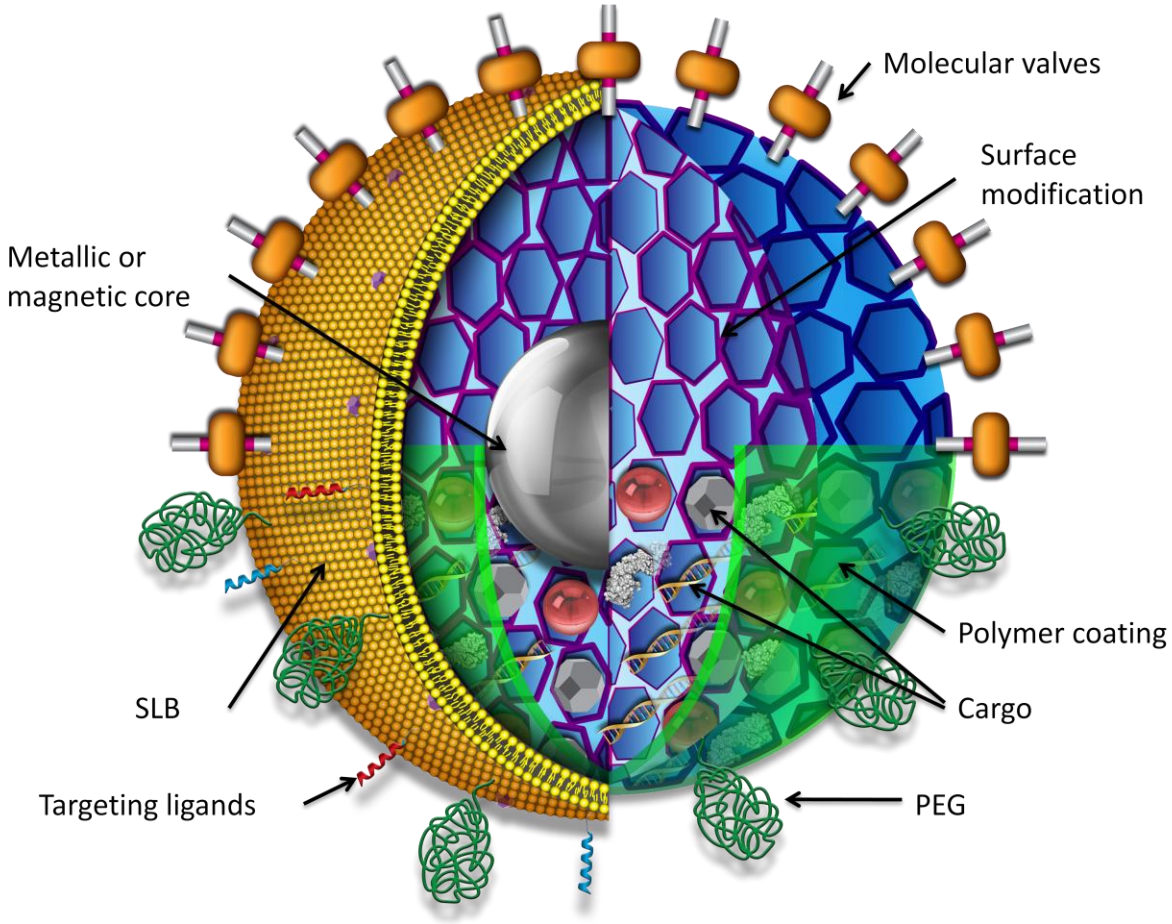

Figure 1.1. Schematic of a multifunctional mesoporous silica nanoparticle showing possible core/shell design, surface modifications, and multiple types of cargos.

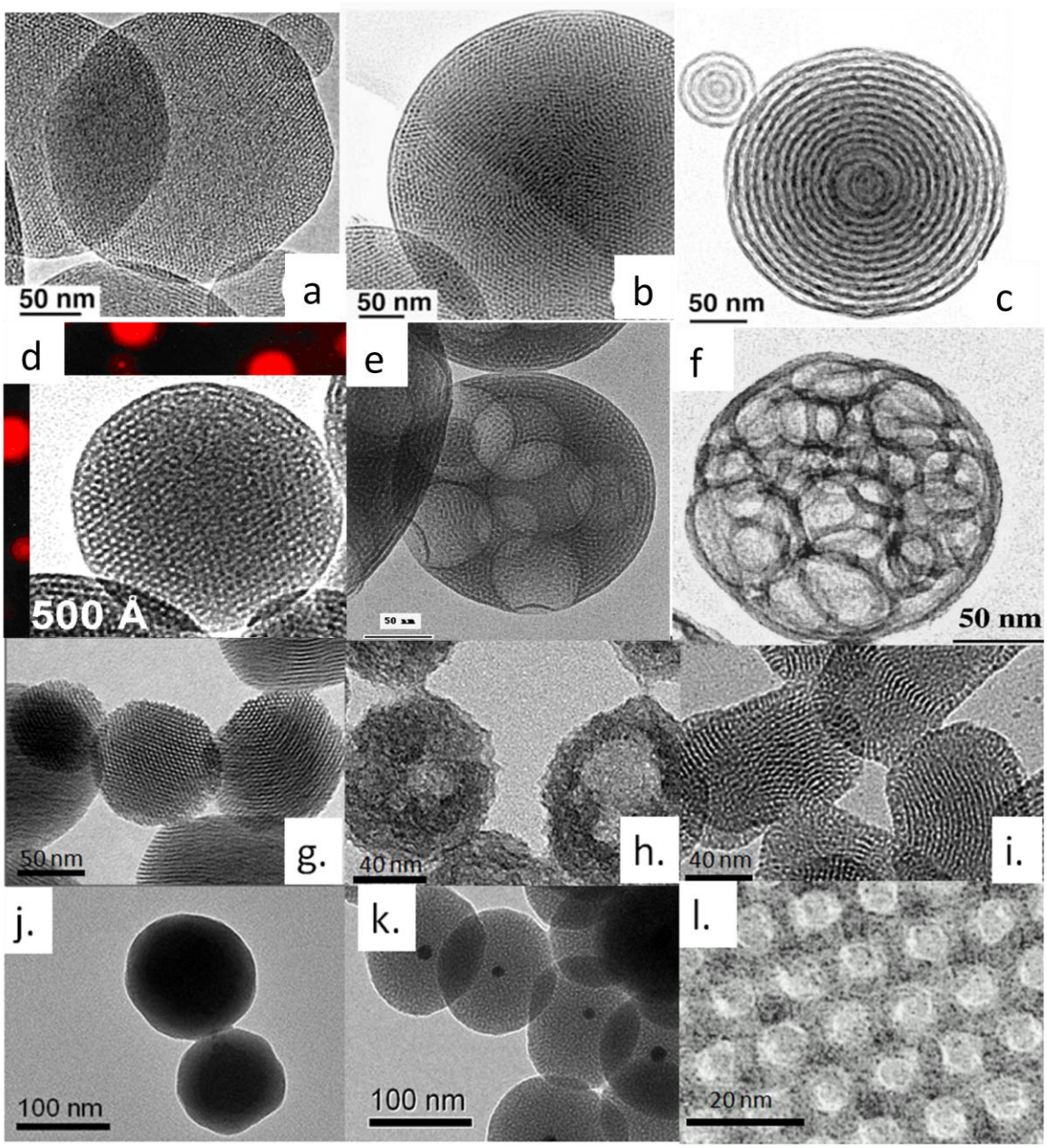

Figure 1.2. Gallery of mesoporous silica nanoparticles. Particles in a, b, c, and d are formed by EISA. Lower panel are solution prepared MSN.[10]

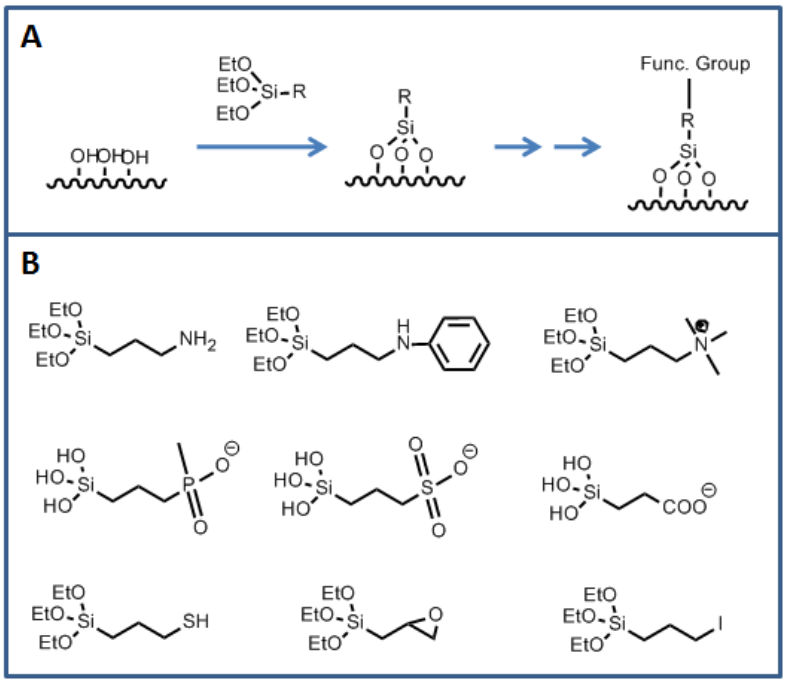

Figure 1.3. (a) Schematic showing reaction of surface silanol groups with an alkoxysilane linker to introduce functionality. (b) Various linkers to attach bio-molecules or to change the surface properties.

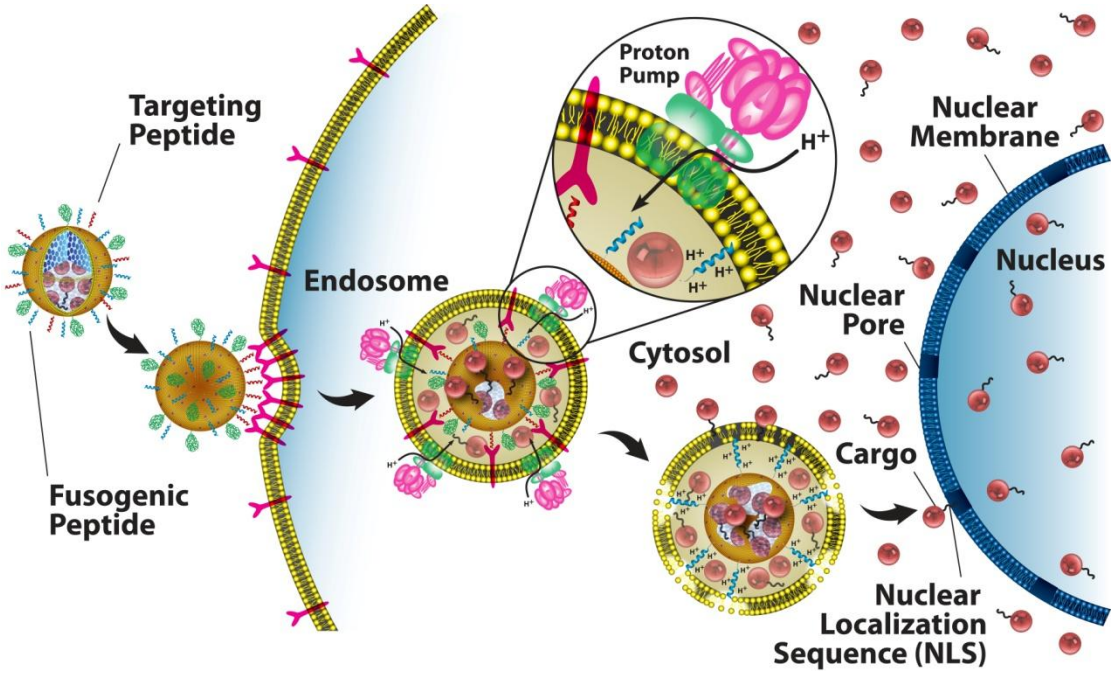

Figure 1.4. Schematic diagram depicting the successive steps of multivalent binding and internalization of MSN, followed by endosomal escape and nuclear localization of MSN-encapsulated cargo. (Adapted from ref. 33).

1.9 References

(1) Kresge, C. T.; Leonowicz, M. E.; Roth, W. J.; Vartuli, J. C.; Beck, J. S.: Ordered mesoporous molecular sieves synthesized by a liquid-crystal template mechanism. *Nature* **1992**, *359*, 710-712.

(2) Grün, M.; Lauer, I.; Unger, K. K.: The synthesis of micrometer- and submicrometer-size spheres of ordered mesoporous oxide MCM-41. *Advanced Materials* **1997**, *9*, 254-257.

(3) Soler-Illia, G. J. de A. A.; Sanchez, C.; Lebeau, B.; Patarin, J. Chem. Rev. 2002, 102, 4093-4138.

(4) Kumar, D.; Tiwari, N. P.; Pradeep, A. Ind. Eng. Chem. Res. 2002, 41, 6670-6677.

(5) Chen, C.-Y.; Burkett, S. L.; Li, H.-X; Davis, M. E. Microporous Mater. 1993, 2, 27.

(6) Cai, Q.; Luo, Z.-S.; Pang, W.-Q.; Fan, Y.-W.; Chen, X-H.; Cui, F.-Z. Chem. Mater. 2001, 13, 258-263.

(7) Zhu, J.; Wang, H.; Liao, L.; Zhao, L.; Zhou, L.; Yu, M.; Wang, Y.; Liu, B.; Yu, C. Chem. Asian. J. 2011, 6, 2332-2338.

(8) Huh, S.; Wiench, J. W.; Yoo, J.-C.; Pruski, M.; Lin, V. S. Y.: Organic Functionalization and Morphology Control of Mesoporous Silicas via a Co-Condensation Synthesis Method. *Chemistry of Materials* **2003**, *15*, 4247-4256.

(9) Meng, H.; Xue, M.; Xia, T.; Ji, Z.; Tarn, D. Y.; Zink, J. I.; Nel, A. E.: Use of Size and a Copolymer Design Feature To Improve the Biodistribution and the Enhanced Permeability and

Retention Effect of Doxorubicin-Loaded Mesoporous Silica Nanoparticles in a Murine Xenograft Tumor Model. *ACS Nano* **2011**, *5*, 4131-4144.

(10) Lin, Y-S.; Haynes, C. L. J. Am. Chem. Soc. 2010, 132, 4834-4842.

(11) Brinker, C. J.; Lu, Y. F.; Sellinger, A.; Fan, H. Y.: Evaporation-induced self-assembly: Nanostructures made easy. *Advanced Materials* **1999**, *11*, 579-585.

(12) Beck, J. S.; Vartuli, J. C.; Roth, W. J.; Leonowicz, M. E.; Kresge, C. T.; Schmitt, K. D.; Chu, C. T. W.; Olson, D. H.; Sheppard, E. W.: A new family of mesoporous molecular sieves prepared with liquid crystal templates. *Journal of the American Chemical Society* **1992**, *114*, 10834-10843.

(13) Grün, M.; Lauer, I.; Unger, K. K.: The synthesis of micrometer- and submicrometer-size spheres of ordered mesoporous oxide MCM-41. *Advanced Materials* **1997**, *9*, 254-257.

(14) Huh, S.; Wiench, J. W.; Yoo, J.-C.; Pruski, M.; Lin, V. S. Y.: Organic Functionalization and Morphology Control of Mesoporous Silicas via a Co-Condensation Synthesis Method. *Chemistry of Materials* **2003**, *15*, 4247-4256.

(15) Meng, H.; Xue, M.; Xia, T.; Ji, Z.; Tarn, D. Y.; Zink, J. I.; Nel, A. E.: Use of Size and a Copolymer Design Feature To Improve the Biodistribution and the Enhanced Permeability and Retention Effect of Doxorubicin-Loaded Mesoporous Silica Nanoparticles in a Murine Xenograft Tumor Model. *ACS Nano* **2011**, *5*, 4131-4144.

(16) Lin, Y.-S.; Haynes, C. L.: Impacts of Mesoporous Silica Nanoparticle Size, Pore Ordering, and Pore Integrity on Hemolytic Activity. *Journal of the American Chemical Society* **2010**, *132*, 4834-4842.

(17) Israelachvili, N.; Mitchell, D. J.; Niham, B. W.; J. Chem. Soc., Faraday Trans. 2 1976, 72, 1525.

(18) Landry, C. C.; Tolbert, S. H.; Gallis, K. W.; Monnier, A.; Stucky, G. D.; Norby, P.; Hanson, J. C. Chem Mater. 2001, 13, 1600.

(19) Huo, Q.; Leon, R.; Petroff, P. M.; Stucky, G. D. Science 1995, 268, 1324.

(20) Lu, Y. F.; Ganguli, R.; Drewien, C. A.; Anderson, M. T.; Brinker, C. J.; Gong, W. L.; Guo, Y. X.; Soyez, H.; Dunn, B.; Huang, M. H.; Zink, J. I.: Continuous formation of supported cubic and hexagonal mesoporous films by sol gel dip-coating. *Nature* **1997**, *389*, 364-368.

(21) Fan, H. Y.; Lu, Y. F.; Stump, A.; Reed, S. T.; Baer, T.; Schunk, R.; Perez-Luna, V.; Lopez, G. P.; Brinker, C. J.: Rapid prototyping of patterned functional nanostructures. *Nature* **2000**, *405*, 56-60.

(22) Lu, Y. F.; Fan, H. Y.; Stump, A.; Ward, T. L.; Rieker, T.; Brinker, C. J.: Aerosol-assisted self-assembly of mesostructured spherical nanoparticles. *Nature* **1999**, *398*, 223-226.

(23) Li, Z.; Nyalosaso, J. L.; Hwang, A. A.; Ferris, D. P.; Yang, S.; Derrien, G.; Charnay, C.; Durand, J.-O.; Zink, J. I.: Measurement of Uptake and Release Capacities of Mesoporous Silica Nanoparticles Enabled by Nanovalve Gates. *The Journal of Physical Chemistry C* **2011**, *115*, 19496-19506.

(24) Kim, J.; Kim, H. S.; Lee, N.; Kim, T.; Kim, H.; Yu, T.; Song, I. C.; Moon, W. K.; Hyeon, T.: Multifunctional Uniform Nanoparticles Composed of a Magnetite Nanocrystal Core and a Mesoporous Silica Shell for Magnetic Resonance and Fluorescence Imaging and for Drug Delivery. *Angewandte Chemie International Edition* **2008**, *47*, 8438-8441.

(25) Thomas, C. R.; Ferris, D. P.; Lee, J.-H.; Choi, E.; Cho, M. H.; Kim, E. S.; Stoddart, J. F.; Shin, J.-S.; Cheon, J.; Zink, J. I.: Noninvasive Remote-Controlled Release of Drug Molecules in Vitro Using Magnetic Actuation of Mechanized Nanoparticles. *Journal of the American Chemical Society* **2010**, *132*, 10623-10625.

(26) Feng, X.; Fryxell, G. E.; Wang, L.-Q.; Kim, A. Y.; Liu, J.; Kemner, K. M.: Functionalized Monolayers on Ordered Mesoporous Supports. *Science* **1997**, *276*, 923-926.

(27) Liong, M.; Lu, J.; Kovochich, M.; Xia, T.; Ruehm, S. G.; Nel, A. E.; Tamanoi, F.; Zink, J. I.: Multifunctional Inorganic Nanoparticles for Imaging, Targeting, and Drug Delivery. *ACS Nano* **2008**, *2*, 889-896.

(28) Xia, T.; Kovochich, M.; Liong, M.; Meng, H.; Kabehie, S.; George, S.; Zink, J. I.; Nel, A. E.: Polyethyleneimine Coating Enhances the Cellular Uptake of Mesoporous Silica Nanoparticles and Allows Safe Delivery of siRNA and DNA Constructs. *ACS Nano* **2009**, *3*, 3273-3286.

(29) Meng, H.; Liong, M.; Xia, T.; Li, Z.; Ji, Z.; Zink, J. I.; Nel, A. E.: Engineered Design of Mesoporous Silica Nanoparticles to Deliver Doxorubicin and P-Glycoprotein siRNA to Overcome Drug Resistance in a Cancer Cell Line. *ACS Nano* **2010**, *4*, 4539-4550.

(30) Trewyn, B. G.; Slowing, I. I.; Giri, S.; Chen, H.-T.; Lin, V. S. Y.: Synthesis and Functionalization of a Mesoporous Silica Nanoparticle Based on the Sol–Gel Process and Applications in Controlled Release. *Accounts of Chemical Research* **2007**, *40*, 846-853.

(31) Hsiao, J.-K.; Tsai, C.-P.; Chung, T.-H.; Hung, Y.; Yao, M.; Liu, H.-M.; Mou, C.-Y.; Yang, C.-S.; Chen, Y.-C.; Huang, D.-M.: Mesoporous Silica Nanoparticles as a Delivery System of Gadolinium for Effective Human Stem Cell Tracking. *Small* **2008**, *4*, 1445-1452.

(32) Lu, J.; Liong, M.; Zink, J. I.; Tamanoi, F.: Mesoporous Silica Nanoparticles as a Delivery System for Hydrophobic Anticancer Drugs. *Small* **2007**, *3*, 1341-1346.

(33) Ashley, C. E.; Carnes, E. C.; Phillips, G. K.; Padilla, D.; Durfee, P. N.; Brown, P. A.; Hanna, T. N.; Liu, J.; Phillips, B.; Carter, M. B.; Carroll, N. J.; Jiang, X.; Dunphy, D. R.; Willman, C. L.; Petsev, D. N.; Evans, D. G.; Parikh, A. N.; Chackerian, B.; Wharton, W.; Peabody, D. S.; Brinker, C. J.: The targeted delivery of multicomponent cargos to cancer cells by nanoporous particle-supported lipid bilayers. *Nature Materials* **2011**, *10*, 389-397.

(34) Ashley, C. E.; Carnes, E. C.; Epler, K. E.; Padilla, D. P.; Phillips, G. K.; Castillo, R. E.; Wilkinson, D. C.; Wilkinson, B. S.; Burgard, C. A.; Kalinich, R. M.; Townson, J. L.; Chackerian, B.; Willman, C. L.; Peabody, D. S.; Wharton, W.; Brinker, C. J.: Delivery of Small Interfering RNA by Peptide-Targeted Mesoporous Silica Nanoparticle-Supported Lipid Bilayers. *ACS Nano* **2012**, *6*, 2174-2188.

(35) Liu, J. W.; Stace-Naughton, A.; Jiang, X. M.; Brinker, C. J.: Porous Nanoparticle Supported Lipid Bilayers (Protocells) as Delivery Vehicles. *Journal of the American Chemical Society* **2009**, *131*, 1354-1355.

(36) Gottesman, M. M.; Fojo, T.; Bates, S. E.: Multidrug resistance in cancer: role of ATP-dependent transporters. *Nature Reviews Cancer* **2002**, *2*, 48-58.

(37) Sapra, P.; Allen, T. M.: Internalizing Antibodies Are Necessary for Improved Therapeutic Efficacy of Antibody-targeted Liposomal Drugs. *Cancer Research* **2002**, *62*, 7190-7194.

(38) Ferris, D. P.; Lu, J.; Gothard, C.; Yanes, R.; Thomas, C. R.; Olsen, J.-C.; Stoddart, J. F.; Tamanoi, F.; Zink, J. I.: Synthesis of Biomolecule-Modified Mesoporous Silica Nanoparticles for Targeted Hydrophobic Drug Delivery to Cancer Cells. *Small* **2011**, *7*, 1816-1826.

(39) Vallet-Regi, M.; Rámila, A.; del Real, R. P.; Pérez-Pariente, J.: A New Property of MCM-41: Drug Delivery System. *Chemistry of Materials* **2000**, *13*, 308-311.

(40) Trewyn, B. G.; Slowing, I. I.; Giri, S.; Chen, H.-T.; Lin, V. S. Y.: Synthesis and Functionalization of a Mesoporous Silica Nanoparticle Based on the Sol–Gel Process and Applications in Controlled Release. *Accounts of Chemical Research* **2007**, *40*, 846-853.

(41) Ambrogio, M. W.; Thomas, C. R.; Zhao, Y.-L.; Zink, J. I.; Stoddart, J. F.: Mechanized Silica Nanoparticles: A New Frontier in Theranostic Nanomedicine. *Accounts of Chemical Research* **2011**, *44*, 903-913.

(42) Li, Z.; Barnes, J. C.; Bosoy, A.; Stoddart, J. F.; Zink, J. I.: Mesoporous silica nanoparticles in biomedical applications. *Chemical Society Reviews* **2012**, *41*, 2590-2605.

(43) Angelos, S.; Yang, Y-W.; Khashab, N. M.; Stoddart, J. F.; Zink, J. I.: Dual-Controlled Nanoparticles Exhibiting AND Logic. *Journal of the American Chemical Society* **2009**, *131*, 11344-11346.

(44) Meng, H.; Xue, M.; Xia, T.; Zhao, Y.-L.; Tamanoi, F.; Stoddart, J. F.; Zink, J. I.; Nel, A. E.: Autonomous in Vitro Anticancer Drug Release from Mesoporous Silica Nanoparticles by pH-Sensitive Nanovalves. *Journal of the American Chemical Society* **2010**, *132*, 12690-12697.

(45) Nel, A. E.; Madler, L.; Velegol, D.; Xia, T.; Hoek, E. M. V.; Somasundaran, P.; Klaessig, F.; Castranova, V.; Thompson, M.: Understanding biophysicochemical interactions at the nano-bio interface. *Nature Materials* **2009**, *8*, 543-557.

(46) Castranova, V.; Vallyathan, V.: Silicosis and coal workers' pneumoconiosis. *Environ Health Perspectives* **2000**, *108*, 675-684.

(47) Donaldson, K.; Borm, P. J. A.: The Quartz Hazard: A Variable Entity. *Annals of Occupational Hygiene* **1998**, *42*, 287-294.

(48) Elias, Z.; Poirot, O.; DaniÃ¨re, M. C.; Terzetti, F.; Marande, A. M.; Dzwigaj, S.; Pezerat, H.; Fenoglio, I.; Fubini, B.: Cytotoxic and transforming effects of silica particles with different surface properties in Syrian hamster embryo (SHE) cells. *Toxicology In Vitro* **2000**, *14*, 409-422.

(49) Rimal, B.; Greenberg, A. K.; Rom, W. N.: Basic pathogenetic mechanisms in silicosis: current understanding. *Current Opinion in Pulmonary Medicine* **2005**, *11*, 169-173.

(50) Zhuravlev, L. T.: Concentration of hydroxyl groups on the surface of amorphous silicas. *Langmuir* **1987**, *3*, 316-318.

(51) Zhang, H.; Dunphy, D. R.; Jiang, X.; Meng, H.; Sun, B.; Tarn, D.; Xue, M.; Wang, X.; Lin, S.; Ji, Z.; Li, R.; Garcia, F. L.; Yang, J.; Kirk, M. L.; Xia, T.; Zink, J. I.; Nel, A.; Brinker, C. J.;

Processing pathway dependence of amorphous silica nanoparticle toxicity: colloidal vs. pyrolytic. *Journal of the American Chemical Society* **2012**, *134*, 15790-15804.

(52) Fubini, B.; Fenoglio, I.; Elias, Z.; Poirot, O.: Variability of biological responses to silicas: effect of origin, crystallinity, and state of surface on generation of reactive oxygen species and morphological transformation of mammalian cells. *Journal of Environmental Pathology, Toxicology and Oncology* **2001**, *20*, 109-118.

(53) Hudson, S. P.; Padera, R. F.; Langer, R.; Kohane, D. S.: The biocompatibility of mesoporous silicates. *Biomaterials* **2008**, *29*, 4045-4055.

(54) Yu, T.; Malugin, A.; Ghandehari, H.: Impact of Silica Nanoparticle Design on Cellular Toxicity and Hemolytic Activity. *ACS Nano* **2011**, *5*, 5717-5728.

(55) Slowing, I. I.; Wu, C.-W.; Vivero-Escoto, J. L.; Lin, V. S. Y.: Mesoporous Silica Nanoparticles for Reducing Hemolytic Activity Towards Mammalian Red Blood Cells. *Small* **2009**, *5*, 57-62.

(56) Nash, T.; Allison, A. C.; Harington, J. S.: Physico-Chemical Properties of Silica in Relation to its Toxicity. *Nature* **1966**, *210*, 259-261.

(57) Schoonen, M. A. A.; Cohn, C. A.; Roemer, E.; Laffers, R.; Simon, S. R.; O'Riordan, T.: Mineral-Induced Formation of Reactive Oxygen Species. *Reviews in Mineralogy and Geochemistry* **2006**, *64*, 179-221.

(58) Ghiazza, M.; Polimeni, M.; Fenoglio, I.; Gazzano, E.; Ghigo, D.; Fubini, B.: Does Vitreous Silica Contradict the Toxicity of the Crystalline Silica Paradigm? *Chemical Research in Toxicology* **2010**, *23*, 620-629.

(59) Brinker, C. J.; Kirkpatrick, R. J.; Tallant, D. R.; Bunker, B. C.; Montez, B.: NMR Confirmation of Strained Defects in Amorphous Silica. *Journal of Non-Crystalline Solids* **1988**, *99*, 418-428.

(60) Griscom, D. L.; Brinker, C. J.; Ashley, C. S.: Electron-Spin-Resonance Studies of Irradiated O-17-Enriched Sol-Gel Silicas - Organic Impurity Effects and the Structure of the Nonbridging-Oxygen Hole Center. *Journal of Non-Crystalline Solids* **1987**, *92*, 295-301.

(61) He, Q.; Zhang, Z.; Gao, Y.; Shi, J.; Li, Y.: Intracellular localization and cytotoxicity of spherical mesoporous silica nano-and microparticles. *Small* **2009**, *23*, 2722-2729.

(62) Meng, H.; Yang, S.; Li, Z.; Xia, T.; Chen, J.; Ji, Z.; Zhang, H.; Wang, X.; Lin, S.; Huang, C.; Zhou, Z. H.; Zink, J. I.; Nel, A. E.: Aspect Ratio Determines the Quantity of Mesoporous Silica Nanoparticle Uptake by a Small GTPase-Dependent Macropinocytosis Mechanism. *ACS Nano* **2011**, *5*, 4434-4447.

(63) Malvindi, M. A.; Brunetti, V.; Vecchio, G.; Galeone, A.; Cingolani, R.; Pompa, P. P.: SiO2 nanoparticles biocompatibility and their potential for gene delivery and silencing. *Nanoscale* **2012**, *4*, 486-495.

CHAPTER 2

A Reversible, Light-Operated Nanovalve

on Mesoporous Silica Nanoparticles

2.1 Abstract

Two azobenzene / cyclodextrin based nanovalves are designed, synthesized and assembled on mesoporous silica nanoparticles. When in aqueous conditions, the cyclodextrin cap is tightly bound to the azobenzene moiety and capable of holding back loaded cargo molecules. Upon irradiation with a near-UV light laser, *trans* to *cis*- photoisomerization of azobenzene causes the cyclodextrin cap to unbind and cargo to release. The addition of a bulky stopper group to the end of thread allows this design to be reversible; complete dethreading of cyclodextrin as a result of unbinding with azobenzene is prevented by the bulky end group. As a result, thermal relaxation of *cis*-azobenzene to *trans* allows for rebinding of cyclodextrin and resealing of remaining cargo. Two threads were designed with different lengths and tested with alizarin red S and propidium iodide. No cargo release was observed prior to light irradiation, and the system was capable of multiuse. On / off control was also demonstrated by tracking cargo release when the light stimulus was applied and removed.

2.2 Introduction

Mesoporous silica has found its application in many fields of chemistry.[1, 2, 3] A subset of mesoporous silica is the MCM-41 type mesoporous silica nanoparticle (MSN), which is characterized by its ordered, 2D hexagonal pore structure.[4] Since its discovery by Mobil researchers several decades ago,[5] MCM-41 has been an ideal choice as a drug delivery platform for its robust nature, high surface area to volume ratio, facile surface modification, low toxicity and high rates of cell internalization.[6, 7, 8, 9, 10] To be an effective drug delivery system, MSN must be able to separately retain cargo molecules while both in storage and in circulation, as well as deliver its payload upon arriving to its target. A variety of methods have been employed to prepare MSN to meet these criteria; researchers have exploited hydrophobicity as a method of passive cargo retention,[11] and/or engineered nanomachines based off of supramolecular nanovalves,[12, 13, 14] snap-tops,[15] metal nanocrystals,[16, 17] nanoimpellers,[18] supported lipid bilayers,[19] biomolecules,[20] and reversible chelation[21] for the goal of retaining cargo inside the pores of MSN. These systems have been designed to deliver their payload as a response to a variety of stimuli that can be already present inside cells, or can be externally applied as magnetic fields[22] and light.[23, 24] The use of internal stimuli such as pH or enzyme activation allows for the creation of a self-contained delivery system, but can inevitably lead to higher rates of undesired activation. The use of external stimuli such as light[25, 26] can allow for an additional degree of control through selective irradiation of the target site. Current designs adopt an all-or-nothing type of release: once initiated by a stimulus, cargo is continuously released until emptied. While a complete delivery of cargo may sometimes be desired, an alternative approach is to create a single set of nanocarriers capable of delivering its payload in controllable doses. In this way, a single treatment with such nanocarriers can deliver multiple sets of therapeutic

agents. To achieve this, a system must be designed that is capable of resealing itself when a stimulus is removed. In the case of internal stimuli such as pH or enzyme activation, removing the stimulus is not feasible. Therefore, light, an external stimulus, was considered for its facile on / off manipulation.

We have previously reported a nanovalve based on azobenzene derivatives that is light-operated.[23] In this pseudorotaxane design, light irradiation of a cyclodextrin / azobenzene adduct causes the more stable *trans*-azobenzene to isomerize into *cis*-azobenzene. Due to the low binding affinity of cyclodextrin to *cis*-azobenzene, the cyclodextrin unthreads from the stalk and allows cargo to release. This dissociation is essentially irreversible; thermal-relaxation of *cis*-azobenzene back to *trans*- theoretically can allow cyclodextrin in proximity to rebind, but after unthreading, this event is highly improbable due to the large solution volume and low solution concentrations of cyclodextrin. Therefore, in order to hold cyclodextrin close proximity to the particle even after it dissociates from the azobenzene, a full rotaxane design was preferred. This can allow for an effective rebinding after thermal conversion back to *trans*-azobenzene. In this way, a system can be designed that can be reversibly resealed upon light removal. Building on our previous azobenzene / cyclodextrin design, we report the (i) design and synthesis of two new azobenzene threads **3a** and **3b** capable of binding of α-cyclodextrin, and (ii) their assembly onto MSN to synthesize a full rotaxane nanovalve which (iii) with near-UV light irradiation, allows α-cyclodextrin to slide away from the pore openings, resulting in the delivery of two different sized fluorescent dyes alizarin red S (ARS) and propidium iodide (PI) and (iv) is capable of resealing cargo after the light irradiation is turned off, allowing for dosage control.

2.3 Results and Discussion

2.3.1 Design of the nanovalves

For adequate functioning of the nanovalve, a stalk must be designed that exhibits regional, reversible binding with a nanocap. After threading the nanocap, in its "closed" state, the region of highest binding affinity should also bring the nanocap close enough to the particle surface to prevent cargo escape. When binding is no longer favorable, the nanocap should be allowed to slide further along the thread in its "open" state before reaching an end-terminating stopper group, allowing cargo molecules to diffuse from the pores, but preventing the nanocap from unthreading completely. To achieve light responsiveness, this binding affinity must also be light dependent. For this reason, an azobenzene moiety was chosen.

Azobenzenes exhibit the property of photoisomerization, where its more stable *trans*-form can be converted into *cis*-azobenzene through light irradiation of the $\pi \rightarrow \pi^*$ band. Thermal relaxation of *cis*-azobenzene regenerates the *trans*- isomer.[32] This transformation results in a large change in dipole moment; as a result, *cis*-azobenzene is relatively more hydrophilic than the *trans*- conformation. This property allows macrocycles which possess hydrophobic interior regions to selectively bind with *trans*-azobenzene. Consequently, a cyclodextrin, which form inclusion complexes as a result of hydrophobic interactions,[27, 28] was chosen as the nanocap.

In the dark, the cyclodextrin can bind and form a supramolecular adduct with the *trans*-azobenzene moiety, which is driven by favorable interactions between the hydrophobic cyclodextrin cavity and the azobenzene core.[27] While all of the cyclodextrins exhibit a respectable binding affinity with *trans*-azobenzene, α-cyclodextrin was chosen for its ideal size in having inner cavity diameter of 0.47 nm that expands to 0.53 nm on its larger end (Figure 2.1a).[28] Irradiating with light causes *trans*-azobenzene to isomerize into its *cis*- form, which, due

to its increased hydrophilicity, no longer has a favorable binding constant with cyclodextrin and causes it to dissociate. The unbound cyclodextrin is able to slide along the thread but must be prevented from unthreading by terminating the end with a stopper group.

Several requirements for the choice of a stopper group were considered. The stopper must simultaneously be bulky enough to prevent the cyclodextrin from unthreading, but have a lower binding affinity with α-cyclodextrin than azobenzene in order to limit competitive binding with the stopper. For these reasons, an adamantane functional group was selected as the stopper. This molecule, with a diameter of 0.5 nm, is large enough to prevent α-cyclodextrin from unthreading, but still exhibits a low binding affinity with it. While other members of the cyclodextrin family β- and γ-cyclodextrin have binding constants of 7000 M^{-1} and 3500 M^{-1} with adamantane,[29] respectively, the strength of the α-cyclodextrin / adamantane adduct is considerably weaker at 100 M^{-1}.[29, 30] In this way, when possible, α-cyclodextrin will preferentially be bound to *trans*-azobenzene, but when *cis*-azobenzene is formed by photoexcitation, a meta-stable adamantane / α-cyclodextrin adduct holds the nanocap away from the pore openings to allow cargo release. To ensure an adequate clearance for cargo movement during this event, the distance between the azobenzene moiety and end stopper must be carefully tailored.

Because the size of many chemotherapy drugs falls between 1 - 2.5 nm, we designed two threads of different lengths in order to load and deliver both 1 nm and 2 nm sized cargo molecules. To illustrate this, three fluorescent dyes, alizarin red S (ARS) and propidium iodide (PI), and Hoechst 33342 with diameters 1.2 nm, 1.8 nm and 2.0 nm, respectively, were chosen as the cargo molecules. Thread FRS1 was tailored to allow for cargo movement in its "open" state with cargo sizes up to 1.6 nm, but in its "closed" state, clearance is reduced to 0.8 nm (Figure 2.1a). Therefore, ARS was selected as a candidate to test FRS1 for its ideal 1.2 nm size. Thread

EXT2 was designed with a 2.8 nm "open" distance when fully extended (Figure 2.1a). Similarly to FRS1, when closed, EXT2 reduces the α-cyclodextrin to pore distance to 0.8 nm in order to seal in cargo. As such, thread FRS1 is expected to load and deliver ARS but fail with Hoechst or PI, and thread EXT2 is expected to be compatible with PI.

2.3.2 Synthesis of MSN

MSNs were synthesized utilizing a surfactant-templated sol-gel process.[31] The resulting spherical nanoparticles were ~100 nm in diameter. After synthesis, MSN was directly modified with 3-aminopropyltriethoxysilane (APTES) by a post-synthetic grafting method in order direct the amine groups onto the particle surface. After modification with APTES, removal of the templating agent resulted in nanoparticles with hexagonally arranged mesopores about 2.2 nm in diameter (Figure 2.4-2.7).

2.3.3 Synthesis of the threads

Since α-cyclodextrin / azobenzene binding is dependent on hydrophobic interactions, considerations in the synthesis of both threads were made to ensure that the final attachment steps onto MSN could be made in a polar solvent. Because of this, a NHS ester functional group was chosen as the reactive end for its specificity and compatibility with non-aqueous, polar solvents. In the synthesis of both threads, p-nitrobenzoic acid was reacted in basic conditions with glucose to form compound **1**. To generate the NHS ester, **1** was reacted with N-hydroxysuccimide to form **2**. In the synthesis of FRS1, **2** was reacted with adamantylamine under dilute conditions and purified via column choromatography to isolate the monosubstituted product **3a**. For thread EXT2, adamantanecarboxylic acid was reacted with oxalyl chloride to generate adamantane carbonyl chloride. Nucleophilic substitution of the acid chloride with 2,2'-(ethylenedioxy)bis(ethylamine) afforded the monoalkylated product **2b**, which was reacted with

intermediate **2** under dilute conditions and purified under column chromatography to yield **3b**. To synthesize the rotaxane, compounds **3a** or **3b** were mixed with α-cyclodextrin in DMF to allow α-cyclodextrin to complex with azobenzene and form rotaxanes **4a** and **4b**, respectively. Attachment to MSN was accomplished by first modifying MSN with 3-aminopropyltriethoxysilane and extracting out the templating agent before a direct reaction with the NHS moieties of **4a** or **4b** and complete the synthesis of FRS1 and EXT2.

2.3.4 Loading and sealing of cargo

After grafting each of the rotaxane threads onto MSN, the assembled machines were washed with methanol to remove unreacted excess. In order to load cargo into the pores, FRS1 or EXT2 were suspended in an organic solvent under UV light irradiation to break the hydrophobic interactions between α-cyclodextrin and azobenzene to allow cyclodextrin to slide to the thread end and allow for pore access (Figure 2.1b1). Suspending and stirring the nanoparticles in an organic solution of fluorescent dye allowed cargo to slowly load inside the pores. In order to seal the nanocap, the loaded nanoparticles were solvent exchanged with water, where the exclusion of solvent from the cyclodextrin cavity is favored, allowing the cyclodextrin cap to rebind with azobenzene and tightly seal back the loaded cargo (Figure 2.1b2). Excess, surface-adsorbed cargo was removed with subsequent water washes until the eluent no longer exhibited fluorescence.

2.3.5 Characterization

In order to verify the success of each step in the synthesis of FRS1 and EXT2, ^{1}H NMR and ESI-TOF mass spectroscopy were employed on each of the intermediates in the thread syntheses (Figure 2.7-2.12). The synthesized MSN quality was determined through TEM imaging, which confirmed an average diameter of 100 nm and a 2D-hexagonally packed pore

structure with pore diameters of 2-2.4 nm (Figure 2.4). Power XRD measurements were used to confirm the hexagonal mesopore phase, evident in the higher order Bragg diffraction peaks indexed as the (100), (110), and (200) planes with a lattice spacing of 4 nm (Figure 2.5). Complete removal of CTAB was verified by subjecting bare MSN to the extraction procedure and performing FTIR spectroscopy on the resulting material, which showed a complete removal of organic material with the disappearance of sp^3 C-H stretching peaks present around 3000 cm^{-1} (Figure 2.6). Successful amine modification of MSN was verified through FTIR spectroscopy, with the appearance of the dual primary amine stretches around 3200 cm^{-1} and sp^3 C-H stretching peaks at 3400 cm^{-1} after CTAB extracting. The attachment efficiency of both FRS1 and EXT2 threads to MSN was verified through UV-Vis spectroscopy, where the solution absorbances of both threads were taken prior to attaching onto APTES modified MSN. The MSN modified with EXT2 or FRS1 showed similar absorption peaks respectively centered at 334 and 336 nm, which can be attributed to a successful attachment of the azobenzene threads (Figure 2.13, 2.16). After isolating the modified nanoparticles through centrifugation, absorption spectroscopy of the corresponding supernatant showed a negligible absorbance in this region, which indicated high attachment efficiency.

2.3.6 Operation of the machines

In order to release the loaded cargo, binding between the cyclodextrin molecule and azobenzene moiety must first be disrupted. This can be achieved through light excitation of an electron in the azobenzene π to π^* band which lies in the near UV region, causing the azobenzene to isomerize from *trans*- to *cis*-azobenzene (Figure 2.13, 2.16).[32] The low binding affinity between *cis*-azobenzene and cyclodextrin results in it sliding down the thread to which it binds with the adamantane stopper, allowing the free movement of cargo molecules loaded

inside the pores (Figure 2.1b3). When the light is removed, thermal relaxation of *cis*-azobenzene to the *trans*- isomer allows α-cyclodextrin to rebind, preventing additional cargo molecules from releasing. In this way, specific dosage control can be achieved.

2.3.7 Light activated cargo delivery

To verify the operation of the nanomachine, continuous monitoring by fluorescence spectroscopy was employed. In a corner of a quartz cuvette, a dried sample of FRS1 or EXT2 was confined and water gently added in order to prevent suspending the nanoparticles into solution. To monitor the release of cargo, a low power probe beam (377 nm, 1 mW) was aimed through the solution supernatant in order to excite fluorescent dye molecules released from the sample. The corresponding emission was filtered through a cut-off filter and selected using a monochromator before focusing onto a CCD detector. Integrating over a specific wavelength range in real-time allowed for the generation of a time-resolved release profile. To irradiate the sample and induce cargo release, a pump beam (403 nm, 85 mW, 1 mm diameter), was directly focused onto the sample (Figure 2.12).

2.3.8 FRS1 light activated release

Using this method, an initial baseline reading of the FRS1 sample was collected for two hours. Figure 2.2a shows little to no dye release prior to activation of the pump beam, illustrating the strength of the α-cyclodextrin / *trans*-azobenzene binding in sealing in cargo. When irradiated, an increasing ARS fluorescence is observed, indicating the release of cargo (Figure 2.2a curve 1). The curved shape illustrates an initially high release rate as dye molecules diffuse from the highly concentrated pore interiors into the solution. After several hours, the slope of the curve flattens off as fewer dye molecules remains inside the pores. To demonstrate the reusability of the rotaxane valve, after a completed release, the sample was washed with ethanol

to remove any remaining dye, reloaded with ARS, and washed in water to remove surface adsorbed dye and reseal the pores. This reloaded sample was subjected to the same release profile experiment to ensure that α-cyclodextrin is still present on the rotaxane thread and capable of sealing in cargo**.** The baseline in Figure 2.2a curve 2 demonstrates that this reloaded sample remains tightly sealed prior to light irradiation, indicating that nanocap has not been removed from the rotaxane thread. After irradiation with the pump laser, an increase in ARS fluorescence is observed, showing that the system is still light responsive, and suggesting the reusability of FRS1 (Figure 2.2a curve 2). To confirm the observed fluorescence change is due to ARS, the supernatant after each release profile was analyzed using UV-Vis spectroscopy and compared to a standard solution of ARS (Figure 2.15).

In order to also verify the reversibility of the rotaxane nanovalve, FRS1 was subjected to a series of "on" / "off" tests. In the same experimental setup as described above, cargo release from a FRS1 sample loaded with ARS was tracked while the pump beam was turned off for 30 minute intervals (Figure 2.3 curve a**)**. At first, when irradiated, FRS1 exhibits the presumed exponential shape indicative of ARS release, but flattens out when the pump beam is turned off. This can be attributed to a thermal relaxation of *cis*-azobenzene into *trans*-azobenzene in the dark, which allows α-cyclodextrin to rebind and prevent additional cargo release **(**Figure 2.1b4**)**. Reintroducing the pump beam to the sample causes ARS fluorescence to increase once more, indicating the reversibility of this system and its potential for dosage control.

In order to ensure the necessity of α-cyclodextrin in the rotaxane design, a control experiment was performed in which a sample of FRS1 was assembled without first threading on α-cyclodextrin. This sample was then loaded with ARS and washed until the supernatant was colorless. The corresponding fluorescence release profile was also acquired with this sample,

which showed increasing ARS fluorescence prior to pump beam irradiation. This suggests that without a cyclodextrin cap, the azobenzene thread alone is unable to retain cargo molecules (Figure 2.3 curve b), and thus demonstrates the necessity of the α-cyclodextrin nanocap for successfully sealing in ARS cargo.

Although FRS1 is able to load and release ARS, the dimensions of FRS1 in its closed and open states indicate that it is unable able to load cargo greater than 1.5 nm. To test this, FRS1 was assembled and loaded with Hoechst 33342 (2 nm). After the loading and washing steps, the loaded nanoparticles showed no Hoechst fluorescence, indicating no Hoechst molecules made it into the pores. To corroborate this, the sample was tested in a similar release profile experiment as described above while monitoring the solution for Hoechst fluorescence. After collecting a baseline, irradiating the sample with the pump laser caused no change in fluorescence over the background noise (Figure 2.16). Because of its length, FRS1 is unable to load a larger sized cargo molecule like Hoechst. The longer thread length of EXT2 allows cargo up to 2.2 nm to be loaded inside of the pores. To assess whether this longer design can achieve the goal of delivering larger cargo molecules, thread EXT2 was similarly tested with PI cargo.

2.3.9 EXT2 light activated release

Under the same laser experimental setup as shown in Figure 2.12, EXT2 modified nanoparticles were tested for their viability as a delivery system for PI cargo. In order to detect PI emission, the monochromator was centered at 600 nm with a 300 nm window. Similarly, a baseline reading was collected before activating the pump beam and stimulating cargo release. Prior to activating the pump beam, the initial flat baseline reading for EXT2 shows no observable PI fluorescence, showing that this rotaxane thread is capable of sealing in the PI cargo (Figure 2.2b curve1). When the pump beam is turned on, an increase in fluorescence is observed,

indicating that PI is being released from the nanoparticles and into the solution. The solution fluorescence of PI increases gradually over several hours before approaching a maxima, when the dye has been completely released from EXT2 (Figure 2.2b curve 1). This indicates that EXT2 is capable of releasing PI dye with light stimulation.

In order to verify the light irradiation did not destroy the thread, or cause α-cyclodextrin to unthread altogether, after a completed release the sample was washed to remove any remaining PI cargo before reloading in a fresh solution of PI. After washing off the excess, surface adsorbed dye with water, a second release profile was generated under the same conditions as used previously (Figure 2.2b curve 2). The initial collection of data shows a flat baseline prior to pump beam activation, indicating that the reloaded EXT2 system is still capable of sealing in PI. Upon irradiation with the pump beam, an increase in solution fluorescence is observed (Figure 2.2b curve 2**)**, suggesting that PI cargo is again diffusing from the nanoparticle pores and into the solution. This release increases exponentially as more EXT2 moieties are isomerized into *cis*-azobenzene which allows PI to repartition from the highly concentrated pore interiors into solution. Upon approaching equilibrium, the curve asymptotes off similarly to the previous release curve (Figure 2.2b). Because cargo release only occurs with light irradiation, EXT2 is demonstrated to be a reusable, light-responsive delivery system for PI.

2.4 Summary

In summary, two reversible, reusable nanovalves were designed based on the azobenzene / cyclodextrin motif that is capable of the controlled release of both small cargo (ARS dye) and larger dye molecules (PI). In aqueous environments, both nanovalves remain tightly closed due to the strong binding between α-cyclodextrin and the *trans*-azobenzene moiety, but light irradiation causes the photoisomerization of *trans*- to *cis*-azobenzene, unbinding the cylodextrin cap and allowing it to slide to the adamantane end of the thread and cargo to release. Because this binding is reversible, once the light is turned off, thermal relaxation of *cis*-azobenzene regenerates *trans*-azobenzene, which allows the cyclodextrin to rebind and seal in the remaining cargo molecules. By tuning the length of the azobenzene / adamantane thread, cargo size-selectivity can be achieved. Currently, this system is being tested *in vitro* with the goal of developing an externally light-activated nanovalve to deliver anti-cancer drugs to cancerous cells.

2.5 Experimental

2.5.1 General Comments

All of the chemicals used in this study were used as purchased from major suppliers such as Sigma-Aldrich and Fisher Scientific. Release profiles were generated using a time-resolved fluorescence spectroscopy setup (Figure 2.10). A Coherent 377 nm CUBE laser was used as the probe beam (1-15 mW, 1 mm diameter), and the emission spectra were monitored using a Princeton Instruments Roper CCD detector cooled to -127 K. The pump beam used was a Coherent 403 nm CUBE laser (1-100 mW, 1 mm diameter) with a manually operated shutter. Powder X-ray diffraction measurements were made using a Panalytical X'Pert Pro diffractometer. ^{1}H NMR was performed on a Bruker ARX400 spectrometer in chloroform-d or DMSO-d solvents. Chemical shift is listed in ppm. The solvent signal was used as an international standard. TEM images were acquired on a JEM1200-EX microscope. TOF-ESI^{+} spectra were collected on a Waters LCT Premier XE Time of Flight instrument. DLS readings were collected on a ZetaPals DLS and zeta potential instrument.

2.5.2 Synthesis of MCM-41 Nanoparticles

Cetyltrimethylammonium bromide (CTAB, 0.25 g, 0.7 mmol) dissolved in deionized water (120 mL) with heat and stirring. The stir speed and temperature (80 ^{o}C) was allowed to stabilize for 1 hour, and NaOH (2 M, 870 μL, 1.7 mmol) was added to the mixture. To this, triethoxysilane (TEOS, 1.2 mL, 5.4 mmol) was then added dropwise under vigorous stirring (800 RPM) and reacted for 2 hours at 80 ^{o}C. After completion, the cloudy solution was cooled to room temperature, and collected through centrifugation (7830 RPM, 15 min). The collected nanoparticles were washed with methanol until the washings showed a pH of 7. Synthesized nanoparticles showed a monodisperse DLS reading and low PDI (224 nm, PDI 0.01). Pore

structure and particle morphology were verified using TEM and XRD, respectively (Figure 2.4, 2.5).

2.5.3 Synthesis of 3-Aminopropyltriethoxysilane Modified MSN

Synthesized MSN (50 mg) was washed twice with toluene before resuspending in anhydrous toluene (10 mL). After purging a round bottom flask with dry argon, the reaction vessel was charged with the MSN / toluene mixture and 3-aminopropyltriethoxysilane (30 μL, 0.13 μmols). The mixture was allowed to react at reflux temperatures under dry argon atmosphere for 12 hours, before isolating the nanoparticles via centrifugation (5000 RPM, 5 min). The modified nanoparticles were washed twice with toluene and with DMF. Successful modification of MSN was verified after surfactant extraction with FTIR spectroscopy, as shown in the appearance of two primary amine stretching peaks at 3200 cm^{-1}, 3400 cm^{-1} and the appearance of sp^3 hybridized C-H stretching at 2980 cm^{-1}.

2.5.4 Extraction of Templating Agent

Synthesized MSN (120 mg) were suspended in a solution of ammonium nitrate in ethanol (133 mg in 50 mL) with vigorous stirring and sonication time. The mixture was stirred under reflux for 2 hours. After the allotted reaction time, the particles were recollected through centrifugation (7830 RPM, 15 min) and washed with portions of methanol (5 x 2 mL). To verify complete extraction of CTAB from the pores, FTIR spectroscopy was performed on the isolated particles (Figure 2.6). DLS readings after surfactant extraction indicated a more monodisperse MSN (180 nm, PDI 0.005).

2.5.5 Synthesis of 4,4'-Azobenzenecarboxylic acid

In a round bottom flask, p-nitrobenzoic acid (15 g, 9 mmols) was dissolved in a solution of sodium hydroxide in water (50 g in 225 mL) with heat and vigorous stirring. In a separate

reaction vessel, a glucose solution was prepared (100 g, 55 mmols) in water (150 mL) by heating until homogenous. After cooling to room temperature, the glucose solution was added dropwise to the dissolved p-nitrobenzoic acid at a rate in order to maintain a temperature of 60 ^{o}C and stirred at room temperature for 12 hours under atmospheric oxygen. After the allotted reaction time, the dark brown colored mixture was aged for four hours before filtering. The bright orange precipitate was dissolved in fresh water (50 mL) and acidified with acetic acid (10%, 10 mL) where a light orange precipitate was observed. After filtering, the product was washed with portions of purified water (3 x 50 mL) and dried under vacuum to yield 4,4'-azobenzenedicarboxylic acid. ^{1}H NMR (DMSO-d): δ 7.99 (d, 4H), δ 8.13 (d, 4H).

2.5.6 Synthesis of 2

4,4'-azobenzenedicarboxylic acid (300 mg, 1.1 mmols) was dissolved in anhydrous DMF (30 mL) with heating. After cooling to room temperature, N-hydroxysuccinimide (300 mg, 2.6 mmols) was added to the reaction mixture along with coupling agent 1-Ethyl-3-(3-dimethylaminopropyl)carbodiimide (EDC, 500 mg, 3.2 mmols). A catalytic amount of 4-dimethylaminopyridine (DMAP) was added to the mixture and reacted for 12 hours at room temperature under dry nitrogen. After complete reaction, water (100 mL) was added to the reaction vessel to precipitate out a red solid. After filtering, the product was washed with portions of water (3 x 50 mL) and methanol (30 mL) and vacuum dried to yield a dark red powder. ^{1}H NMR (DMSO-d): δ 8.32 (d, 4H), δ 8.14 (d, 4H), δ 2.89 (s, 8H).

2.5.7 Synthesis of 1-Adamantanecarbonyl chloride

1-Adamantanecarboxylic acid (2 g, 11 mmols) was dissolved in DCM (50 mL) and catalytic amounts of DMF added before cooling to 0 ^{o}C. To this, oxalyl chloride (1.5 mL, 18 mmols) was introduced dropwise to the ice-cold mixture. After the addition, the reaction was

allowed to warm to room temperature and reacted for an additional two hours. Completion of the reaction was verified with TLC plate, and the solvent was removed under reduced pressure to isolate adamantanecarbonyl chloride. The white solid was used without further purification. ^{1}H NMR (DMSO-d): δ 2.09 (s, 3H), δ 1.98 (d, 6H), δ 1.78 (q, 6H).

2.5.8 Synthesis of 2b

In a round bottom flask, potassium carbonate (600 mg) was vacuum dried with heating for 30 minutes and purged with dry argon before adding anhydrous DCM (20 mL) and 2,2'-(ethylenedioxy)bis(ethylamine) (1.5 mL, 10 mmols). The reaction vessel was sealed before cooling to 0 ^{o}C in an ice bath. In a separate container, adamantanecarbonyl chloride (1 g, 5 mmols) was dissolved in anhydrous DCM (10 mL) and cooled to ice temperatures before adding dropwise to the first mixture. After the complete addition, the reaction mixture was allowed to warm to room temperature and stirred for an additional 2 hours, where TLC plate analysis confirmed reaction completion. The mixture was filtered to remove excess potassium carbonate, washed once with water (10 mL) and then acidified with hydrochloric acid (10%, 2 mL) before extracting the organic phase with water (3 x 15 mL). The combined aqueous layers were washed with DCM (3 x 10 mL) before adjusting to pH 8 with NaOH (10%). The aqueous layer was then extracted with DCM (5 x 15 mL), and the combined organic layers washed with brine, and dried under anhydrous sodium sulfate before concentrating under rotary evaporator to yield compound **2b** as a viscous, clear liquid. ^{1}H NMR (chloroform-d): δ 6.13 (s, 1H), δ 3.53 (s, 4H), δ 3.42 (m, 4H), δ 3.29 (q, 2H), δ 2.74 (t, 2H), δ 1.90 (s, 3H), δ 1.72 (s, 6H), δ 1.57 (t, 6H). TOF-ESI^{+} MS (calculated at 310.2): m/z 311.2 ($M+H^{+}$).

2.5.9 Synthesis of 3a

In a reaction vessel, compound **2** (100 mg, 0.22 mmols) was dissolved in DMF (20 mL) with gentle heating and cooled to room temperature. Separately, adamantylamine (50 mg, 0.33 mmols) was dissolved in anhydrous DCM (5 mL) and cooled to 0 ^{o}C. The adamantylamine mixture was added to the mixture containing compound **2** dropwise over 2 hours, and allowed to react overnight at room temperature. After completion, the mixture was diluted with water (50 mL) and extracted with ethyl acetate (3 x 30 mL). The organic phases were combined and washed with water (5 x 20 mL) to remove the dissolved DMF, washed with brine and dried with anhydrous sodium sulfate. After concentrating the solution under reduced pressure, the crude product was purified with column chromatography on a silica stationary phase (EtOAc : hexanes = 1 : 2), and the second band isolated to yield quantitative amounts of **3a**. ^{1}H NMR (DMSO-d): δ 8.29 (d, 2H), δ 8.09 (d, 2H), δ 7.95 (m, 4H), δ 2.89 (s, 4H), δ 2.24 (t, 3H), δ 2.05 (d, 6H), δ 1.64 (s, 6H). TOF-ESI^{+} MS (calculated at 500.2): m/z 501.2 (M+H^{+}).

2.5.10 Synthesis of 3b

In a round bottom flask, compound **2** (100 mg, 0.22 mmols) was dissolved in DMF (20 mL) with gentle heating and allowed to cool to room temperature. In a separate vessel, compound **2b** (100 mg, 0.32 mmols) was dissolved in DCM (5 mL) before adding to the solution of compound **2** over a period of 2 hours. After the complete addition, the mixture was allowed to react overnight at room temperature before diluting with water (30 mL) and extracting with ethyl acetate (5 x 10 mL). The combined organic layers were washed with water (5 x 15 mL), once with brine and dried over anhydrous sodium sulfate before concentrating on a rotary evaporator. The crude product was purified with column chromatography on a silica stationary phase, and eluted with ethyl acetate. The second band was isolated as a dark red solution, and the solvent

evaporated under reduced pressure to isolate **3b** as a dark red powder. ^{1}H NMR (chloroform-d): δ 8.31 (d, 2H), δ 7.97-8.05 (m, 6H), δ 6.87 (s, 1H), δ 5.97 (s, 1H), δ 3.58-3.72 (m, 8H), δ 3.57 (t, 2H), δ 3.44 (q, 2H), δ 2.94 (s, 4H), δ 2.01 (s, 3H), δ 1.82 (d, 6H), δ 1.67 (s, 6H). TOF-ESI^{+} MS (calculated at 659.3): m/z 660.3 ($M+H^{+}$).

2.5.11 Synthesis of 4a

In a sealed reaction vessel charged with **3a** (6 mg, 1.1 μmols) and α-cyclodextrin (17 mg, 2.3 μmols) was dissolved in anhydrous DMF (1 mL). The reaction mixture was stirred at room temperature for an additional 2 hours to form rotaxane **4a**.

2.5.12 Synthesis of 4b

In a similar fashion as described above, a sealed reaction vessel with **3b** (2 mg, 0.3 μmols) and α-cyclodextrin (6 mg, 0.7 μmols) was dissolved in anhydrous DMF (1 mL). The reaction mixture was also stirred at room temperature for an additional 2 hours to allow α-cyclodextrin to thread onto **3b** to synthesize rotaxane **4b**.

2.5.13 Synthesis of FRS1

APTES modified MSN (20 mg) was washed twice with DMF before resuspending in a mixture of **4a** (23 mg in 1 mL DMF). The reaction vessel was sealed under dry argon atmosphere and allowed to react for 12 hours at room temperature, before collecting through centrifugation (15000 RPM, 3 min). The thread modified nanoparticles were washed with two portions of methanol and resuspended in ethanol. Successful attachment of the thread was verified through UV-Vis spectroscopy of a suspension of FRS1 modified nanoparticles (Figure 2.13).

2.5.14 Synthesis of EXT2

A sealed reaction vessel purged with dry argon gas was charged with APTES modified MSN (20 mg) that have been washed twice with anhydrous DMF. To this, a solution of **4b** (8 mg

in 1 mL DMF) was added and allowed to react at room temperature for 12 hours. The product was collected through centrifugation (15000 RPM, 3 min), washed twice with methanol and suspended in ethanol. Successful attachment of the thread was verified through UV-Vis spectroscopy of a suspension of EXT2 modified nanoparticles (Figure 2.14).

2.5.15 Loading of Fluorescent Dye and Sealing in Cargo

In a typical loading procedure, a sample of FRS1 or EXT2 was suspended in a concentrated dye solution. For ARS loaded samples, FRS1 nanoparticles were suspended in an ethanoic ARS dye solution (2 mM, 1 mL). For Hoechst 33342 samples, FRS1 or EXT2 nanoparticles were suspended in a solution of Hoechst in ethanol : acetone = 1 : 1 (1 mM, 1 mL). For PI loaded samples, EXT2 nanoparticles were suspended in an ethanoic PI dye solution (1 mM, 1 mL). Samples were stirred at room temperature for 24 hours before collecting with centrifugation (15000 RPM, 10 min). To seal in cargo and wash off excess surface-adsorbed dye, samples were washed with fresh portions of water until the supernatant exhibited no more fluorescence under blacklight and dried under vacuum prior to testing.

2.5.16 Assessment of Light activated Cargo Release

FRS1 or EXT2 samples (5 mg) loaded with an appropriate dye were confined to the corner of a glass cuvette. Water (4 mL) was gently added to the particles at a rate to prevent particles from being resuspended into solution. A 377 nm excitation laser (1 mW) was aimed through the solution supernatant. Emission of dye molecules released from each sample in the solution supernatant was monitored in real time by focusing the emitted light through a collecting lens, a 450 nm cutoff filter, and a monochromator (300 nm window) before integrating on a CCD detector (Figure 2.12). To track release of ARS, the monochromator was centered on 550 nm, and the fluorescence integrated from 550-600 nm. PI release was monitored by

centering the window at 600 nm and tracking dye emission from 600-620 nm. A baseline was collected over 1.5 hours to allow solution suspended particles to settle before a 403 nm pump beam (85 mW) was focused directly on the sample to stimulate cargo release. For the on/off experiments, the pump beam was turned off at timed intervals.

2.5.17 Reloading and Reuse Assessment

After acquiring a complete release profile, the sample was heated to 60 ^{o}C in ethanol for 12 hours in order to dissociate α-cyclodextrin and remove all additional cargo from areas of the sample not activated by the pump beam. The solution was centrifuged (15000 RPM, 15 min) to remove suspended nanoparticles and analyzed under UV-Vis spectroscopy in order to verify the identity of the released cargo, and the sample pellet reloaded in an appropriate dye solution before washing away the unloaded excess. The reloaded samples were subjected to a second release profile test, and the corresponding time resolved fluorescence spectra collected in a similar fashion as described above.

2.6 Figures

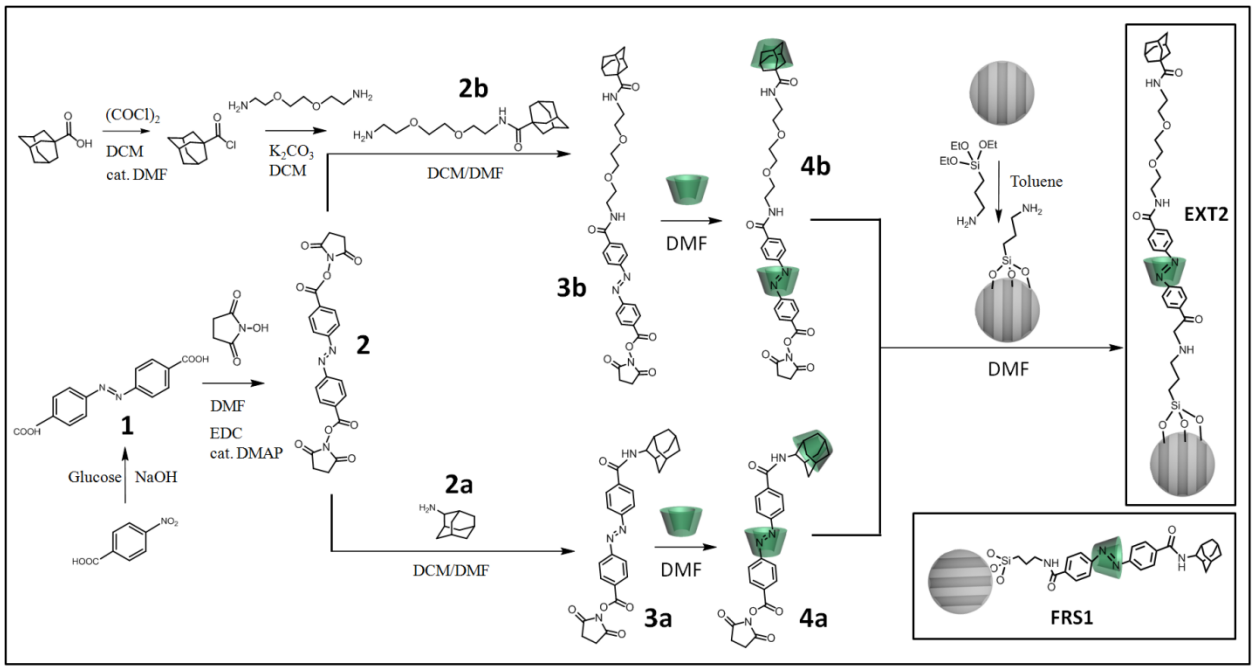

Scheme 2.1. Schematic overview of the synthesis of threads FRS1 and EXT2. P-nitrobenzoic acid is reacted in basic conditions with glucose to give **1**. Reaction with N-hydroxysucciminide with coupling agent EDC yields **2**, which can be reacted with one equivalence of **2a** or **2b**, the mono substituted product of 2,2'-(ethylenedioxy)bis(ethylamine) and 1-adamantanecarbonyl chloride, to generate **3a** and **3b**, respectively. Intermediates **3a** and **3b** can be mixed with α-cyclodextrin in DMF to form a cyclodextrin/azobenzene adduct, and reacted with APTES modified MSN to complete the synthesis of threads FRS1 and EXT2.

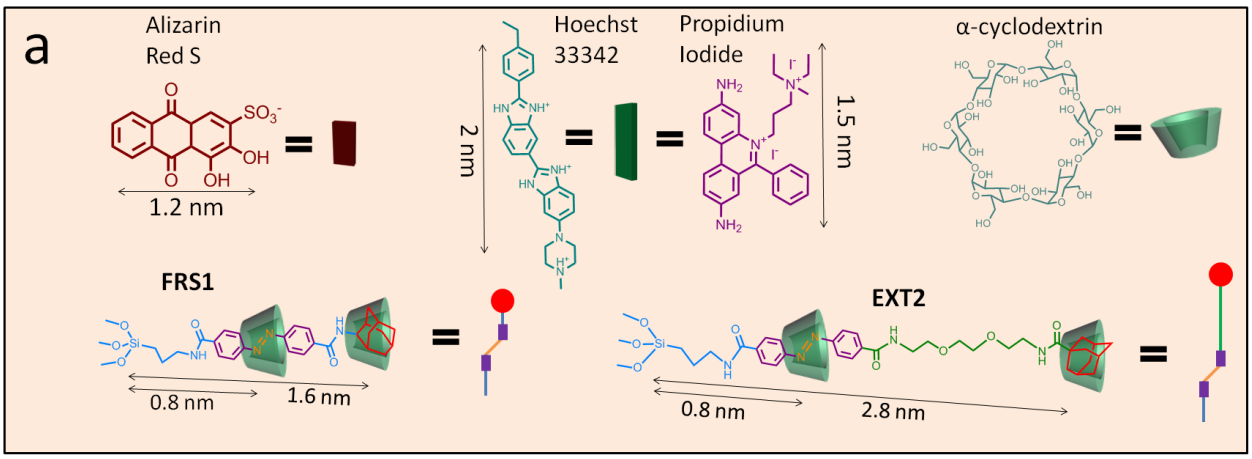

Figure 2.1. (a) Size illustration of various cargo molecules in reference to azobenzene stalks FRS1 and EXT2. Using FRS1, Hoechst 33342 and propidium iodide cargo cannot be loaded into MSN even when the cyclodextrin is shifted towards the adamantane stopper. Because of size constraints, FRS1 only allows for cargo molecules < 2 nm to move from the MSN pores in its open state. MSN assembled using EXT1 can load alizarin, Hoechst 33342 and propidium iodide cargo.

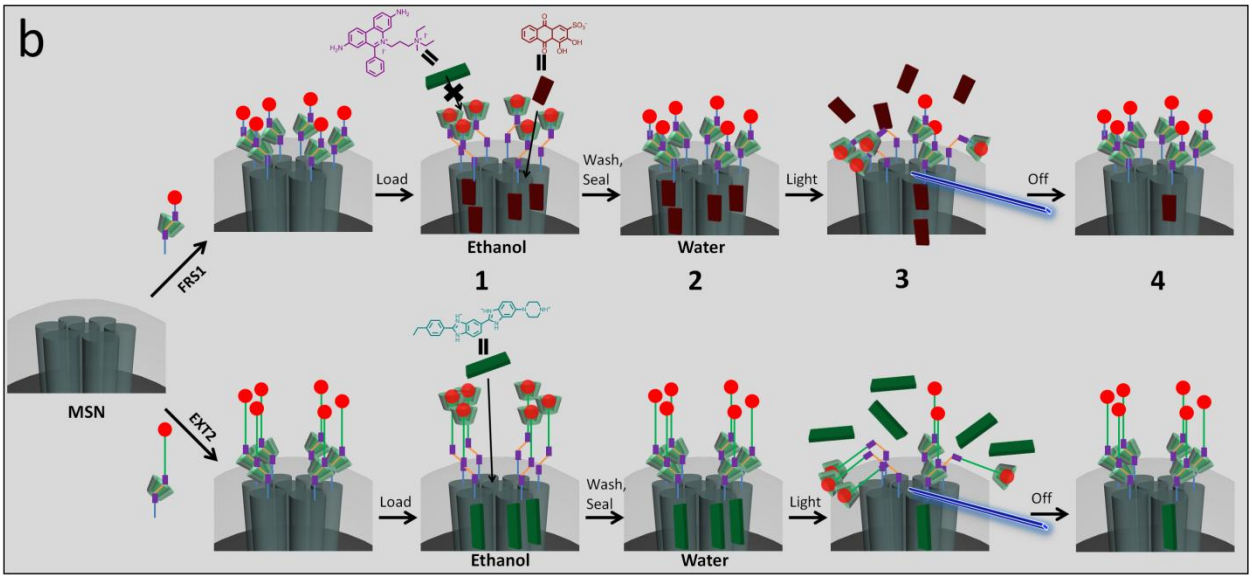

Figure 2.1 (b) Schematic illustration of fully assembled rotaxane nanovalve functioning. (1) After assembly, cargo can be loaded in an organic solvent, which destabilizes hydrophobic interactions between the cyclodextrin and azobenzene moiety. (2) Upon changing the solvent

back to water, the cyclodextrin reforms a supramolecular adduct with azobenzene, sealing in the loaded cargo. (3) Irradiating with light causes a conformational change from *trans*-azobenzene to *cis*-azobenzene, resulting in the cyclodextrin sliding to the end of the stalk. (4) When the light is turned off, thermal relaxation of *cis*-azobenzene to the more stable *trans* isomer allows cyclodextrin to rebind with the azobenzene moiety and seal in cargo.

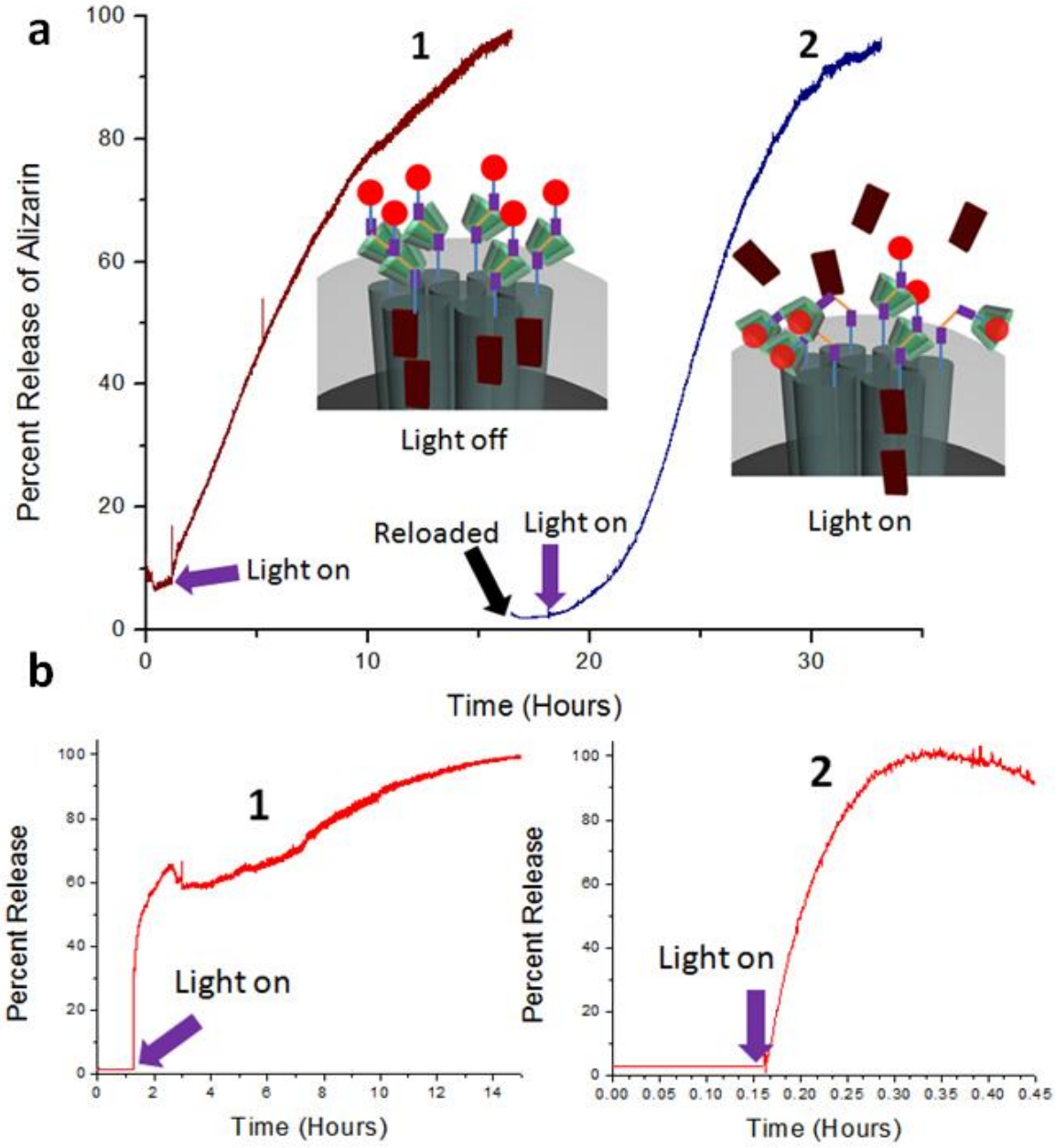

Figure 2.2. (a) Time resolved fluorescence spectra showing 403 nm light activated release of alizarin red S dye from FRS1. In trace 1, the flat baseline collected prior to light irradiation indicates that FRS1 is capable of sealing in ARS cargo in the dark. When the pump beam is activated, an increase of solution fluorescence is observed, corresponding to ARS cargo release. After a completed release, the particles were heated in ethanol to remove remaining dye, reloaded with alizarin and washed with water until washes were colorless. Trace 2 shows that

this reloaded sample also displays a similar behavior in which ARS is only observed to release with light irradiation, indicating the reusability of the FRS1 system. (b) Time resolved fluorescence spectra showing 403 nm light activated release of propidium iodide dye from EXT2. Trace 1 shows no premature cargo release prior to light activation. After irradiation with 403 nm light, an increase in PI fluorescence is detected in the solution supernatant. After a completed release, the sample was heated in ethanol to remove any remaining dye before reloading with PI. Trace 2 shows that this reloaded sample does not exhibit any leakage, and again releases cargo upon light irradiation.

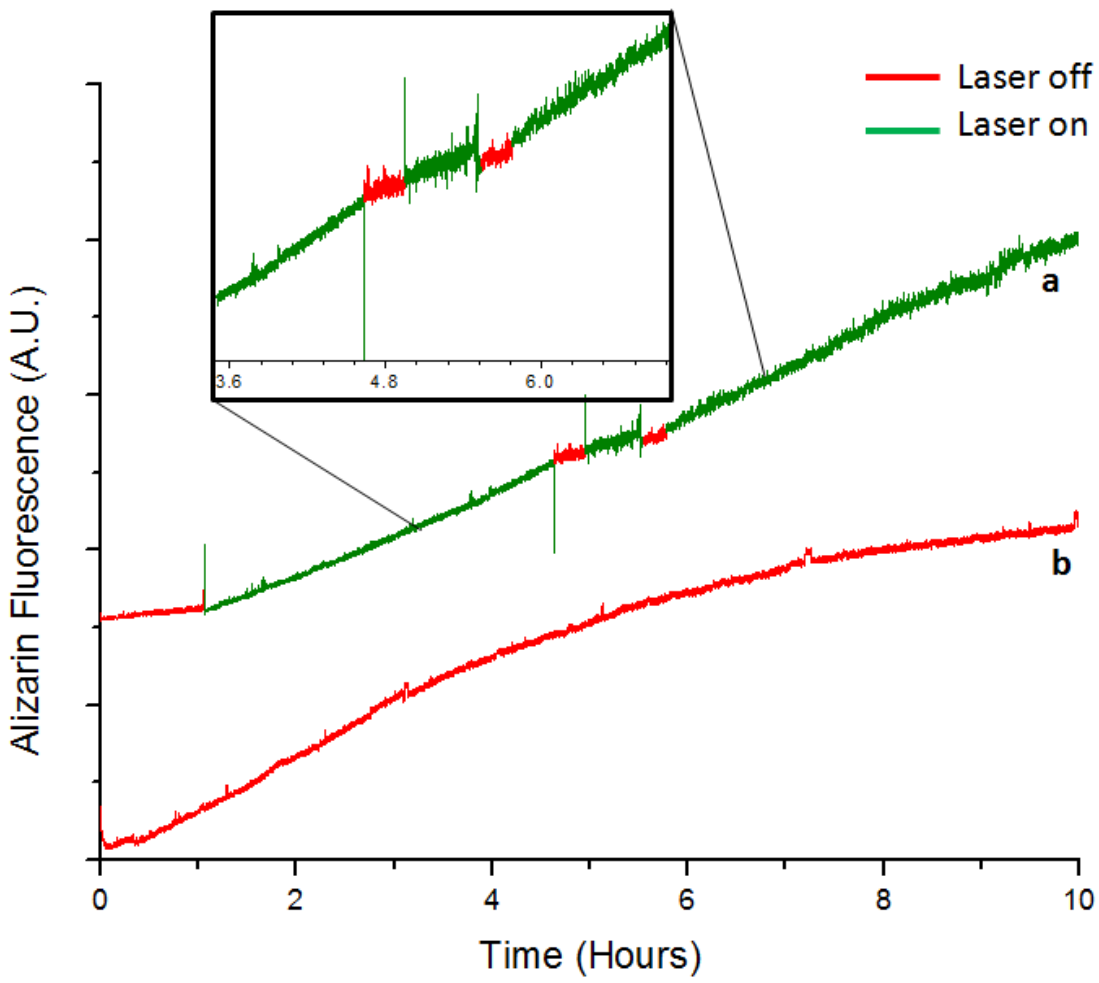

Figure 2.3. Time resolved fluorescence spectra demonstrating (a) on/off properties of FRS1. The slope of curve (a) flattens off when the pump beam is turned off (red areas), indicating the resealing capabilities of FRS1 in the dark. With thermal relaxation of *cis*-azobenzene to *trans*-azobenzene, FRS1 is capable of resealing itself and preventing additional cargo release. Upon re-irradiation, the nanovalve continues to function as expected and cargo release is observed. (b) To verify the necessity of the nanocap, a control was performed in which the cyclodextrin binding step was omitted in the assembly of FRS1. Prior to irradiation with the pump beam, cargo release was observed. This indicates α-cyclodextrin is required in order to tightly seal in cargo.

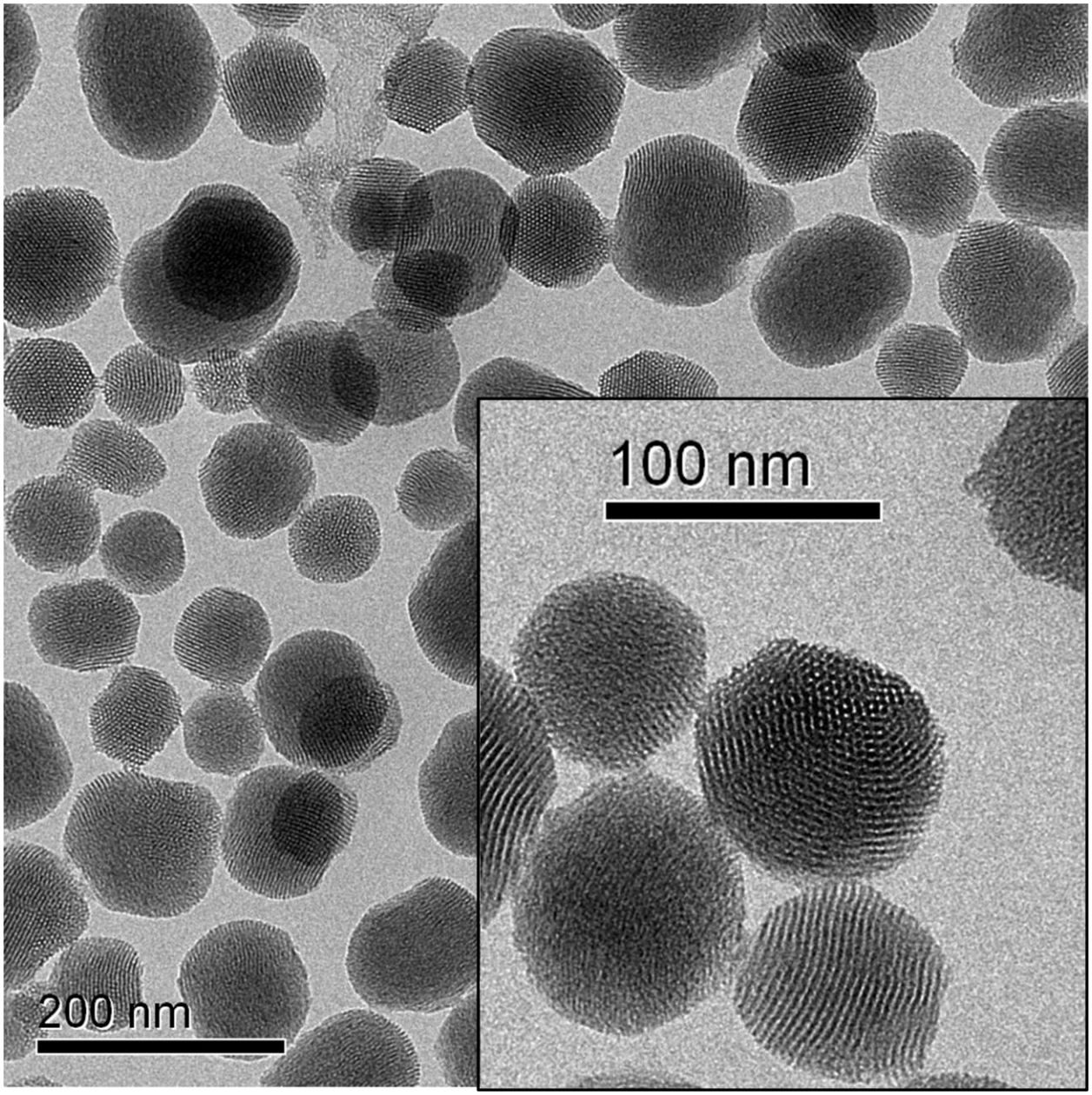

Figure 2.4. TEM image of a typical batch of MCM-41 type nanoparticles showing the ordered, 2D hexagonal mesopore phase. In a typical batch, particles range from 80-120 nm in diameter, with an average pore size of 2.2 nm.

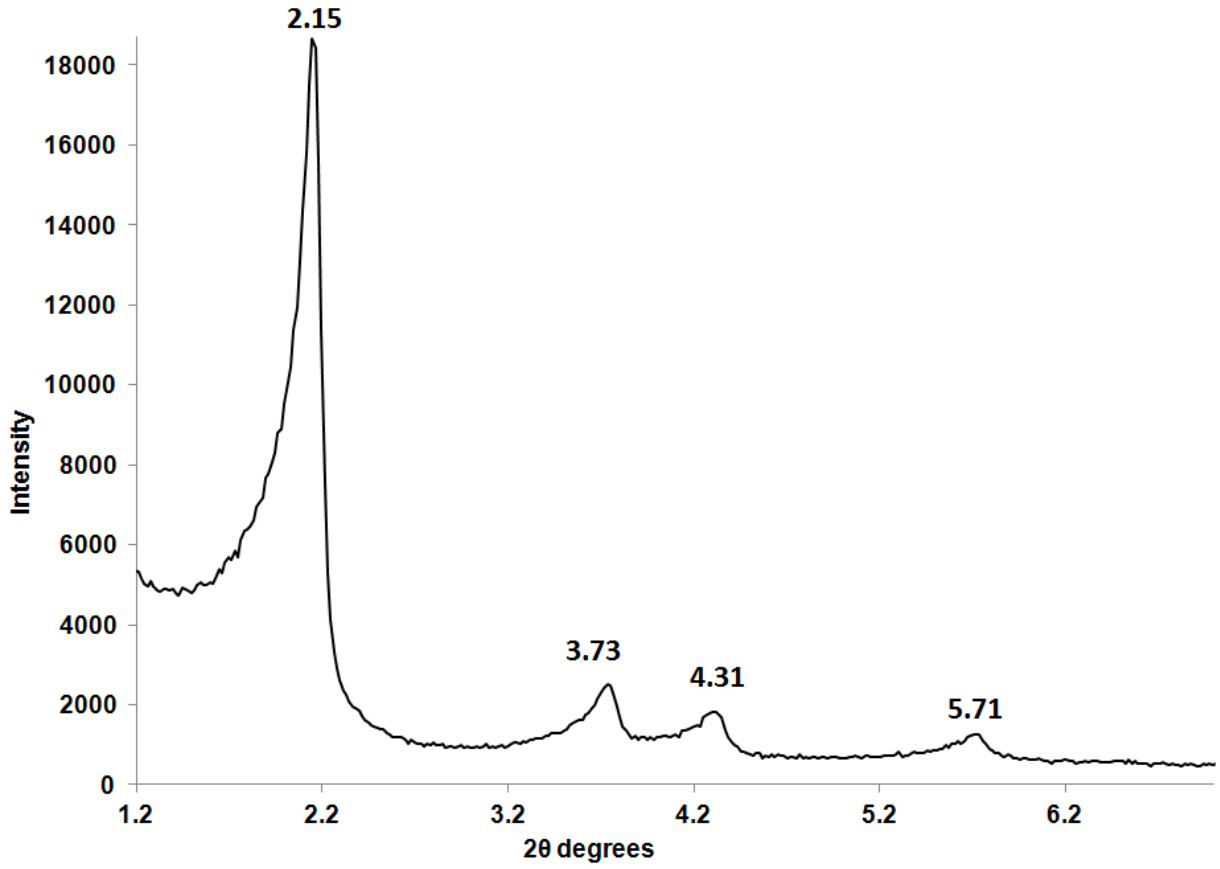

Figure 2.5. Powder XRD of synthesized MCM-41 nanoparticles. The primary peak appears at 2.15, with a lattice spacing of 4 nm to give a calculated pore diameter of ~2 nm, in close agreement with TEM images of the synthesized nanoparticles.

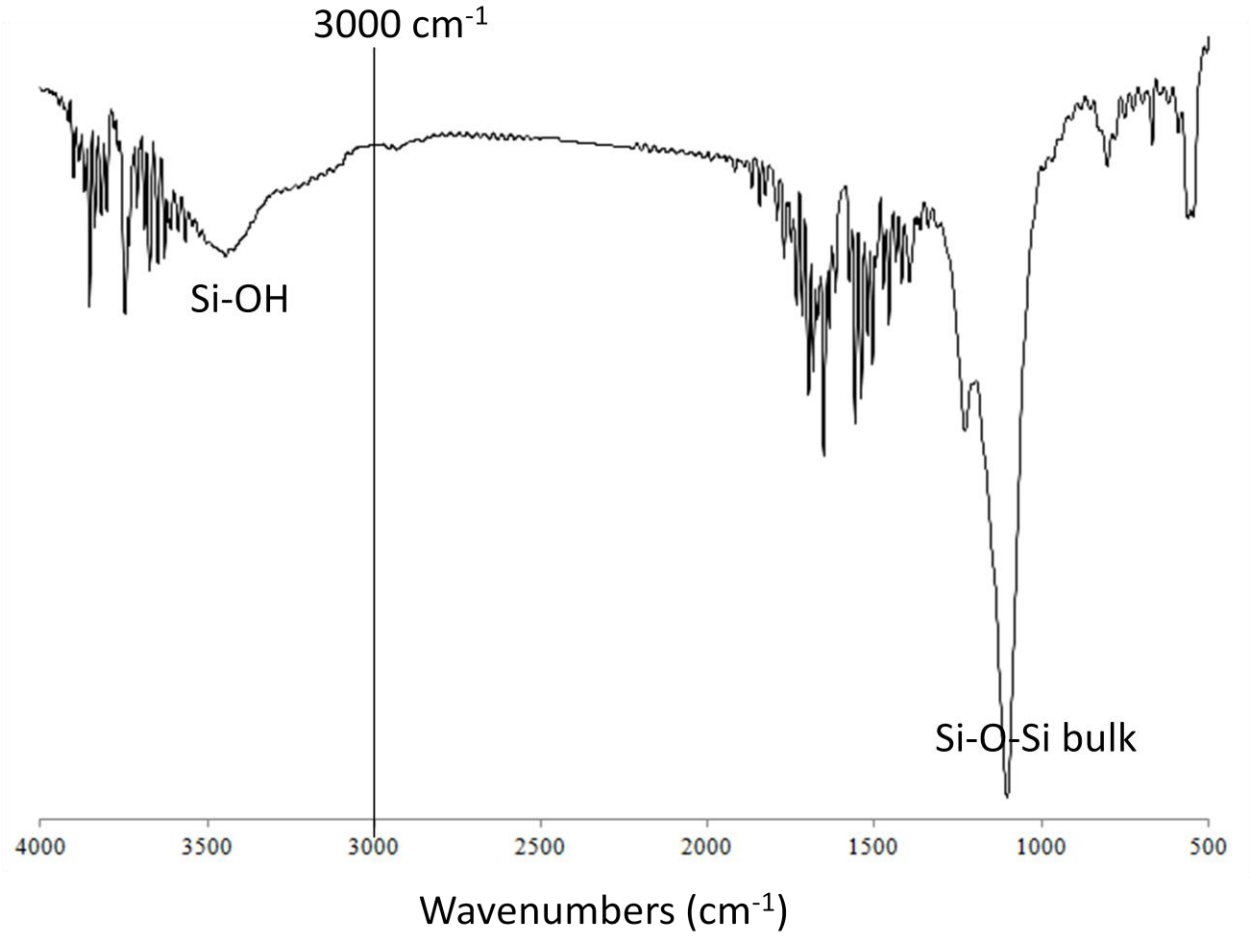

Figure 2.6. FTIR spectrum of surfactant extracted synthesized MSN. The absence of C-H stretching bands at 3000 cm^{-1} indicates complete removal of the surfactant templating agent CTAB.

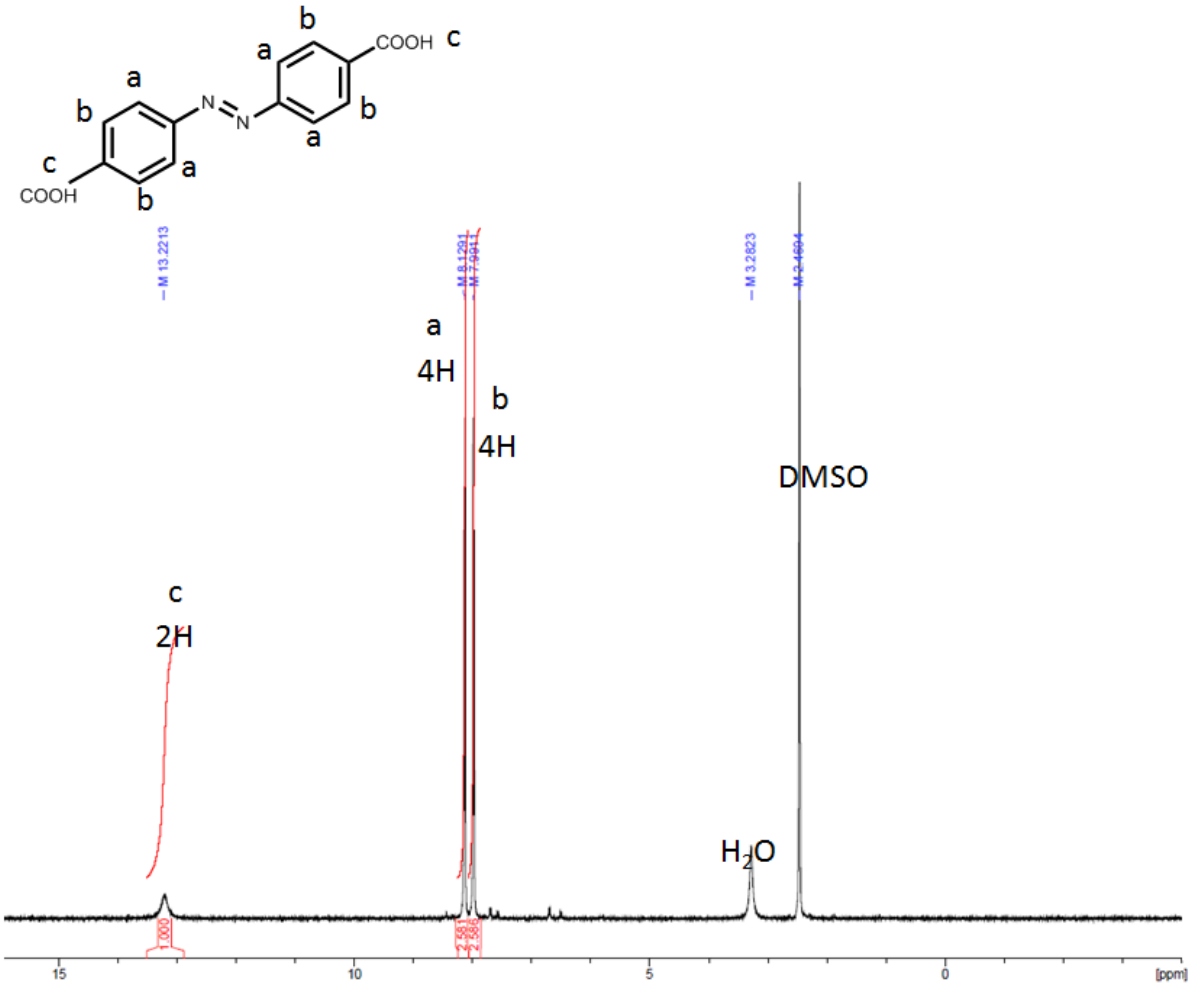

Figure 2.7. [1]HNMR spectrum of 4,4'-azobenzenecarboxylic acid in DMSO-d.

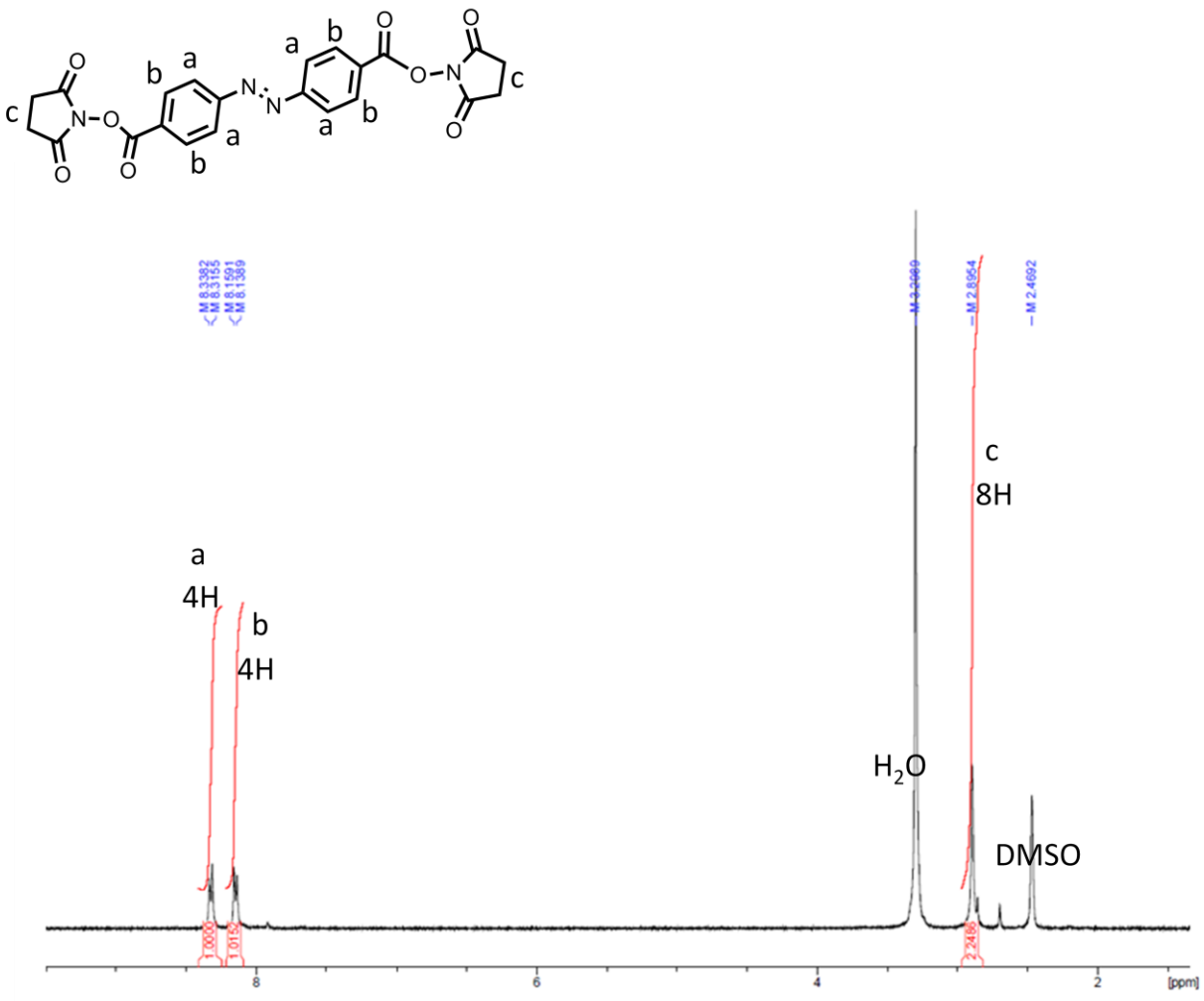

Figure 2.8. [1]HNMR spectrum of **2** in DMSO-d.

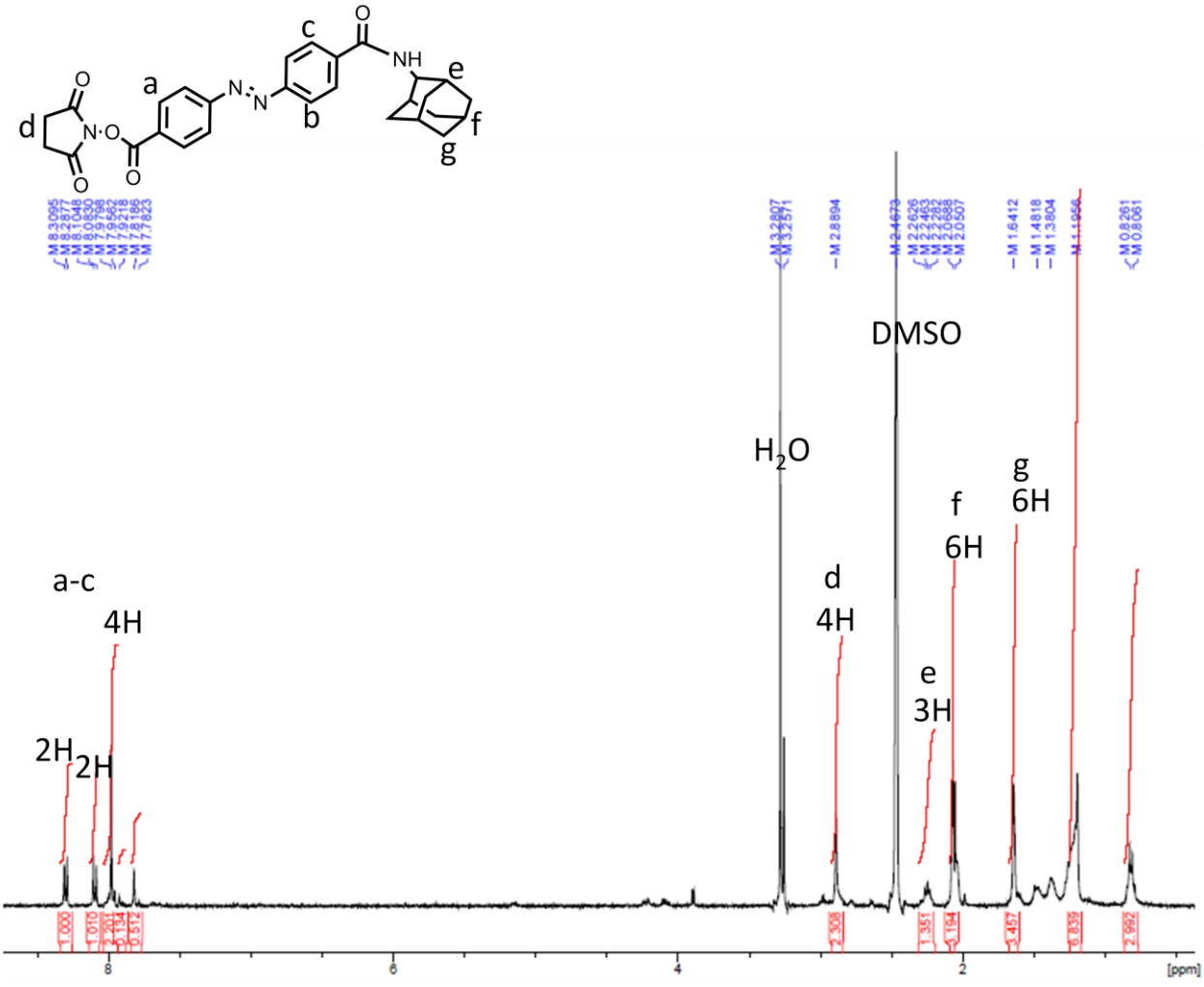

Figure 2.9a. [1]HNMR spectrum of **3a** DMSO-d.

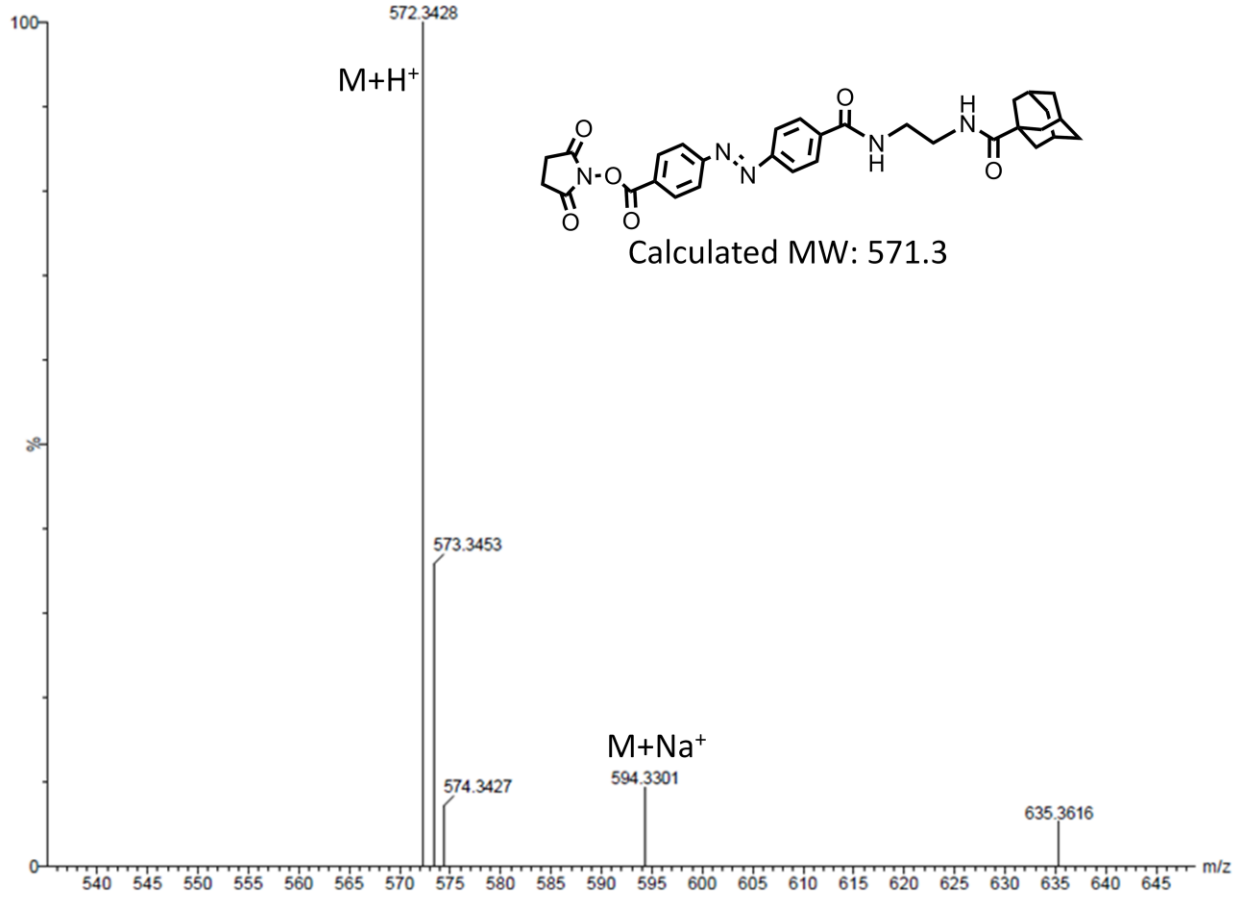

Figure 2.9b. ESI-TOF mass spectrum of **3a**.

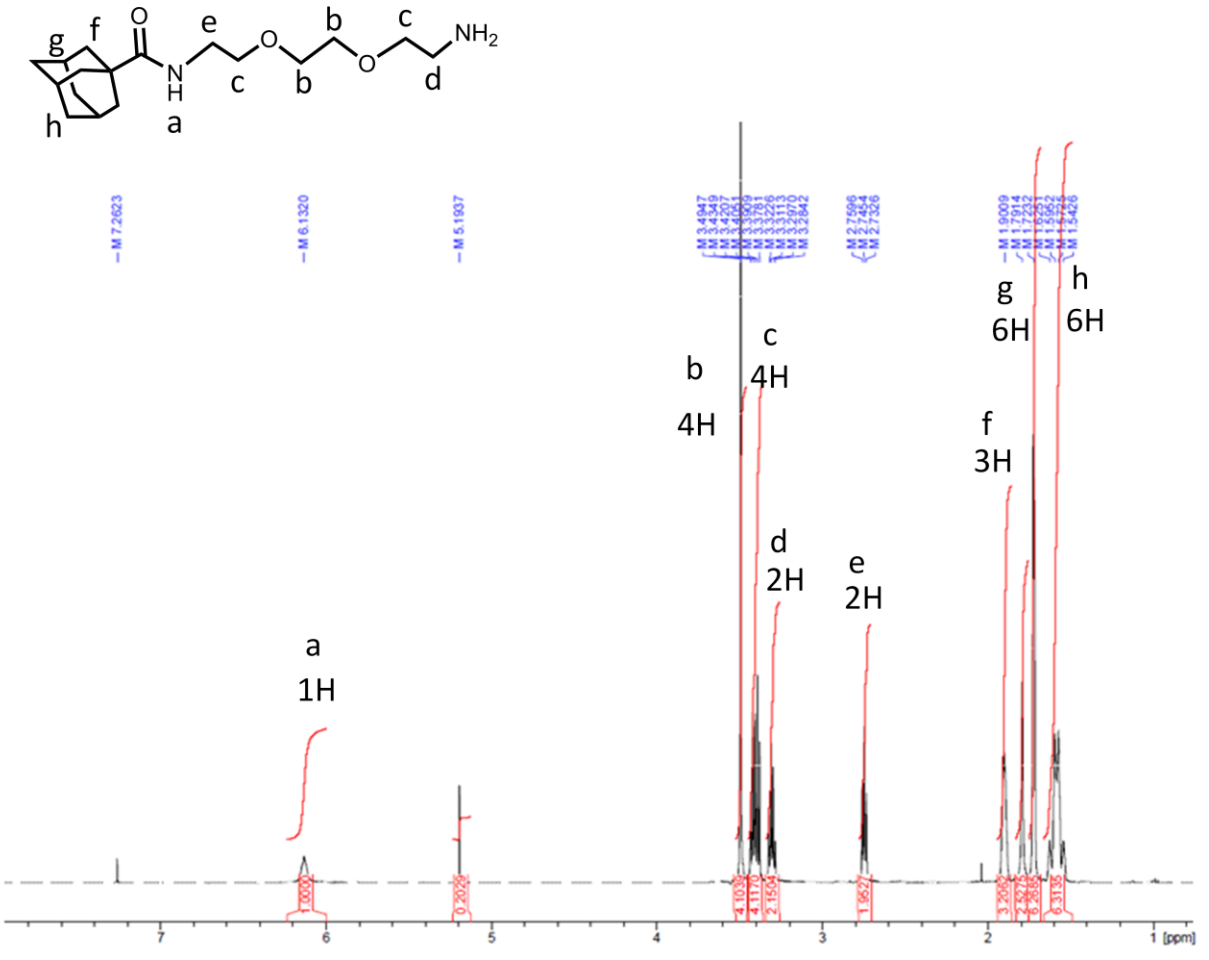

Figure 2.10. [1]HNMR spectrum of **2b** in chloroform-d.

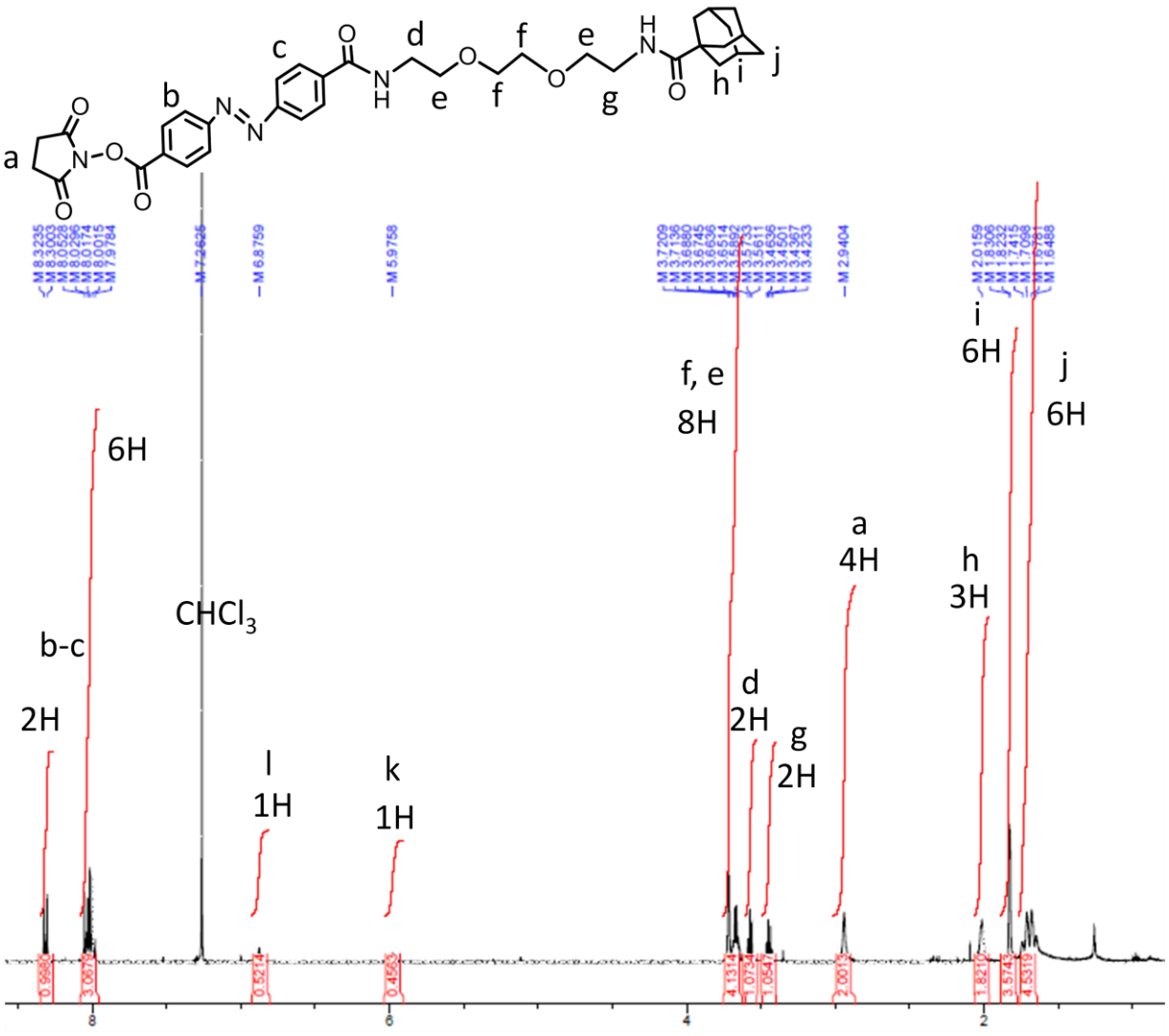

Figure 2.11a. [1]HNMR spectrum of **3b** in chloroform-d.

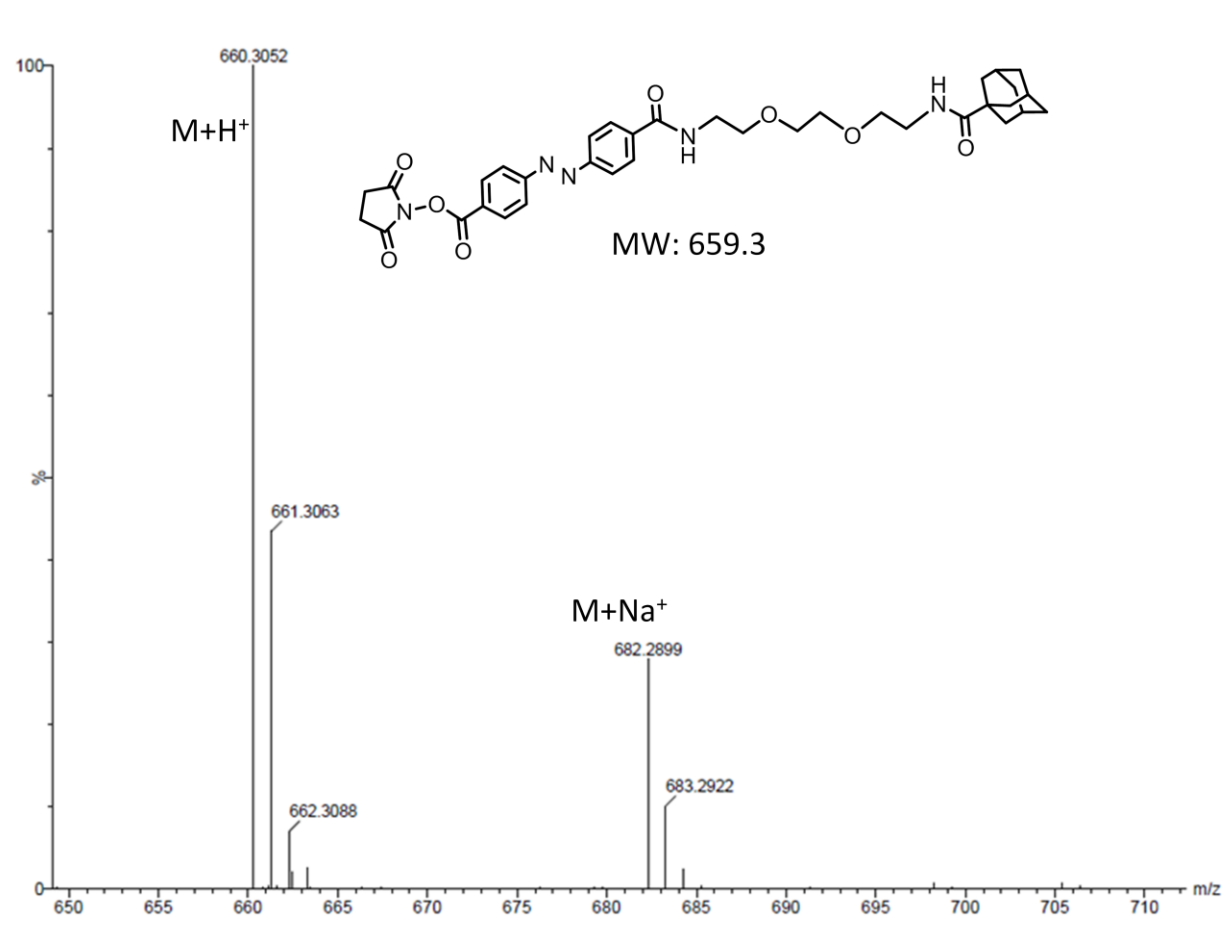

Figure 2.11b. ESI-TOF mass spectrum of **3b**.

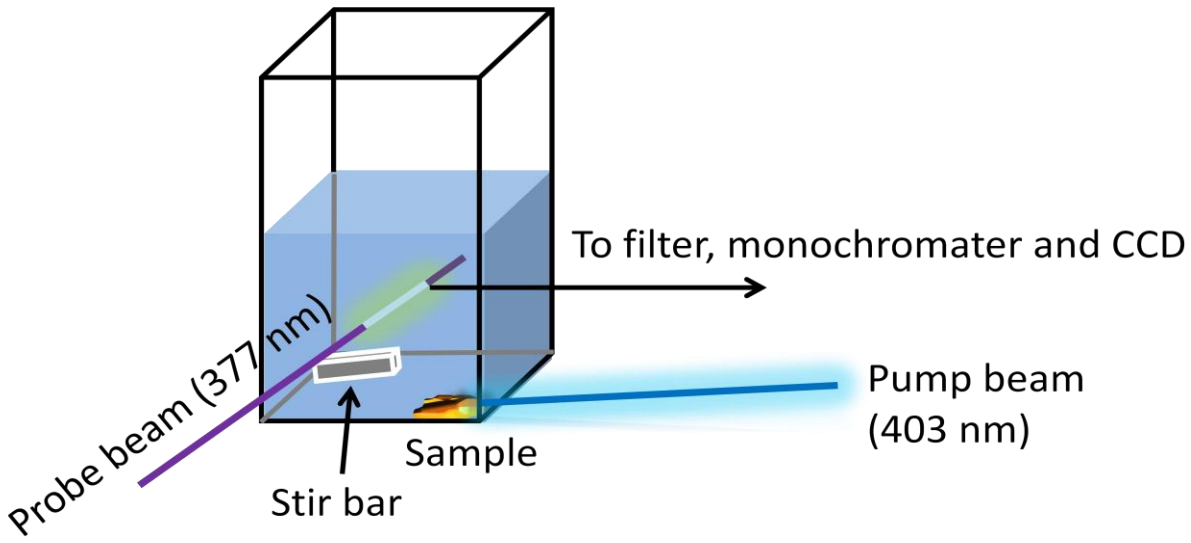

Figure 2.12. Experimental setup for time-resolved fluorescence spectroscopy measurements. An excitation beam (377 nm, 1mW, 1 mm) is aimed at the solution supernatant, exciting any dye molecules present. The corresponding emission is passed through a cutoff filter, and a monochromator before being read on a CCD detector cooled to liquid nitrogen temperatures. Computer software integrates the intensities at a specified wavelength in real-time to generate a release profile. To initiate release, a pump beam (403 nm, 85 mW, 1 mm) is turned on and focused directly onto the sample to induce *trans*- to *cis*-azobenzene photoisomerization.

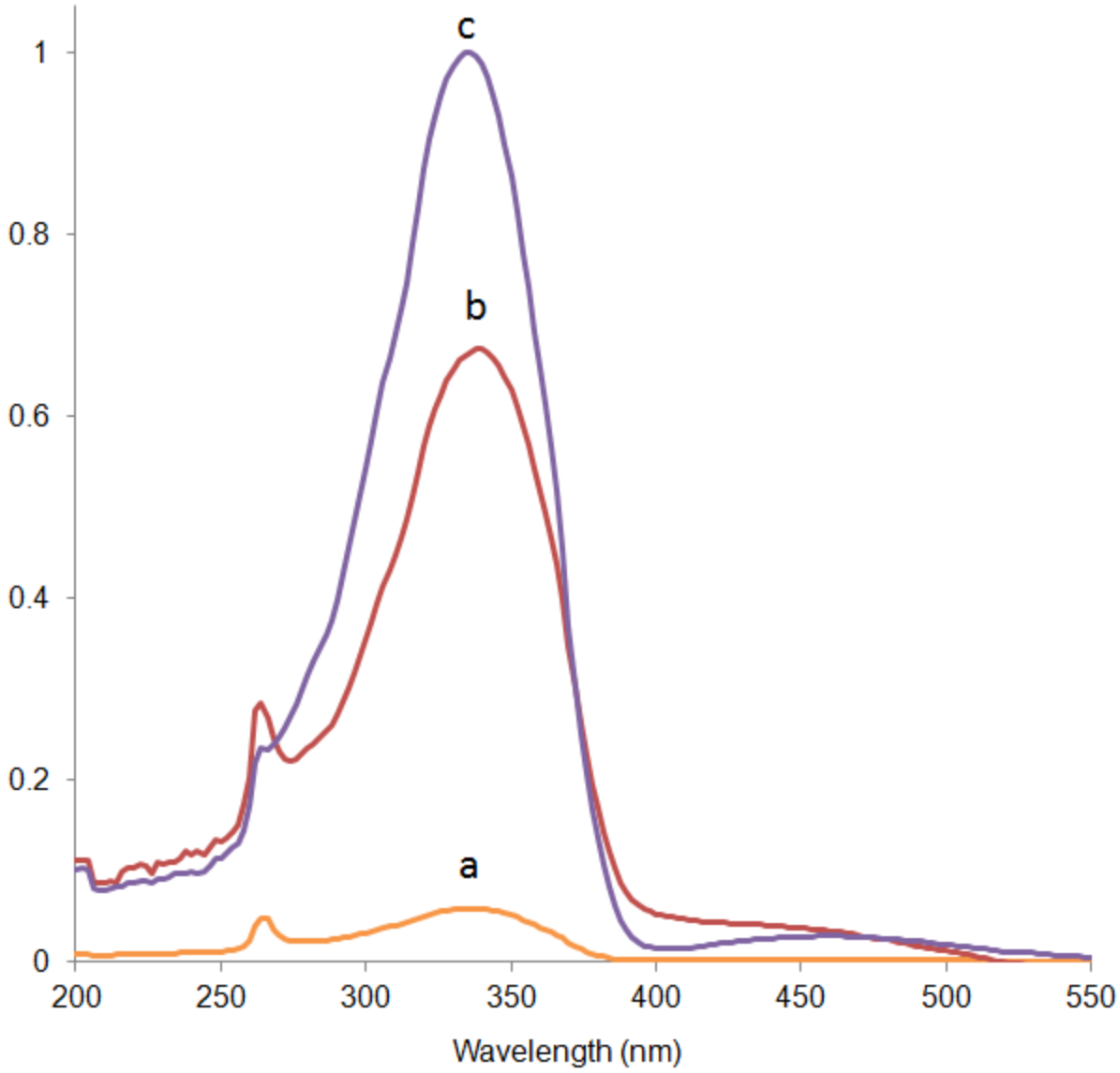

Figure 2.13. UV-Vis absorption spectra proving successful reaction between **4a** and APTES modified MSN. All absorption spectra were normalized to trace (c). Trace (c) shows the absorption of compound **4a** dissolved in DMF prior to reaction with APTES modified MSN. After modification, an absorption spectrum of the FRS1 attached nanoparticles in suspension is shown in trace (b). Finally, trace (a) shows the absorption of the supernatant solution after this attachment reaction has been completed, which indicates a successful reaction to attach the thread onto MSN.

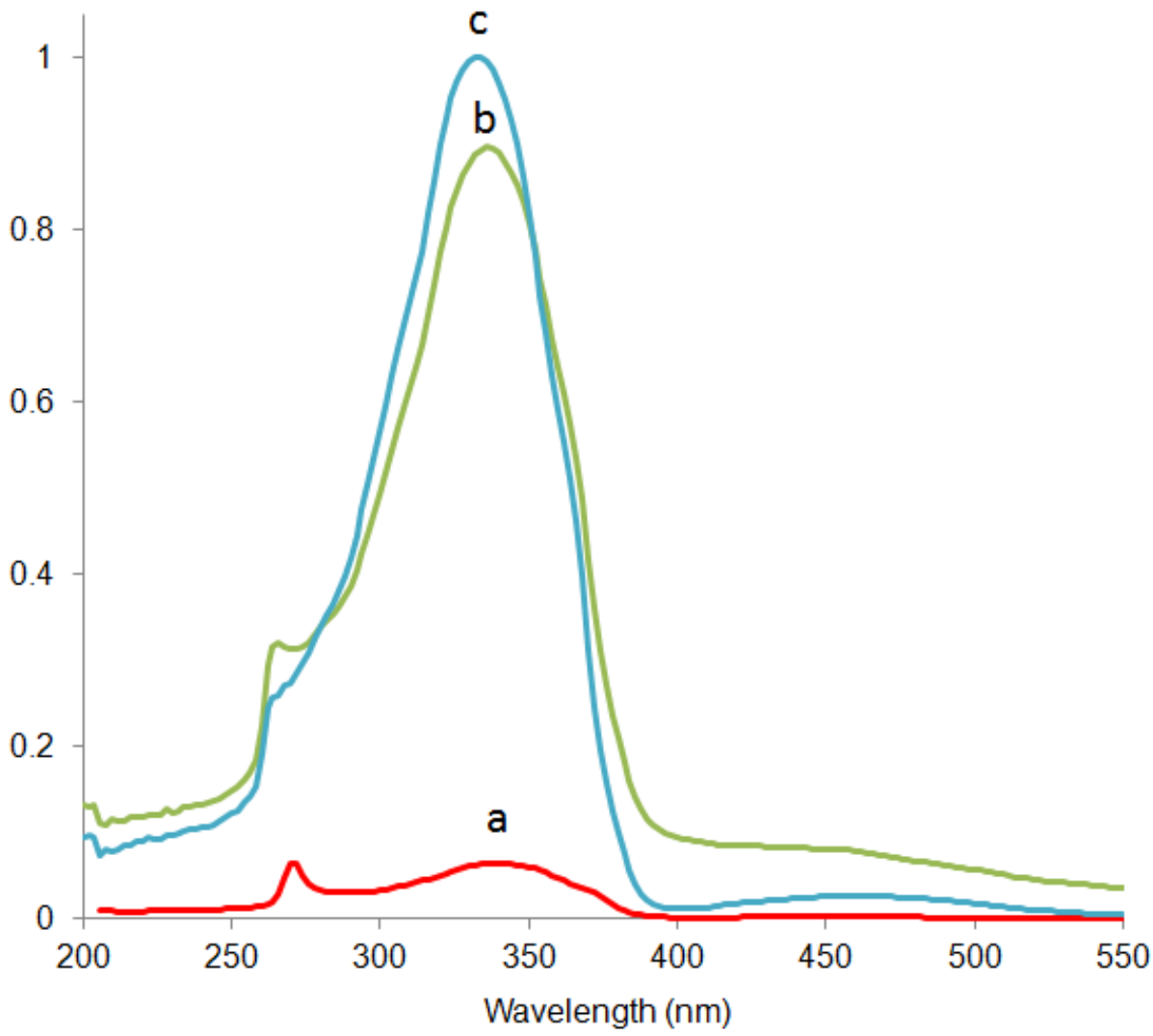

Figure 2.14. UV-Vis absorption spectra proving successful reaction between **4b** and APTES modified MSN. All traces were normalized to trace (c). Trace (b) shows the absorption of EXT2 attached MSN in suspension. Trace (c) shows the absorbance of thread **4b** dissolved in DMF prior to reaction with APTES modified MSN. Trace (a) shows the supernatant absorbance after the completed reaction, indicating that the thread has been successfully attached onto MSN.

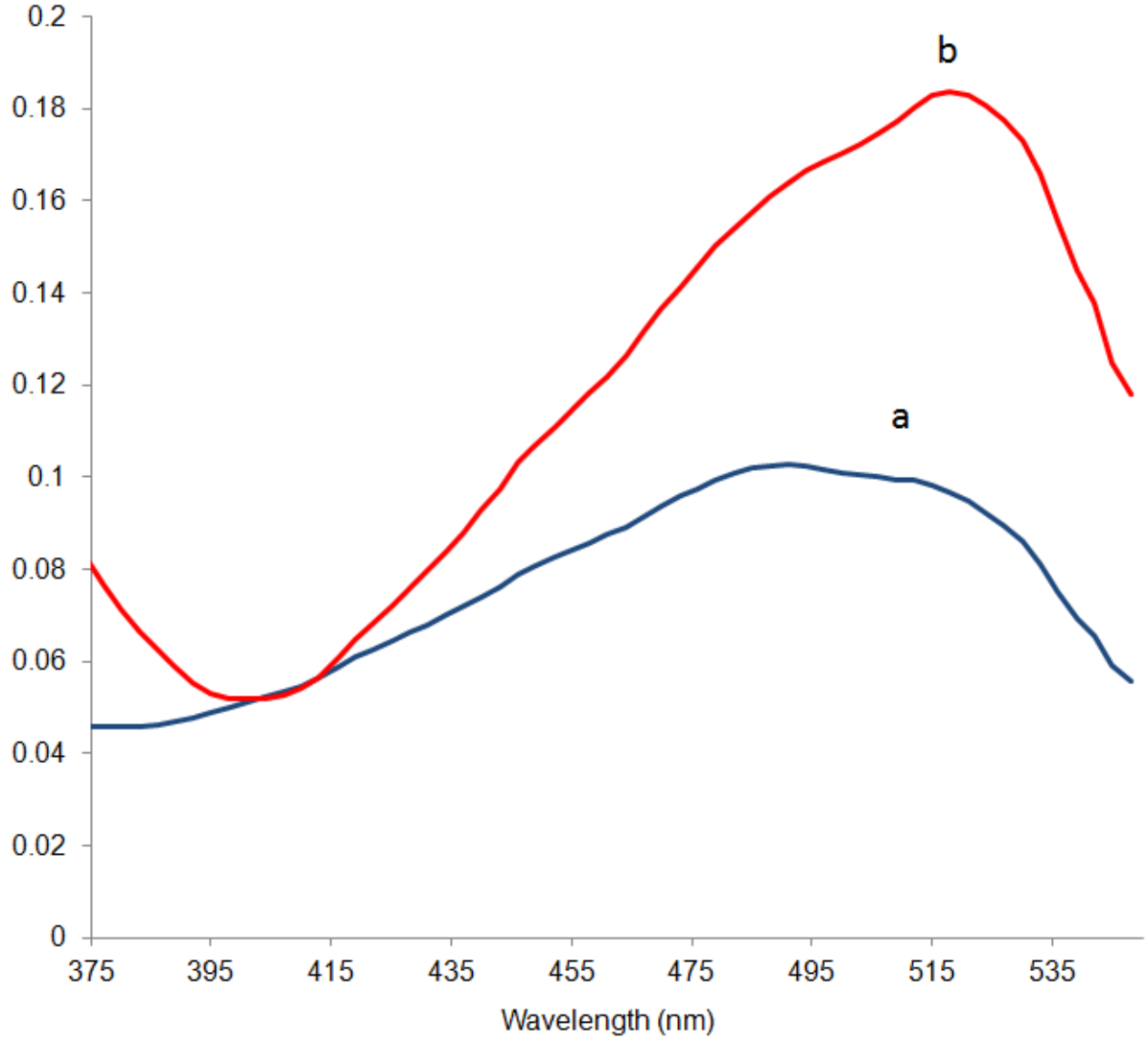

Figure 2.15. UV-Vis absorption spectra of supernatant after release of ARS from FRS1 machine. Trace (a) shows the absorbance of a 0.02 mM stock solution of ARS. Trace (b) shows the supernatant absorbance after a complete release from FRS1. Release weight percent was calculated from this trace to be 5%w.

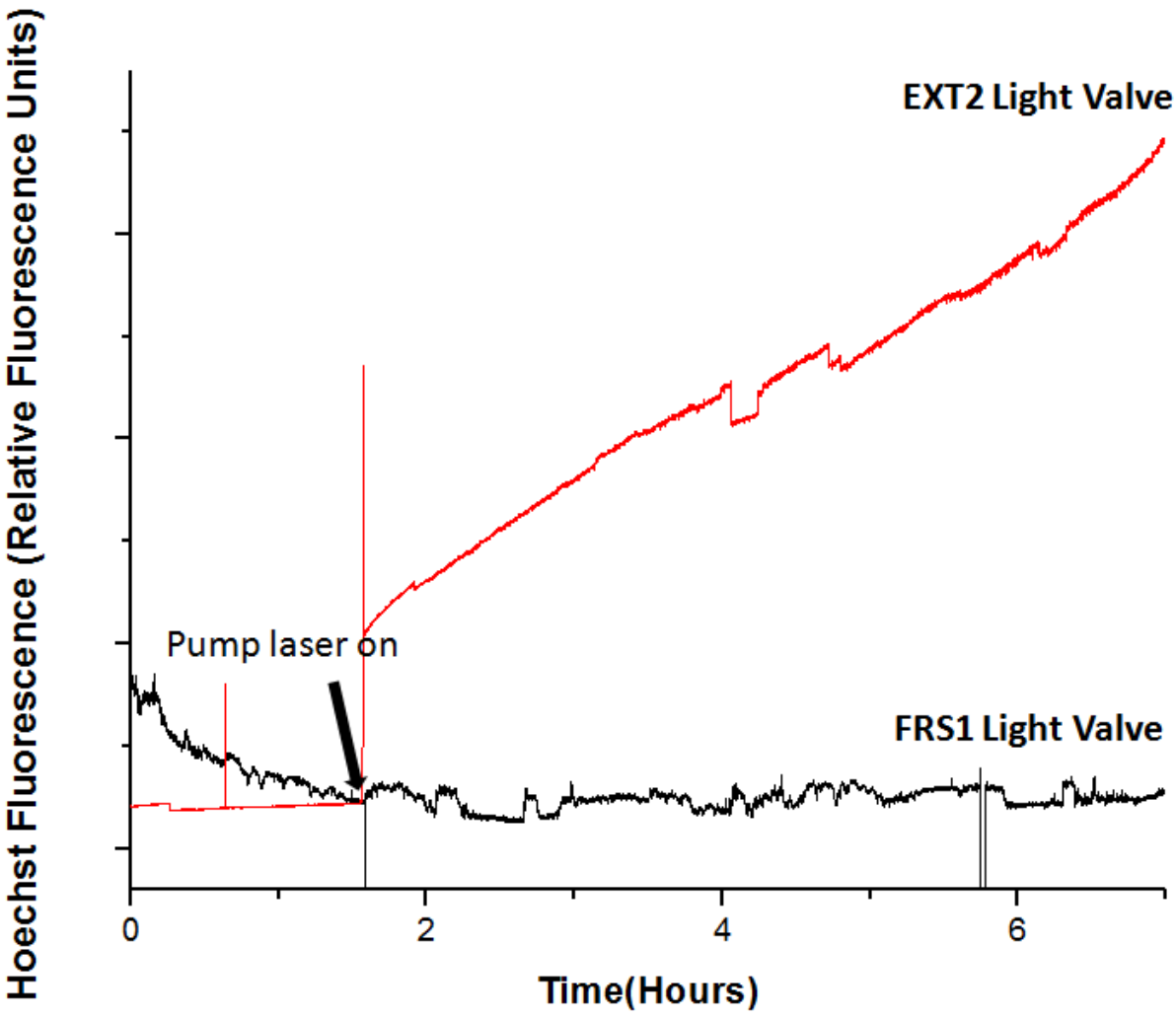

Figure 2.16. Continuous fluorescence monitoring of FRS1 MSN loaded with Hoechst 33342 dye. No definite slope change is observed when the pump laser is turned on, indicating that this design cannot store and release larger cargo such as Hoechst, while EXT2 MSN shows a distinct fluorescence increase when irradiated.

2.7 References

(1) Cheon, J.; Lee, J. H. *Acc. Chem. Res.* **2008**, 41, 1630-1640.

(2) Slowing, I. I.; Trewyn, G. B.; Giri, S.; Lin, S. V. *Adv. Funct. Mater.* **2007**, 17, 1225-1236.

(3) Lin, Y-S.; Hurley, K. R.; Haynes, C. L. *J. Phys. Chem. Lett.* **2012**, 3, 364-374.

(4)Kresge, C. T.; Leonowicz, M. E.; Roth, W. J.; Vartuli, J. C.; Beck, J. S. *Nature* **1992**, 359, 710-712.

(5) Beck, J. S.; Vartuli, J. C.; Roth, W. J.; Leonowicz, M. E.; Kresge, C. T.; Schmitt, K. D.; Chu, C. T. W.; Olson, D. H.; Sheppard, E. W. *J. Am. Chem. Soc.* **1992**, 114, 10834-10843.

(6) Liong, M.; Lu, J.; Kovochich, M.; Xia, T.; Ruehm, S. G.; Nel, A. E.; Tamanoi, F.; Zink, J. I. *ACS Nano* **2008**, *2*, 889-896.

(7) Ambrogio, M. W.; Thomas, C. R.; Zhao, Y.-L.; Zink, J. I.; Stoddart, J. F. *Acc. Chem. Res.* **2011**, 44, 903-913.

(8) Trewyn, B. G.; Slowing, I. I.; Giri, S.; Chen, H.-T.; Lin, V. S. Y. *Acc. Chem. Res.* **2007**, 40, 846-853.

(9) Zhang, H.; Dunphy, D. R.; Jiang, X.; Meng, H.; Sun, B.; Tarn, D.; Xue, M.; Wang, X.; Lin, S.; Ji, Z.; Li, R.; Garcia, F. L.; Yang, J.; Kirk, M. L.; Xia, T.; Zink, J. I.; Nel, A.; Brinker, C. J. *J. Am. Chem. Soc.* **2012**, 134, 15790-15804.

(10) Yanes, R. E.; Tarn, D.; Hwang, A. A.; Ferris, D. P.; Sherman, S. P.; Thomas, C. R.; Lu, J.; Pyle, A. D.; Zink, J. I.; Tamanoi, F. *Small* **2013**, 9, 697-704.

(11) Lu, J.; Liong, M.; Zink, J. I.; Tamanoi, F. *Small* **2007**, 3, 1341-1346.

(12) Meng, H.; Xue, M.; Xia, T.; Zhao, Y.-L.; Tamanoi, F.; Stoddart, J. F.; Zink, J. I.; Nel, A. E. *J. Am. Chem. Soc.* **2010**, 132, 12690-12697.

(13) Angelos, S.; Yang, Y-W.; Khashab, N. M.; Stoddart, J. F.; Zink, J. I. *J. Am. Chem. Soc.* **2009**, 131, 11344-11346.

(14) Li, Z.; Nyalosaso, J. L.; Hwang, A. A.; Ferris, D. P.; Yang, S.; Derrien, G.; Charnay, C.; Durand, J.-O.; Zink, J. I. *J. Phys. Chem. C.* **2011**, 115, 19496-19506.

(15) Coti, K. K.; Belowich, M. E.; Liong, M.; Ambrogio, M. W.; Lau, T. A.; Khatib, H. A.; Zink, J. I.; Khashab, N. M.; Stoddart, J. F. *Nanoscale* **2009**, 1, 16-39.

(16) Vivero-Escoto, J. L.; Slowing, I. I.; Trewyn, B. G.; Lin, V. S.-Y. *Small* **2010**, 6, 1952-1967.

(17) Lai, C.-Y.; Trewyn, B. G.; Jeftinija, D. M.; Jeftinija, K.; Xu, S.; Jeftinija, S.; Lin, V. S. Y. *J. Am. Chem. Soc.* **2003**, 125, 4451-4459.

(18) Lu, J.; Choi, E.; Tamanoi, F.; Zink, J. I. Small **2008**, 4, 421-426.

(19) Liu, J. W.; Stace-Naughton, A.; Jiang, X. M.; Brinker, C. J. *J. Am. Chem. Soc.* **2009**, 131, 1354-1355.

(20) Ferris, D. P.; Lu, J.; Gothard, C.; Yanes, R.; Thomas, C. R.; Olsen, J.-C.; Stoddart, J. F.; Tamanoi, F.; Zink, J. I. *Small* **2011**, 7, 1816-1826.

(21) Tarn, D.; Xue, M.; Zink, J. I. *Inorg. Chem.* **2013**, 52, 2044-2049.

(22) Thomas, C. R.; Ferris, D. P.; Lee, J.-H.; Choi, E.; Cho, M. H.; Kim, E. S.; Stoddart, J. F.; Shin, J.-S.; Cheon, J.; Zink, J. I. *J. Am. Chem. Soc.* **2010**, 132, 10623-10625.

(23) Ferris, D.P.; Zhao, Y.-L.; Khashab, N.M.; Khatib, H.A.; Stoddard, J.F.; Zink, J. I. *J. Am. Chem. Soc.* **2009**, 131, 1686-1688.

(24) Nguyen, T. D.; Leung, K. C.-F.; Liong, M.; Liu, Y.; Stoddart, J. F.; Zink, J. I. *Adv. Funct. Mater.* **2007**, 17, 2101–2110.

(25) Angelos, S.; Choi, E.; Vo¨gtle, F.; De Cola, L.; Zink, J. I. *J. Phys. Chem. C* **2007**, 111, 6589–6592.

(26)Aznar, E.; Casasu´s, R.; Garcı´a-Acosta, B.; Marcos, M. D.; Martı´nez-Ma´n˜ez, R.; Sanceno´n, F.; Soto, J.; Amoro´s, P. *Adv. Mater.* **2007**,19, 2228–2231.

(27) Murakami, H.; Kawabuchi, A.; Kotoo, K.; Kunitake, M.; Nakashima, N. *J. Am. Chem. Soc.* **1997**, 119, 7605-7606.

(28) Del Valle, E. M. M. *Process Biochem.* **2004**, 39, 1033-1046

(29) Falvey, P.; Lim, C. W.; Darcy, R.; Revermann, T.; Karst, U.; Giesbers, M.; Marcelis, A. T. M.; Lazar, A.; Coleman, A. W.; Reinhoudt, D. N.; Ravoo, B. J. Chem. Eur. J. 2005, 11, 1171-1180.

(30) Cromwell, W. C.; Bystrom, K.; Eftink, M. R. *J. Phys. Chem.* **1985**, 89, 326-332.

(31) Angelos, S.; Liong, M.; Choi, E.; Zink, J. I. *Chemical Engineering Journal* **2008**, 137, 4-13.

(32) Rabek, J. F. *Photochemistry and Photophysics, Volume II,* CRC Press, Inc: Boca Raton, Florida, **1990.**

CHAPTER 3

Application of a Pseudorotaxane-Based Azobenzene-Cyclodextrin Light Valve for the *In Vitro* Delivery of Doxorubicin and Hoechst 33342

3.1 Abstract

A pseudorotaxane-based, light activated nanovalve consisting of *β*-cyclodextrin complexed to 4-(3-triethoxysilylpropylureido)azobenzene on mesoporous silica nanoparticles (MSN) was used to deliver the anti-cancer drug Doxorubicin and nuclear stain Hoechst 33342 *in vitro* to a MiaPaCa-2 cancer cell model. Using this design, it was found that the functionalized MSN were endocytosed by cells and localize in the cellular lysosomal compartments and with light irradiation (403 nm), deliver Hoechst or Doxorubicin *in vitro*. The delivery of Doxorubicin with this nanovalve resulted in high levels of cancer cell death.

3.2 Introduction

With drug delivery being one of the potentially most important applications of these mechanized MSN,[1, 2, 3, 4 5, 6, 7, 8, 9, 10] responding to stimuli inside the cell is the most common form of activation. An alternative approach involves the use of light as an external stimulus to cause a chemical change.[11, 12, 13, 14] The preparation of an azobenzene (AB) derivative from 4-(3-triethoxysilylpropylureido)azobenzene (TSUA)[15, 16, 17] to give modified MSN resulted in the binding and the light-operated dissociation of a pyrene-modified *β*-cyclodextrin (Py-*β*-CD) with the TSUA stalks on the surfaces of the MSN, and the light-operated release of Rhodamine B (RhB) upon dissociation the *β*-CD rings from the TSUA stalks. Irradiating AB with 351 nm light causes AB to isomerize from the more stable *trans* to the less stable *cis* configuration. In the case of MSN carrying AB-containing stalks, *β*-CD will thread onto the stalks and bind to *trans*-AB units, thus sealing the nanopores and stopping release of the cargo. By contrast, upon irradiation (351 nm), the isomerization of *trans*-to-*cis* AB units leads to the dissociation of *β*-CD rings from the stalks, thus opening the gates to the nanopores and releasing the cargo. The synthesis and mode of activation of these mechanized MSN are summarized in Figure 3.1. A release profile showing the light-activated release of RhB using this system is illustrated in Figure 3.2**.**

The 80-120 nm MSN used in these studies have been shown to be readily endocytosed by cancer cells and are non-cytotoxic.[18, 19] Once uptaken, they are observed to localize in the cellular lysosomal compartments (Figure 3.3a), [18] which has a pH between 5-7.[20] This has led to the development of pH sensitive nanovalves for cargo delivery. [21, 22, 23, 24, 25] As an alternative to pH activation, once endocytosed, MSN functionalized with a light-activated nanovalve can be irradiated with light (Figure 3.3b) to externally induce cargo release (Figure 3.3c). After demonstrating the successful synthesis and characterization of this pseudorotaxane-based,

azobenzene-cyclodextrin light activated nanovalve,[26] its functioning was tested *in vitro*; in this chapter, we demonstrate the release of both anti-cancer drug Doxorubicin (Dox) and a nuclear stain, Hoechst 33342 to MiaPaCa-2 pancreatic cancer cells.

3.3 Results and Discussion

3.3.1 Synthesis of TSUA MSN

MSN were constituted and functionalized by known procedures (See Chapter 1.3.1). The structures of the MSN were elucidated by X-ray diffraction, and the sizes of the MSN were obtained by dynamic light scattering. The AB-containing organosilane TSUA was prepared and linked to MSN by reacting 4-aminoazobenzene with 3-aminopropyltriethoxysilane in an organic solvent. Attachment of TSUA to MSN was confirmed by UV-vis spectroscopy, in which TSUA modified MSN exhibited characteristic absorption peaks of free TSUA. The release of both the Py-β-CD and the RhB cargo from the MSN is monitored by luminescence spectroscopy. A small amount of the solid MSN is placed in the corner of an optical cuvette, and a small stir bar and H_2O are carefully added to avoid disturbing the MSN. A 351 nm excitation beam is directed onto the liquid above the MSN to excite the Py-β-CD and RhB that are released from the MSN into solution under gentle stirring. The maximum amount of cap or cargo that is released is determined by measuring the intensity (excited by the probe beam) after a long period (>400 min) of excitation. A plot of the percent Py-β-CD released as a function of time (the release profile) is shown in Figure 3.2, which shows a concurrent release of RhB along with the β-CD cap.

3.3.2 *In Vitro* Release of Hoechst 33342 and Doxorubicin

After confirming the successful operation of the TSUA nanovalve in solution, we applied this system for its use in biology. In these experiments, a MiaPaCa-2 pancreatic cancer cell model was applied. Treating these cells with TSUA-MSN resulted in nanoparticle endocytosis and lysosomal localization (Figure 3.3a), where the nanovalve can be activated by light irradiation (Figure 3.3b), resulting in release of Hoechst 33342 or Doxorubicin cargo (Figure 3.3c). The *in vitro* release of Hoechst was determined through cellular nuclei staining with cargo release, and the release of Dox through monitoring cellular death as a result of Dox-induced cellular death. Fluorescence labeling of the TSUA-MSN with fluorescein allowed for *in vitro* imaging of the cells.

To verify the surface modification of MSN with TSUA does not affect endocytosis and lysosomal uptake, MiaPaCa-2 cells were stained with LysoTracker Red before treating with fluorescein (FITC) labeled TSUA-MSN. Figure 3.4 illustrates the locations of the fluorescently labeled TSUA-MSN nanoparticles are traceable through their green fluorescence (Figure 3.4, far right). In the middle frame of Figure 3.4, red fluorescence indicates the locations of the cell lysosomes, some of which align with the green fluorescence of FITC TSUA-MSN in the merged image (Figure 3.4, far left). The significant colocalization suggests that modifying MSN with TSUA does not affect its lysosomal uptake, and that treating the cells with TSUA-MSN results in lysosomal localization of the nanoparticles.

Upon confirming the uptake of TSUA-MSN by cells, the light-activated release of cargo was demonstrated by treating the cells with TSUA-MSN loaded with Hoechst 33342 nuclear stain. This dye exhibits a large blue shift when intercalated with DNA where it appears blue,[27] allowing for its clear visualization when delivered. Confocal imaging of cells treated with

Hoechst loaded TSUA-MSN show no nuclei staining in dark conditions (Figure 3.5, lower frame, middle image), indicating that Hoechst is tightly stored within the MSN pores by the TSUA nanovalves. When subjected to light irradiation, cells treated with Hoechst loaded TSUA-MSN show high levels of nuclear staining (Figure 3.5, upper frame, middle image), demonstrating the light dependent release of cargo. Merging the blue fluorescence channel (Figure 3.5, upper frame, middle image) with the bright field image (Figure 3.5, upper frame, left image) colocalizes the blue staining with the cell nuclei (Figure 3.5, upper frame, right image), confirming nuclear staining as a result of Hoechst release.

The red intrinsic fluorescence of Doxorubicin can allow for its traceability under confocal imaging, but differentiating between cargos trapped within MSN and the released cargo is difficult. Therefore, the release of Doxorubicin from TSUA-MSN was visualized by monitoring cellular viability after treatment with Dox loaded TSUA-MSN. In a similar fashion as described, MiaPaCa-2 cancer cells were treated with Dox loaded TSUA-MSN. After being endocytosed, the cells were irradiated with 403 nm light to induce cargo release of the endocytosed TSUA-MSN. Figure 3.6 shows that both Dox loaded TSUA-MSN and unloaded TSUA-MSN are non-cytotoxic to cells in the absence of light at a concentration of 20 μg/mL. When subjected to light irradiation, the sample treated with Dox loaded TSUA-MSN shows a large increase in cell killing, which can be attributed to the release of its cargo (Figure 3.6). In this sample, the amount of observed cell death is directly proportional to the laser power, where presumably higher power results in more release of Dox; an almost complete cell killing was observed after irradiating with 100 mW of laser power. Comparing these results with the no observed cell killing in the dark conditions indicates that light irradiation of Dox loaded TSUA-MSN results in cargo delivery and subsequent cell death. It is important to note that irradiation of a group of

cells where nanoparticles were excluded resulted in no cell death at both 50 and 100 mW of laser power (Figure 3.6, right bars). Interestingly, cell killing was also observed in a cell set treated with unloaded TSUA-MSN (Figure 3.6, middle bars). Although this sample shows no toxicity in the dark, light irradiation of the sample resulted in cell death. One possibility for this observed toxicity ROS generation[28] through the light-induced degradation of azobenzene. This result warrants further photochemical investigation of TSUA.

3.4 Summary

In summary, a pseudorotaxane-based, light-activated azobenzene-cyclodextrin nanovalve was used to for the *in-vivo* delivery of Hoechst 33342 and Doxorubicin in MiaPaCa-2 cells. The lysosomal localization of TSUA-MSN was verified by confocal imaging, showing colocalization of fluorescently labeled nanoparticles with LysoTracker Red labeled lysosomes. Cells treated with Hoechst loaded TSUA-MSN exhibited bright nuclear staining when irradiated with 403 nm light as compared to a non-irradiated control group. TSUA-MSN nanoparticles loaded with Doxorubicin showed high levels of cell killing when irradiated with light, but no toxicity in the dark.

3.5 Figures

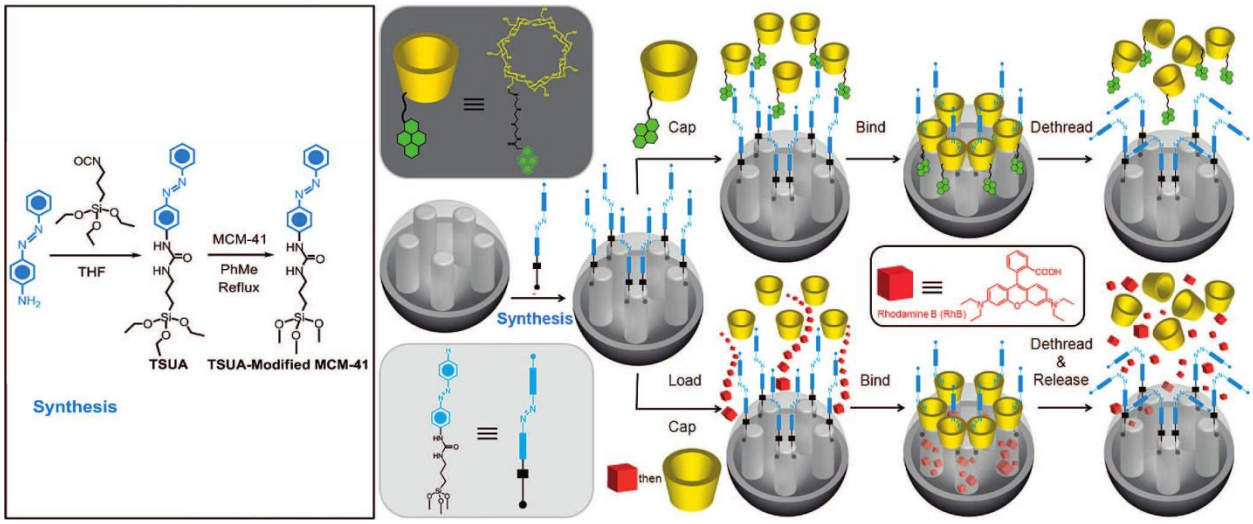

Figure 3.1. Synthesis of TSUA -modified MSN. Two approaches to the operation and function of the AB-modified MSN carrying nanovalves. Py-*β*-CD or *β*-CD threads onto the *trans*-AB stalks to seal the nanopores. Upon irradiation (351 nm), the isomerization of *trans*-to-*cis* AB units leads to the dissociation of Py-*β*-CD or *β*-CD rings from the stalks, thus opening the gates to the nanopores and releasing the cargo.[26]

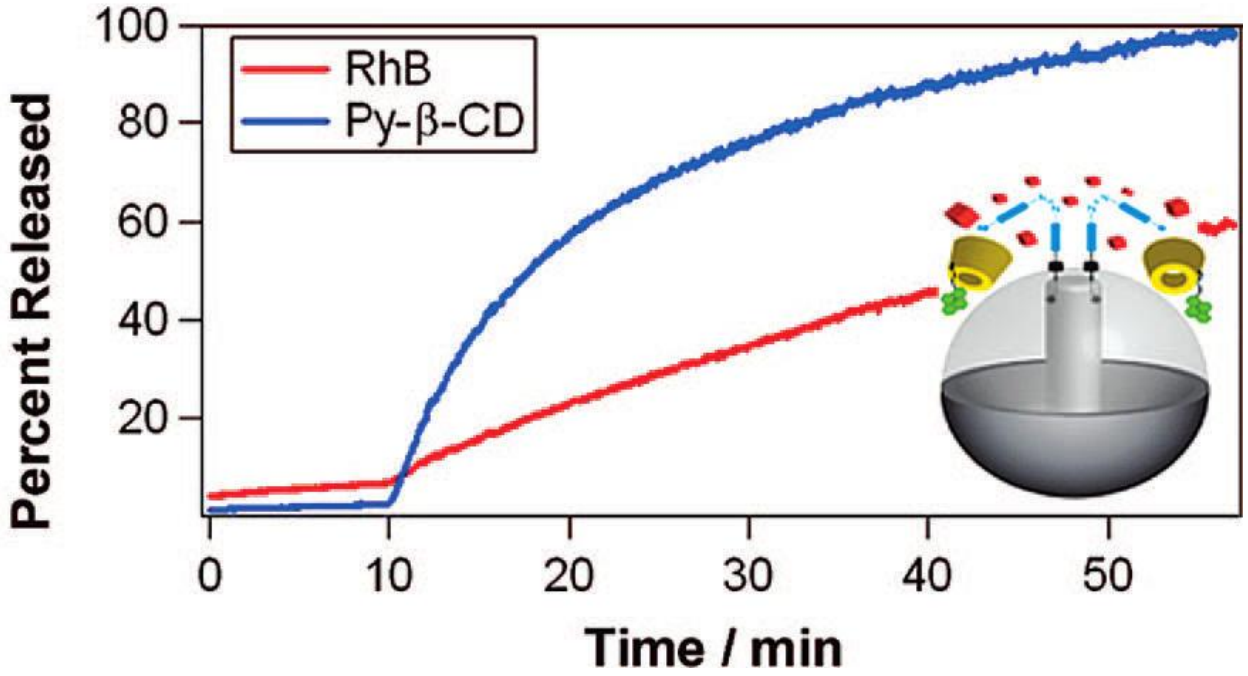

Figure 3.2. Release profile for TSUA modified nanoparticles. Upon light irradiation of TSUA modified nanoparticles (10 minutes), both RhB and Py-*β*-CD are observed to release. This concurrent release indicates that cargo release requires displacement of the cap.[26]

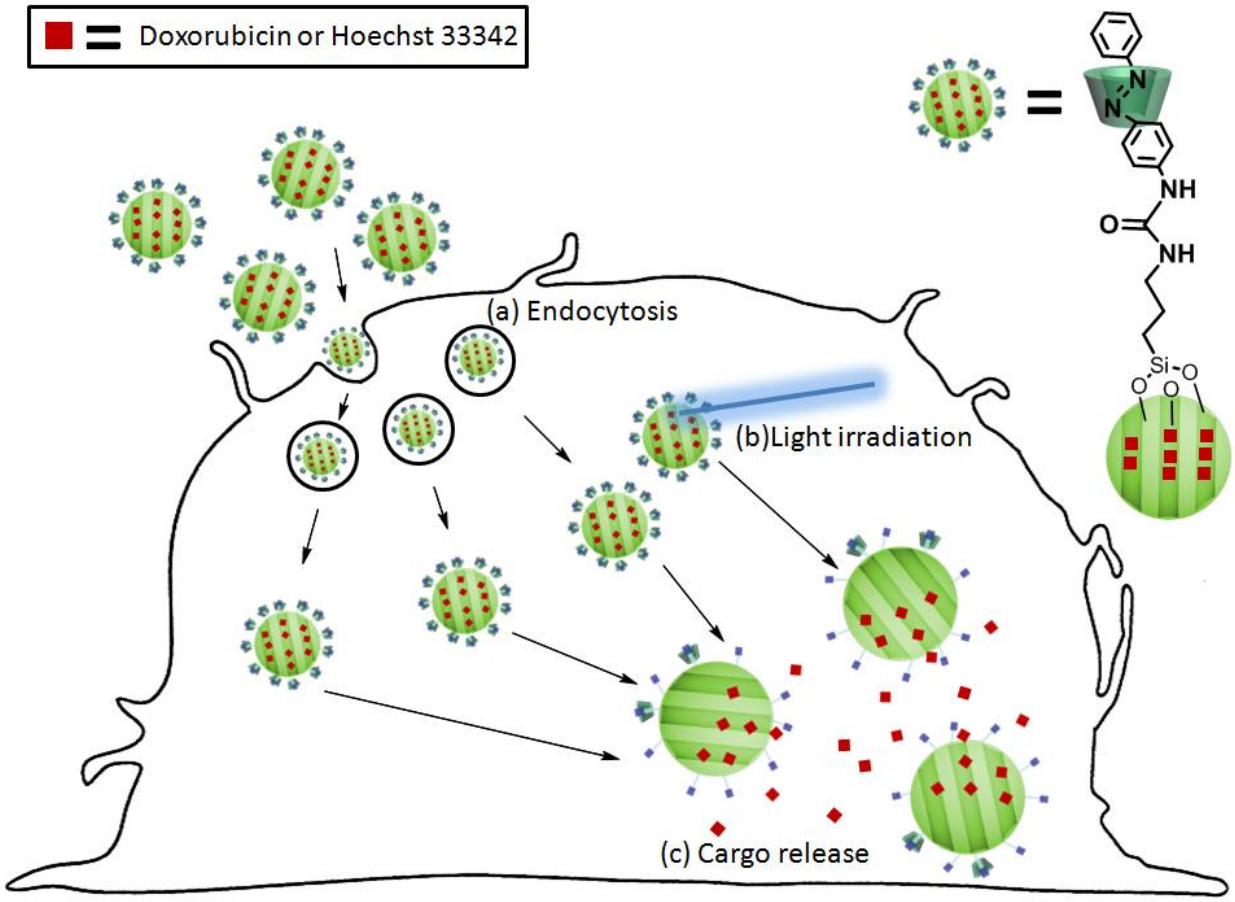

Figure 3.3. Cellular uptake of TSUA modified MSN. (a) Endocytosis of the nanoparticles results in cellular uptake. (b) Light irradiation of these nanoparticles results in *trans*- to *cis*- azobenzene isomerization and subsequent (c) cargo release. The released cargo can be visualized by fluorescent staining of the cellular nuclei (Hoechst 33342), or indirect monitoring of cell viability (Doxorubicin).

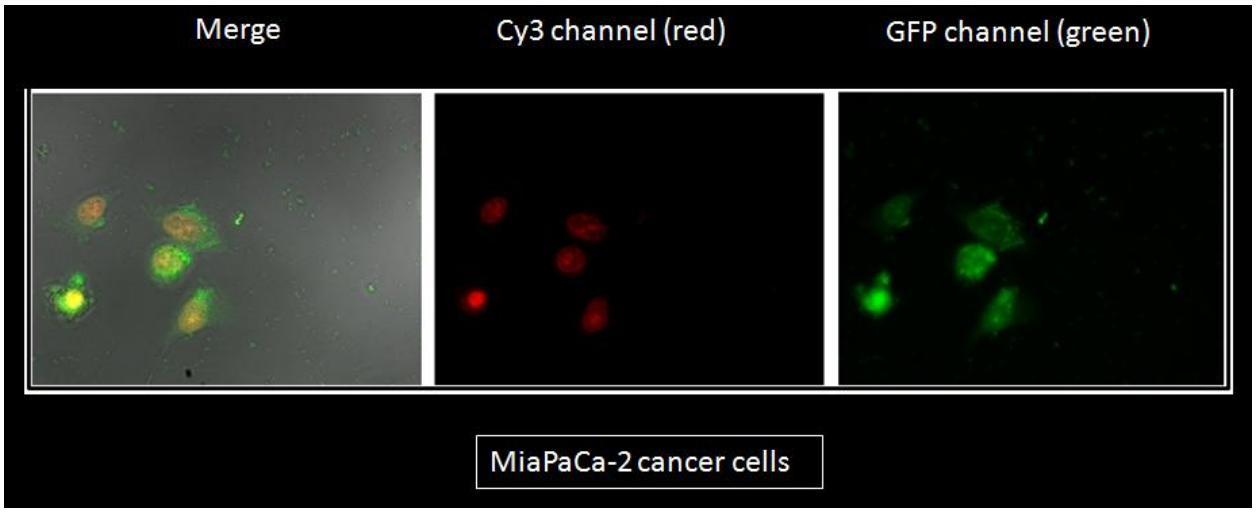

Figure 3.4. Confocal imaging of MiaPaCa-2 pancreatic cancer cells stained with LysoTracker Red and treated with fluorescently labeled TSUA-MSN. The spatial locations of TSUA-MSN labeled with fluorescein can be visualized in the green channel (far right), some of which colocalize with the lysosomes in the red fluorescence channel (middle), suggesting the successful lysosomal uptake of TSUA-MSN by MiaPaCa-2 cells.

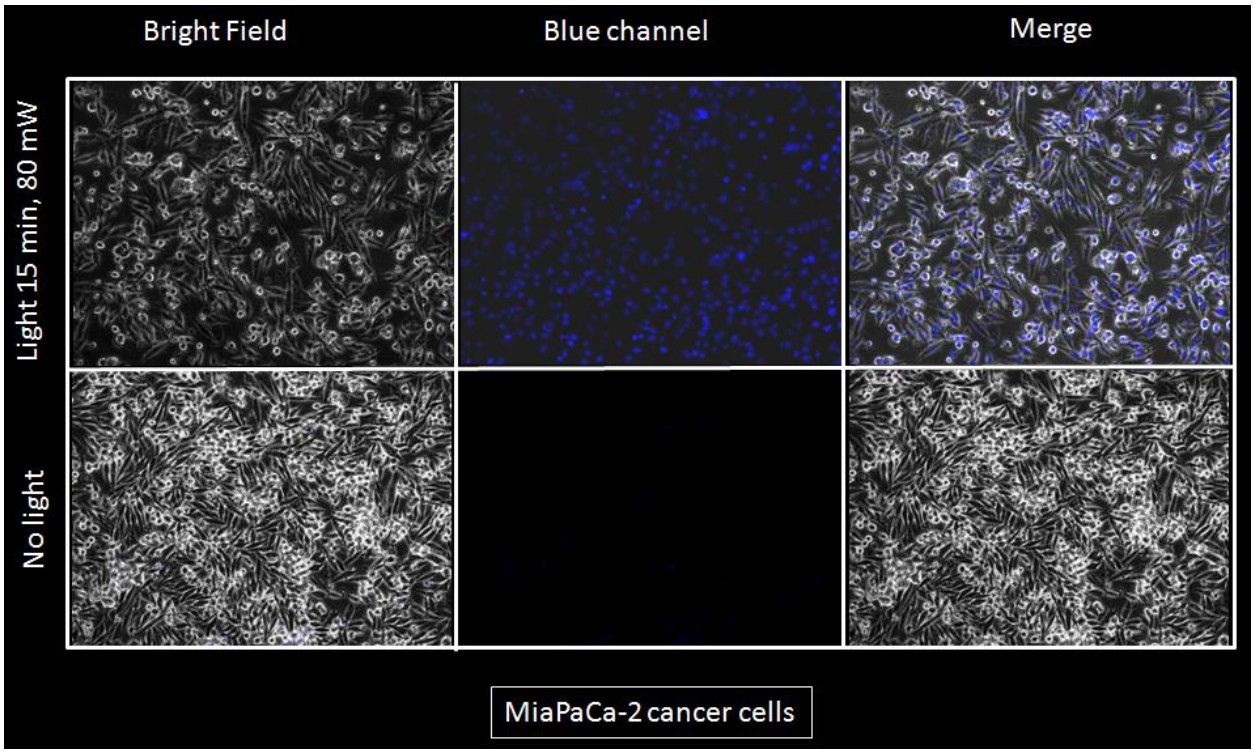

Figure 3.5. Confocal imaging of MiaPaCa-2 pancreatic cancer cells treated with TSUA-MSN and loaded with Hoechst 33342 nuclear stain. The upper frames show that light irradiation (403 nm, spot size = 1 cm^2) of the TSUA-MSN nanovalve after cellular uptake resulted in cargo release, as visualized by the blue fluorescence of the Hoechst stained nuclei (upper frames, middle image). In the cell sample treated with TSUA-MSN loaded with Hoechst stain not subjected to light irradiation, no nuclear staining was observed in the blue channel (lower frames, middle image). This indicates that the observed Hoechst staining is a result of light-activated cargo release.

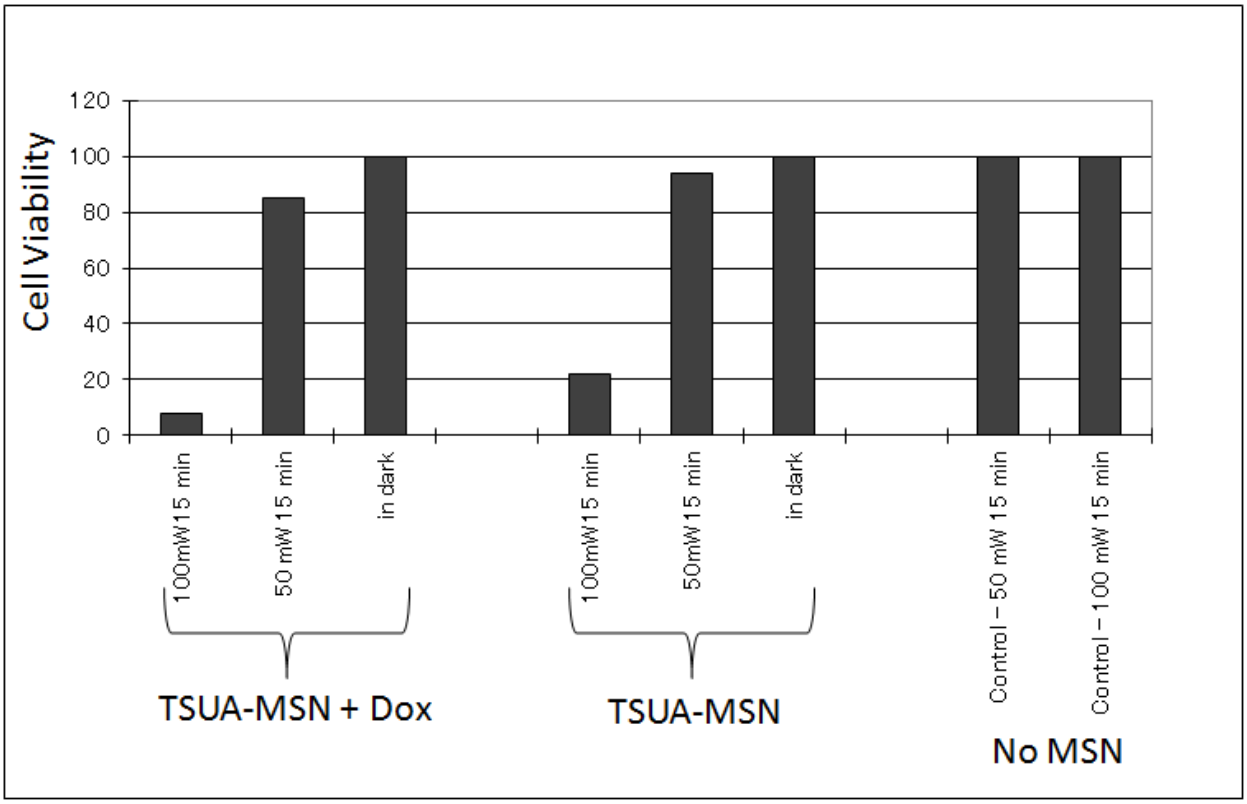

Figure 3.6. Cell viability assay performed on MiaPaCa-2 cancer cells treated with 20 μg/mL of TSUA-MSN loaded with or without Doxorubicin. For both the loaded and unloaded samples, no cell killing was observed in the dark. When irradiated by light (403 nm, spot size = 1 cm^2), the Dox loaded sample shows cell killing when exposed to both 50 and 100 mW of laser power. There is an almost 100% cell death observed at 100 mW laser exposure in the Dox loaded samples. Exposure at 50 and 100 mW in the absence of TSUA-MSN resulted in no cell death. Interestingly, cell killing was also observed in the sample treated with unloaded TSUA-MSN, presumably from ROS generation.[28]

3.6 References

(1) Hernandez, R.; Tseng, H.-R.; Wong, J. W.; Stoddart, J. F.; Zink, J. I. *J. Am. Chem. Soc.* **2004**, *126*, 3370–3371.

(2) Nguyen, T. D.; Tseng, H.- R.; Celestre, P. C.; Flood, A. H.; Liu, Y.; Stoddart, J. F.; Zink, J. I. *Proc. Natl. Acad. Sci. U.S.A.* **2005**, *102*, 10029–10034.

(3) Saha, S.; Leung, K. C.-F.; Nguyen, T. D.; Stoddart, J. F.; Zink, J. I. *Adv. Funct. Mater.* **2007**, *17*, 685–693.

(4) Nguyen, T. D.; Liu, Y.; Saha, S.; Leung, K. C.-F.; Stoddart, J. F.; Zink, J. I. *J. Am. Chem. Soc.* **2007**, *129*, 626–634.

(5) Yang, Q.; Wang, S.; Fan, P.; Wang, L.; Di, Y.; Lin, K.; Xiao, F.-S. *Chem. Mater.* **2005**, *17*, 5999–6003.

(6) Nguyen, T. D.; Leung, K. C.-F.; Liong, M.; Pentecost, C. D.; Stoddart, J. F.; Zink, J. I. *Org. Let.* **2006**, *8*, 3363–3366.

(7) Leung, K. C.-F.; Nguyen, T. D.; Stoddart, J. F.; Zink, J. I. *Chem. Mater.* **2006**, *18*, 5919–5928.

(8) Park, C.; Oh, K.; Lee, S. C.; Kim, C. *Angew. Chem., Int. Ed.* **2007**, *46*, 1455–1457.

(9) Angelos, S.; Yang, Y.-W.; Patel, K.; Stoddart, J. F.; Zink, J. I. *Angew. Chem., Int. Ed.* **2008**, *47*, 2222–2226.

(10) Patel, K.; Angelos, S.; Dichtel, W. R.; Coskun, A.; Yang, Y.-W.; Zink, J. I.; Stoddart, J. F. *J. Am. Chem. Soc.* **2008**, *130*, 2382–2383.

(11) Mal, N. K.; Fujiwara, M.; Tanaka, Y. *Nature* **2003**, *421*, 350–353.

(12) Nguyen, T. D.; Leung, K. C.-F.; Liong, M.; Liu, Y.; Stoddart, J. F.; Zink, J. I. *Adv. Funct. Mater.* **2007**, *17*, 2101–2110.

(13) Angelos, S.; Choi, E.; Vögtle, F.; De Cola, L.; Zink, J. I. *J. Phys. Chem. C* **2007**, *111*, 6589–6592.

(14) Aznar, E.; Casasús, R.; García-Acosta, B.; Marcos, M. D.; Martínez-Mánêz, R.; Sancenón, F.; Soto, J.; Amorós, P. *Adv. Mater.* **2007**, *19*, 2228–2231.

(15) Liu, N.; Yu, K.; Smarsly, B.; Dunphy, D. R.; Jiang, Y.-B.; Brinker, C. J. *J. Am. Chem. Soc.* **2002**, *124*, 14540–14541.

(16) Liu, N.; Chen, Z.; Dunphy, D. R.; Jiang, Y.-B.; Assink, R. A.; Brinker, C. J. *Angew. Chem., Int. Ed.* **2003**, *42*, 1731–1734.

(17) Liu, N.; Dunphy, D. R.; Atanassov, P.; Bunge, S. D.; Chen, Z.; Lo´pez, G. P.; Boyle, T. J.; Brinker, C. J. *Nano Lett.* **2004**, *4*, 551–554.

(18) J. Lu, M. Liong, J. I. Zink and F. Tamanoi, *Small*, **2007**, 3, 1341–1346.

(19) Coti, K. K.; Belowich, M. E.; Liong, M.; Ambrogio, M. W.; Lau, T. A.; Khatib, H. A.; Zink, J. I.;

(20) Li, Z.; Barnes, J. C.; Bosoy, A.; Stoddart, J. F.; Zink, J. I. *Chem. Soc. Rev.* **2012**, 41, 2590-2605.

(21) Zhao, Y.-L.; Li, Z.; Kabehie, S.; Botros, Y. Y.; Stoddart, J. F.; Zink, J. I. *J. Am. Chem. Soc.* **2010**, 132, 13016-13025.

(22) Meng, H.; Xue, M.; Xia, T.; Zhao, Y.-L.; Tamanoi, F.; Stoddart, J. F.; Zink, J. I.; Nel, A. E. *J. Am. Chem. Soc.* **2010**, 132, 12690-12697.

(23) Khashab, N. M.; Belowich, M. E.; Trabolsi, A.; Friedman, D. C.; Valente, C.; Lau, Y. A.; Khatib, H. A.; Zink, J. I.; Stoddart, J. F. *Chem. Comm.* **2009**, 36, 5371-5373.

(24) Angelos, S.; Khashab, N. M.; Yang, Y.-W.; Trabolsi, A.; Khatib, H. A.; Stoddart, J. F.; Zink, J. I. *J. Am. Chem. Soc.* **2009**, 131, 12912-12914.

(25) Tarn, D.; Xue, M.; Zink, J. I. *Inorg. Chem.* **2013**, 52, 2044-2049.

(26) Ferris, D. P.; Zhao, Y.-L.; Khashab, N. M.; Khatib, H. A.; Stoddart, J. F.; Zink, J. I. *J. Am. Chem. Soc.* **2009**, 131, 1686-1688.

(27) Shapiro, H. M. *Cytometry* **1981**, 2, 143-150.

(28) Podsaidły, R.; Sokołowska, J. *Color. Technol.* **2003**, 119, 341-344.

CHAPTER 4

pH-Responsive Dual Cargo Delivery from Mesoporous Silica Nanoparticles with a Metal-latched Nanogate

4.1 Abstract

A nanogate composed of two iminodiacetic acid (IDA) and a metal ion latch was designed, synthesized and assembled on mesoporous silica nanoparticles. This gating mechanism is capable of storing and releasing metal ions and molecules trapped in the pores. Pore openings derivatized with IDA can be latched shut by forming a bis-IDA chelate complex with a metal ion. This system was tested by loading with Hoechst 33342 as the probe cargo molecule, and latching with cobalt, nickel or calcium metal ions. No cargo release was observed in a neutral aqueous environment, but both cargos were delivered after acid stimulation and/or the addition of a competitively binding ligand.

4.2 Introduction

Nanoparticles of MCM-41 silica, a type of mesoporous nanomaterial, have found a variety of applications in many fields.[1-6] In the area of drug delivery, their large pore volume, easily accessible pores, well-established surface chemistry and high rate of endocytosis by mammalian cells makes them versatile nanocontainers.[4, 5, 7-10] Nanomachines are increasingly being employed on mesoporous silica nanoparticles (MSN) for stimuli-responsive delivery of cargo molecules from the pores. Numerous organo-functionalized silicas have been designed on MSN for the purpose of pore control. Researchers have exploited a creative variety of both covalent and non-covalent systems to achieve this goal, including supramolecular nanovalves, [11-17] snap-tops,[18] polymer networks,[19] metal nanocrystals,[20] biomolecules,[21] light-responsive nanogates,[22] magnetic field-responsive nanogates,[23] nanoimpellers,[24] cleavable chemical bonds,[25] and hydrophobicity.[26] These methods have demonstrated the stimulated release of a variety of ~1-2 nm sized cargo molecules, but are unable to hold back small metal ions in pores. Reversible chelation on nanoparticles has been used to bind and release metal ions, but did not trap and release molecules from pores.[27-29]

Many metal ions play important biological roles and are the active center of enzymes, proteins, vitamins, and coenzymes.[30,31]Calcium is heavily regulated in eukaryotic cells as a reflection of its important role in a number of physiological processes, notably in inducing apoptosis.[32,33] Normally regulated and stored in the endoplasmic reticulum and mitochondria inside cells, calcium stimulates an apoptotic cycle when present in the cell cytoplasm.[34,35] MSNs have been shown to be endocytosed by cells, resulting in colocalization in endosomes and finally endosomal escape through a “proton sponge effect” which results in payload delivery to the cell cytoplasm. Endosomal pH can be as low as 4.5 and more commonly in the range of pH 5-7. [17]

Delivery of traditional anti-cancer drugs such as camptothecin with MSN has also shown high efficacy and cell killing compared to the free drug.[17] A delivery system capable of delivering both therapeutic cargo molecules and bio-relevant metal ions would be more efficient than single cargo nanocarriers and could take advantage of synergistic interactions. In this chapter we demonstrate a method that utilizes coordination chemistry in order to achieve the objective of carrying and releasing both metal ions and biologically useful organic cargo molecules from MSN.

4.3 Results and Discussion

4.3.1 Design of the Gate

In the design of this system, a swinging gate with a latch was synthesized and assembled on MSN to control pore access. Two gates freely swinging on hinges can be locked in place with a latch. The latch serves a dual purpose of being a desired cargo type and latching the gates shut. When situated around the pore openings, these gates regulate entrance to the pore interiors (Figure 4.1b). Cargo molecules are free to diffuse in and out of the pores when the gates are unlatched, but when a metal ion is present, cargo is trapped as a result of latching the nanogate shut. Using this design strategy, iminodiaacetic acid (IDA), a chelating agent, is selected as the gate and a metal ion integrated as the latch.

Iminodiaacetic acid has a chelating property similar to that of one-half of an ethylenediaminetetraacetic acid (EDTA) molecule. When IDA is attached to silica with a flexible linker, two neighboring IDA molecules can bind strongly to a metal ion. The IDA binding constant with various metal centers exhibits a ~10^3 decrease upon changing the pH from neutral to mildly acidic as a result of protonation of the Lewis base chelating groups.[28,29] This

property is the basis for the mechanism of operation of the pH responsive nanogate. A flexible linker bonded to the amine moiety results in one point of attachment to the nanoparticle surface, creating a potentially tridentate ligand that is free to swing when unlatched.[44] The introduction of a metal ion results in a bis-IDA complex, joining two IDA molecules to the metal ion forming $M(IDA)_2$ tethered to the MSN at the end of each ligand. When the chelation occurs over a pore opening the system can trap and release molecules into and from the pores (Figure 4.1b). Since IDA can form stable complexes with many different transition metal ions,[36,37] this system can function with a variety of different metal latches. Co(II), Ni(II) and Ca^{2+} (that have 10^7, 10^8, and 10^2 order of magnitude formation constants, respectively) were chosen for this study.[37,38]

MSNs were synthesized using a surfactant-templated sol-gel process producing spherical nanoparticles ~100 nm in diameter. Acid removal of the templating agent resulted in hexagonally arranged mesopores about 2.2 nm in diameter (Figure 4.1a, 4.5). Because of the aqueous synthesis conditions, MSNs have a high surface silanol density and additional treatments to functionalize the particles are not required. The IDA swinging gates were attached to the silanols through a post-synthesis grafting method shown in Figure 4.2.[39]

Because of its existence as a zwitterion, IDA required conversion to an ester in order to allow for nucleophilic substitution to the halogenated alkoxysilane. This was accomplished by reacting IDA with oxalyl chloride in methanol, and nucleophilic substitution of 3-iodopropyltriethoxysilane. The triethoxysilane intermediate was attached to the particle surface through a condensation reaction with surface Si-OH (See Experimental Section). After grafting on the particle surface, the methyl ester was hydrolyzed to restore IDA (Figure 4.2a).

4.3.2 Characterization

Synthesized MSN quality was confirmed through XRD and TEM measurements. TEM was used to confirm the distribution of particle sizes between 80-120 nm. Image analysis software of nanoparticles viewed directly down the axis of the pore structure showed that the nanoparticles had pore diameters of 2.2 nm (Figure 4.5, Figure 4.1a). The hexagonal pore arrangement observed in Figure 4.1a is confirmed by higher order Bragg peaks shown in the powder XRD which can be indexed as the (100), (110) and (200) planes (Figure 4.6) with a lattice spacing of 4 nm. Complete removal of the templating agent was confirmed with FTIR spectroscopy with the disappearance of the C-H stretching peaks at 3000 cm^{-1} after acid extraction (Figure 4.7). The synthesis of compounds **1** and **2** were verified with ^{1}H NMR (see Experimental Section). Successful attachment of the nanogate was confirmed through CP-MAS solid state ^{29}Si NMR with the appearance of two signals at -54 and -72 ppm as di- and tri-functionalized Si-C (Figure 4.8b), respectively. Additionally, a IDA carbonyl peak was observed in solid state ^{13}C NMR at 149 ppm, a corresponding α-carbon at 128 ppm, and the aliphatic carbons appearing between 10-50 ppm, indicating successful attachment of the nanogate thread (Figure 4.8a).

4.3.3 Loading and Release

After confirmation of successful nanogate grafting, the machine was assembled through a process of loading an organic molecule, latching the gates with a metal ion, and washing away any excess cargo. Hoechst 33342, a dye commonly used as a nuclear stain in cells was chosen as the probe for its ease of detection and its similar size characteristics to those of therapeutic drugs. By monitoring the fluorescence intensity of Hoechst, a real-time release profile can be generated. From previous studies of grafted molecules, we estimate an average of four gates around each

pore opening, corresponding to two assembled nanogates per pore (Figure 4.1b).[15] Based on molecular size estimates, when closed, this number of nanogates is more than enough to prevent leakage of cargo molecules between 1-2 nm. Loading of Hoechst dye was accomplished by suspending IDA modified nanoparticles in a concentrated solution of the dye and allowing sufficient time for the dye molecules to diffuse inside the pores.

4.3.4 Cobalt Latch

The Hoechst loaded nanoparticles were latched shut after introducing a metal ion. Cobalt was chosen as the first metal latch because of its stability, solubility, and large binding constant with IDA. Introducing the Co^{2+} ion latches the nanogates together by bringing two IDA units together (Figure 4.2b). In order to remove any surface adsorbed Hoechst and unbound cobalt, the pale yellow particles were washed with aliquots of fresh $_{dd}H_2O$ until the rinses no longer exhibited any fluorescence.

To assess the functioning of the nanogates, release of Hoechst dye was monitored using a time-resolved fluorescence spectroscopy method. The fully assembled and latched nanoparticles were placed in a corner of a glass cuvette and an excitation beam (377 nm) was used to excite any dye released into the supernatant (Figure 4.11). The corresponding emission spectrum was collected to generate a time-resolved release profile.

4.3.5 Acid Release

After collecting baseline fluorescence, the machine was activated by slightly acidifying the solution. Trace 1 in Figure 4.3a shows that at neutral pH no Hoechst fluorescence is detected indicating no observable cargo leakage of Hoechst molecules at neutral pH. After adjusting the solution to a pH of 5, a large increase in solution fluorescence is observed, indicating a release of Hoechst molecules from the pores into solution stimulated by the acidification. In order to

differentiate between surface-adsorbed dye from dye stored in the pores and to assess hydrogen bonding strengths between IDA dimers, a control experiment was performed where IDA modified particles were loaded with Hoechst but left unlatched by omitting the cobalt attachment step. This sample was subjected to a similar washing procedure and "released" by adjusting the solution pH to 5. Trace 3 in Figure 4.3a shows no Hoechst release after acidification, indicating that the loaded Hoechst cargo was removed during the washing steps. This also indicates that the amount of positively charged Hoechst adsorbed on the surface silanols (which ionize into $Si\text{-}O^-$ in neutral pH)[40] is insignificant when compared to the amount capable of being stored and delivered through pore control (Figure 4.3b). Additionally, hydrogen bonding between two IDA dimers does not result in unintentionally latching the nanogates and holding back cargo.

After completion of each time-resolved fluorescence spectra, the amount of cobalt removed from the nanogates was analyzed through ICP-OES analysis. For the sample loaded with Hoechst and latched with cobalt, the addition of acid resulted in cobalt unbinding (Figure 4.3b1). Because of the strength of the electrostatic interaction between doubly cationic cobalt and surface $Si\text{-}O^-$ groups, Co^{2+} was difficult to completely remove from the particle surface with washings. As a result, after subjecting Hoechst loaded cobalt latched nanoparticles to a 24 hour soaking period, a small quantity of cobalt was still removable from the particle surface (Figure 4.3b2). It is important to note that this unbinding of cobalt is not coupled with Hoechst cargo release. This result indicates that at least two differently bound forms of cobalt are removed from MSN: surface adsorbed cobalt as a result of electrostatic interactions with silica, and chelated cobalt bound in the IDA nanogates.

After complete release, the total weight percent of dye was calculated through UV-Vis absorption measurements of the solution supernatant. The observed 2% weight of Hoechst is a

typical delivery capacity of MSN loaded with Hoechst.[41] Additionally, a 0.2% weight release of cobalt was observed. In terms of molar concentration, this amount is on the order of Hoechst released; 5 mg of gated particles can release ~0.2 μmols of Hoechst and cobalt, demonstrating that the system is capable of delivering comparable molar quantities of both cargo types (Figure 4.3b1). The large amount of cobalt released can be explained through examining the pore structure of MCM-41. Only nanogates present across the pore openings function in controlling Hoechst delivery. However, some derivatization of the particles with IDA also occurs on the outer surface, resulting in sites for metal ion chelation not used to control pore access but acting as cobalt storage (Figure 4.3c). Due to the large excess of cobalt used in latching the nanogate, these non-gating IDA moieties can also chelate cobalt, resulting in the large amount of cobalt released after acidification.

4.3.6 Competitive Binding Release

Since the nanogate trapping is dependent on the coordination of the metal center, removal of the metal center by a strong chelating agent dissolved in solution should also result in cargo release. To examine this, the cobalt latched nanogate was exposed to a molecule capable of competitively binding cobalt from IDA. Figure 4.3a trace 2 demonstrates that the addition of 2,2'-bipyridine (bipy) to the system results in the release of Hoechst cargo. Therefore, a second release method based on competitive binding is also possible. If a ligand that has a large binding constant with the metal ion is added to the system, that ligand competes with the IDA, binds with the metal, and thus opens the system. This result demonstrates that the removal of the metal center by a competing ligand unlatches the gate resulting in cargo delivery.

4.3.7 Nickel Latch

Since the amine and carboxylic acid groups on IDA can form strong coordinational bonds with a variety of transition metals, Ni^{2+} was also tested for a viable latch. Studies were performed using the same procedures as previously described. After loading with Hoechst cargo and latching the nanogate by introducing Ni^{2+}, a baseline fluorescence was collected at neutral pH to verify the stability of the assembled machine. When the solution pH is adjusted to a pH of 5, a release of Hoechst into the solution was observed (Figure 4.4a). This result indicates that the IDA nanogate is tightly shut when latched with nickel and can also be used to deliver nickel ions after acidification. In an experiment similar to that of the cobalt latched nanogate, the nickel latched machine was also tested for release with competitive binding. A baseline fluorescence was also collected for a comparable time and released via the addition of bipy. Hoechst release is only observed after bipy addition, indicating a similar mechanism of trapping and release to that of the cobalt latched nanogates (Figure 4.9).

4.3.8 Calcium Latch

Calcium, a metal ion with important biological significance was also tested with this design. Because of its role as a regulator for cell apoptosis, a controlled delivery of calcium can potentially have therapeutic value. Therefore, the IDA nanogate system was tested for functionality with calcium ions. In a similar fashion as described above, Hoechst loaded IDA nanoparticles were latched by introducing Ca^{2+}. A baseline was also collected for a comparable time to that for the transition metals and were released through acidification. No Hoechst cargo was observed to release until the pH of the solution was adjusted to a pH of 6, indicating the compatibility of calcium ion as a latch for this system (Figure 4.4b). Due to the lower binding affinity between calcium and IDA, Hoechst release was observed to begin at a higher pH value

than that for the nickel and cobalt latched nanomachines. Since the stability of the formed metal inorganic complex is metal dependent, each nanogate built on a different metal center may be activated at different pH, depending on the metal IDA binding strengths. Using this design, a metal center can be chosen that responds only to strongly acidic conditions or if desired, a metal nanogate that responds to a more subtle pH change.

4.4 Summary

In summary, a new type of nanogate supported on MSN was successfully designed and synthesized. The fully assembled system is capable of simultaneously delivering both large and small molecules. In neutral conditions, the nanogate remains closed and cargo is stored, but the addition of acid opens the nanogate, releasing both metal ions and the large cargo molecules. Controlled cargo release was also demonstrated by activation through competitive binding. This system can potentially be expanded as a delivery system for a broad combination of cargo molecules and metal ions for biological application. By changing both the metal ion and/or choice of nanogate, the pH responsiveness can be tuned to allow for biological pH activation. Currently, this system is being optimized using different transition metal ions with the goal of developing a synergistic drug delivery system.

4.5 Experimental

4.5.1 General Comments

Chemicals used in this study were purchased from major chemical suppliers such as Sigma-Aldrich and Fisher Scientific and used without further purification. Release studies were obtained with an in-house time-resolved fluorescence spectroscopy setup (Figure 4.11). A Coherent 377 nm CUBE laser was used to excite Hoechst dye, and the subsequent emission spectra monitored using a Princeton Instruments Roper CCD detector cooled to liquid nitrogen temperatures. ICP-OES measurements were made using a Thermo Jarrell Ash IRIS 1000 in a 5% HNO_3 matrix. XRD measurements were made using a Panalytical X'Pert Pro powder diffractometer. ^1H NMR was performed on a Bruker ARX400 spectrometer in $CDCl_3$ solution. Chemical shift is listed in ppm. The solvent signal was used as an internal standard. Solid state NMR was performed on a Bruker DSX300 spectrometer. TEM images were acquired on a JEM1200-EX microscope. SEM images were taken on a JSM-6701F microscope after coating with gold (5 nm) through plasma sputtering.

4.5.2 Synthesis of MCM-41 Nanoparticles

In a 250 mL round bottom flask equipped with a magnetic stir bar, cetyltrimethylammonium bromide (CTAB, 0.25 g, 0.7 mmol) was added and dissolved in deionized water (120 mL) with heat. The temperature was stabilized at 80 ^oC for 1 hour, and a NaOH solution (2 M, 870 µL, 1.7 mmol) was added to the mixture at a rate to maintain 80 ^oC. Tetraethylorthosilicate (TEOS, 1.2 mL, 5.4 mmol) was then added dropwise over 10 minutes under vigorous stirring (800 RPM) and reacted for 2 hours at 80 ^oC. After the allotted reaction time, the milky solution was allowed to cool to room temperature under stirring, and collected with centrifugation (7830 RPM, 15 min). The nanoparticles were washed with methanol until the

washings showed a pH of 7. DLS readings of synthesized MSN in water indicate a low PDI (224 nm, PDI 0.01) on a ZetaPals instrument. MSN particle quality was confirmed through TEM / XRD measurements (Figure 4.5, 4.6).

4.5.3 Extraction of Templating Agent

In a 250 mL round bottom flask, synthesized MSN (120 mg) were suspended in methanol (75 mL) with vigorous stirring and water bath sonication. Under sonication, concentrated HCl (12 M, 4.2 mL) was added to the dropwise suspension where the solution became clearer, and refluxed for 8 hours under inert atmosphere. The particles were recollected through centrifugation (7830 RPM, 15 min) and washed with portions of methanol until washings showed a neutral pH. Complete extraction of CTAB from the pores was confirmed through IR spectroscopy (Figure 4.7). Surfactant extracted particles gave a more monodisperse DLS reading in water (180 nm, PDI 0.005).

4.5.4 Synthesis of Dimethyl Iminodiacetate

In a 500 mL round bottom flask equipped with a reflux condenser and a magnetic stir bar, iminodiacetic acid (5 g, 38 mmol) was suspended in methanol (200 mL). The solution was cooled to 0^{o} C while oxalyl chloride (7 mL, 82 mmol) was added to the reaction mixture in dropwise fashion. After complete addition of the oxalyl chloride, the solution was warmed to room temperature and refluxed overnight. The solvent was evaporated off giving a white powder (6 g). The powder was dissolved in water, neutralized with sodium carbonate and extracted with ethyl acetate (3 x 35 mL). The combined organic layers was washed with brine (60 mL), and dried over anhydrous sodium sulfate, filtered, and concentrated under reduced atmosphere to give quantitative yields of a slightly yellow oil. ^{1}H NMR (chloroform-d): δ 2.01 (s, 1H), δ 3.36 (s, 4H), δ 3.61 (s, 6H).

4.5.5 Synthesis of (Dimethyl Iminodiacetate)propyltriethoxysilane

In a 50 mL three-necked round bottom flask equipped with a reflux condenser, gas inlet, and magnetic stir bar, dimethyl iminodiacetate (1 mL, 6 mmol), and 3-iodopropyltriethoxysilane (1 mL, 5 mmol) were dissolved in anhydrous toluene (5 mL). Catalytic amount of N,N-diisopropylethylamine was added and the mixture was allowed to react under dry nitrogen atmosphere overnight at reflux. The mixture was then cooled to room temperature, washed with 3 portions of water, brine and dried over anhydrous sodium sulfate. The organic layer was then concentrated under reduced pressure and purified with column chromatography oven-dried silica gel (CH_3Cl_3 : hexanes = 2 : 1) to yield quantitative amounts of (dimethyl iminodiacetate)propyltriethoxysilane. ^{1}H NMR (chloroform-d): δ 0.73 (t, 2H), δ 1.15 (t, 9H), δ 1.89 (m, 2H), δ 3.18 (t, 2H), δ 3.44 (s, 4H), δ 3.54 (q, 6H), δ 3.66 (s, 6H).

4.5.6 Synthesis of Dimethyl Iminodiacetate Modified Nanoparticles

In a 50 mL round bottom flask, MSN (50 mg) washed with toluene (2 x 10 mL) was suspended in anhydrous toluene dried over calcium hydride (10 mL). (Dimethyl iminodiacetate)propyltriethoxysilane (30 μL, 0.08 mmol) dissolved in toluene (1 mL) was added to the MSN suspension heated overnight at reflux temperatures. The functionalized particles were collected through centrifugation (7830 RPM, 10 min) and washed with toluene (2 x 10 mL) and methanol (2 x 10 mL).

4.5.7 Synthesis of Iminodiacetic Acid Modified Nanoparticles (IDA-MSN)

A 50 mL round bottom flask was charged with a suspension of dimethyl iminodiacetate modified silica nanoparticles (30 mg) in doubly distilled water (25 mL). Concentrated HCl (1.5 mL) was slowly added to the reaction mixture under sonication and refluxed for six hours. The particles were recollected through centrifugation (7830 RPM, 10 min) and washed with methanol

until the washings were of neutral pH. Successful functionalization of the silica surface was verified through solid state NMR (Figure 4.8a, 4.8b).

4.5.8 Loading of Hoechst 33342

IDA-MSN (10 mg) was washed twice with methanol and twice with doubly distilled water. After the solvent exchange, the particles were centrifuged and resuspended in a fresh solution of Hoechst 33342 in water (1 mM, 1 mL) and stirred overnight. The Hoechst loaded particles were collected through centrifugation (15,000 RPM, 3 min) and dried under vacuum.

4.5.9 Closing of the Nanogate and Loading of the Smaller Cargo

Hoechst loaded IDA-MSN (10 mg) was suspended in doubly distilled water (100 μL). For cobalt closed nanogates, cobalt(II) chloride (20 mg, 0.15 mmol) was added to the mixture and stirred for 6 hours. For nickel closed nanogates, nickel(II) chloride (20 mg, 0.15 mmol) was added instead. For calcium latched nanoparticles, calcium chloride (50 mg, 0.4 mmol) was added in a buffered solution (Tris buffered, pH 8) and stirred overnight. The assembled machine was collected through centrifugation (15,000 RPM, 3 min), washed with doubly distilled water until the washings no longer exhibited fluorescence under blacklight, and dried under vacuum.

4.5.10 Assessment of the Cargo Release

Hoechst loaded, metal ion capped IDA-MSN (5 mg) were confined to a corner of a rectangular glass cuvette. To this, doubly distilled water (4 mL) was added to the particles at a rate to limit particles from suspending in solution. A 377 nm excitation diode laser (14 mW) was directed through the solution supernatant. The emission of excited Hoechst dye present in the solution supernatant was monitored in real time by focusing the emitted light through a collecting lens, a 400 nm cutoff filter and a monochromator (300 nm window, centered on 500

nm) before integrating on a CCD detector (Figure 4.11). A baseline was collected over 2 hours of allowing suspended particles to settle before stimulating cargo release.

4.5.11 pH Activation

For pH released samples, after achieving a stable baseline with the setup as described above, a known quantity of dilute HCl freshly calibrated was added to adjust the solution pH to 5. A plot of fluorescence intensity with respect to time was generated through integrating fluorescence counts from 500-550 nm. After complete release, the supernatant was collected through centrifugation (7830 RPM, 25 min) and analyzed through UV-Vis to determine weight percent release of Hoechst dye. The amount of cobalt released was done through stabilizing dissolved metals by adding 70% HNO_3 (307 μL) to the release supernatant and analysis with ICP-OES. Intensity of the analyzed samples were standardized using standard solutions made by diluting a stock solution (1000 ppm, Fisher Scientific) of cobalt or nickel or calcium. Each sample was run 3x to generate statistical data and error.

4.5.12 Competitive Binding Activation

For the nickel latched nanogate, after achieving a stable baseline plot with the above setup, solid 2,2'-bipyridine (15 mg) was added to the solution to saturate the solution. Competitive binding release studies with the cobalt latched nanogate were performed by adding 100 μL of a saturated solution of bipy in water to the 4 mL sample.

4.6 Figures

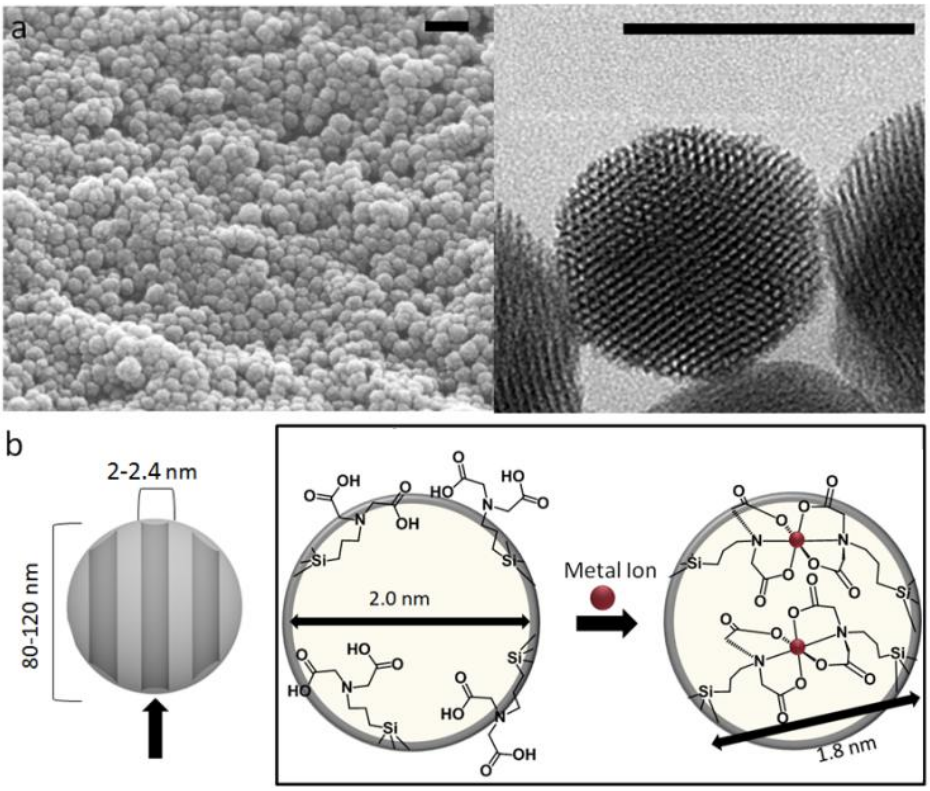

Figure 4.1. (a) SEM (left) and TEM (right) images of typical batches of MSN. The scale bar for SEM is 200 nm and that for TEM is 100 nm. The TEM image shows the hexagonally arranged pore channels. (b) Projection down the pore channels of MSN grafted with IDA. In the open state, the single tethered IDA is freely swinging and allows access to the pore channels, but the addition of a metal ion creates an inorganic complex tethered at two ends over the pore opening.

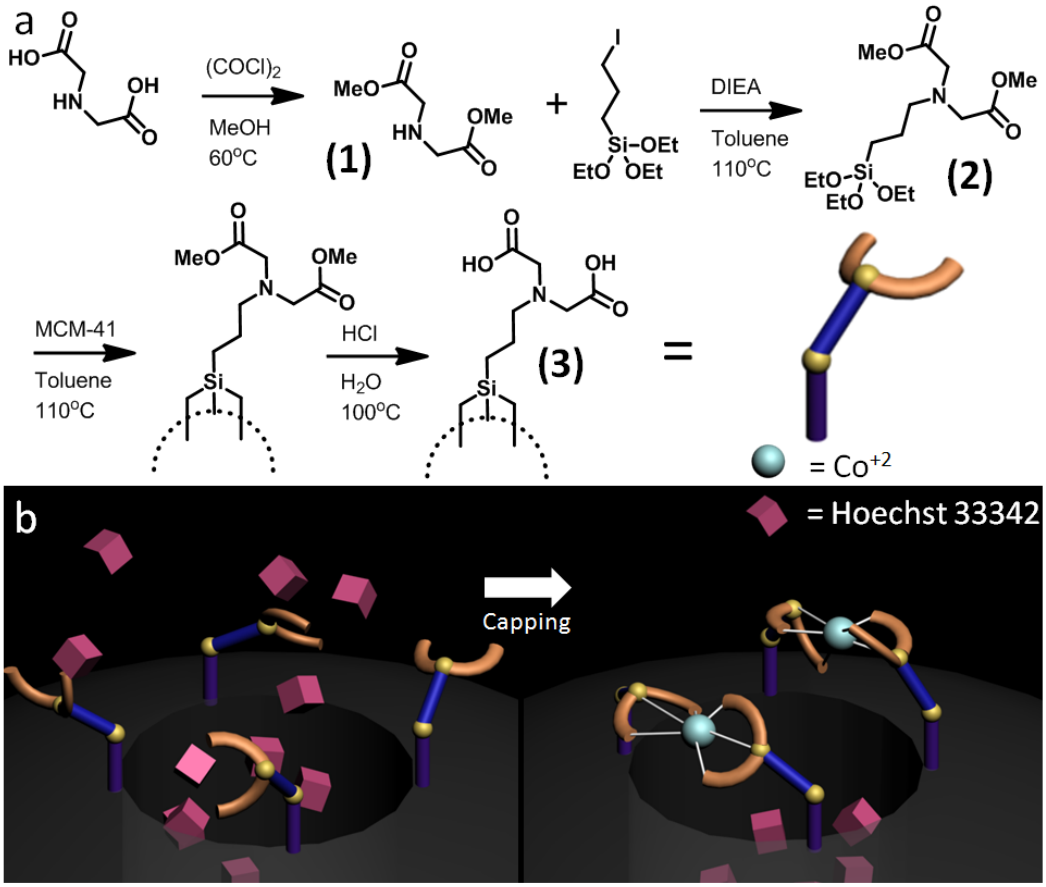

Figure 4.2. (a) Reaction scheme showing the synthesis and attachment of IDA to the nanoparticle surface. (b) Illustration of the machine assembly process. IDA-modified MCM-41 nanoparticles were loaded with Hoechst 33342, and the nanogate latched through the introduction of $CoCl_2$. The assembled nanogate was washed to remove surface-adsorbed dye and unbound cobalt.

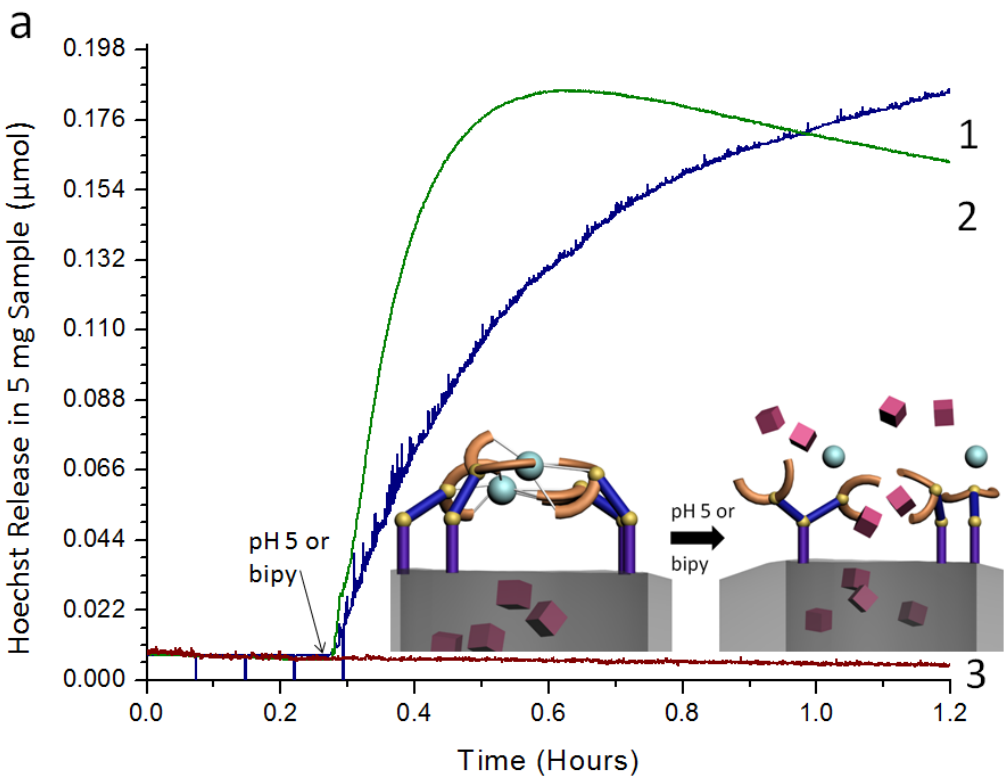

Figure 4.3. (a) Time-resolved fluorescence spectra showing the release of Hoechst dye from the gated pores. (Trace 1) Cargo is observed to release from the pores upon changing the solution pH to 5. (Trace 2) Release is also observed when 2,2'-bipyridine is added to the solution, since the competing chelator is capable of removing the metal latch from the nanogate. (Trace 3) No release of Hoechst is observed from Hoechst loaded IDA modified particles when no metal ion is introduced and the nanogate is left unlatched.

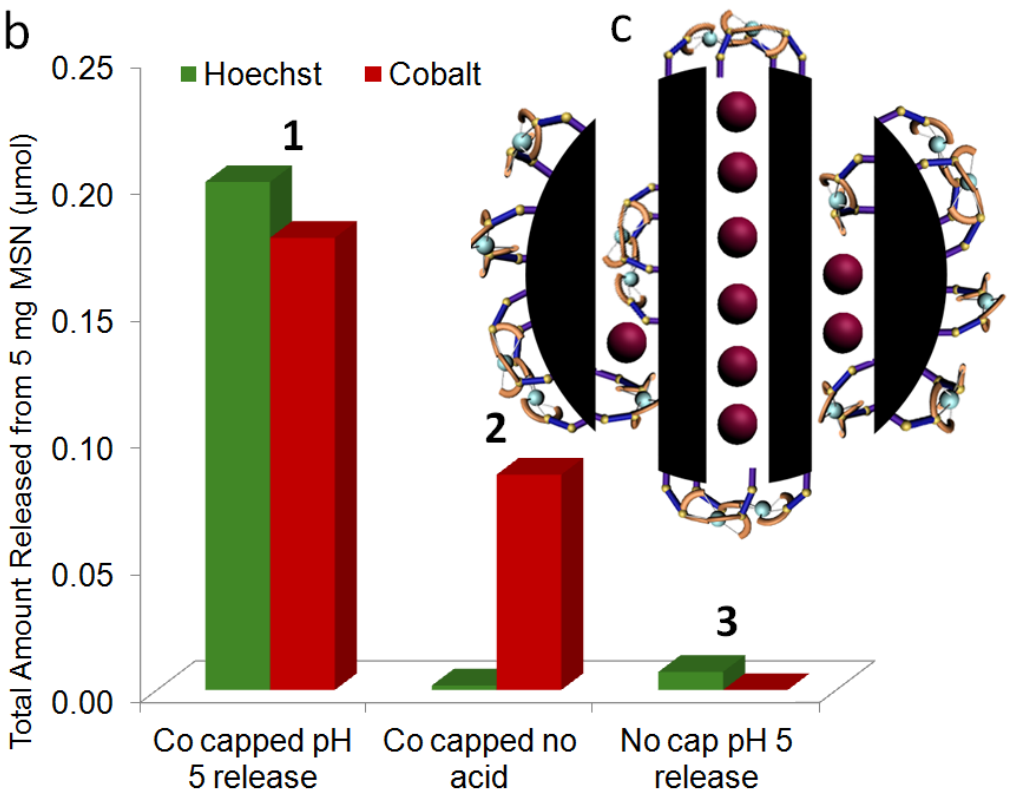

Figure 4.3. (b) 1. The total amount of Hoechst and cobalt (in µmols) released from 5 mg of nanomachine. 0.2 µmols of Hoechst released corresponds to a 2% weight release and 1.8 µmols of cobalt released corresponds to a 0.2% weight release. 2. Hoechst loaded, cobalt latched nanoparticles are subjected to a 24 hour soaking period in which a 1% weight release of cobalt is detected, but no Hoechst release. 3. Hoechst loaded IDA modified MSN are "released" by adjusting the solution pH to 5, resulting in a trivial amount of Hoechst released (c) Cobalt ions are released not only from the latched nanogates but also from ligands attached elsewhere on the particle.

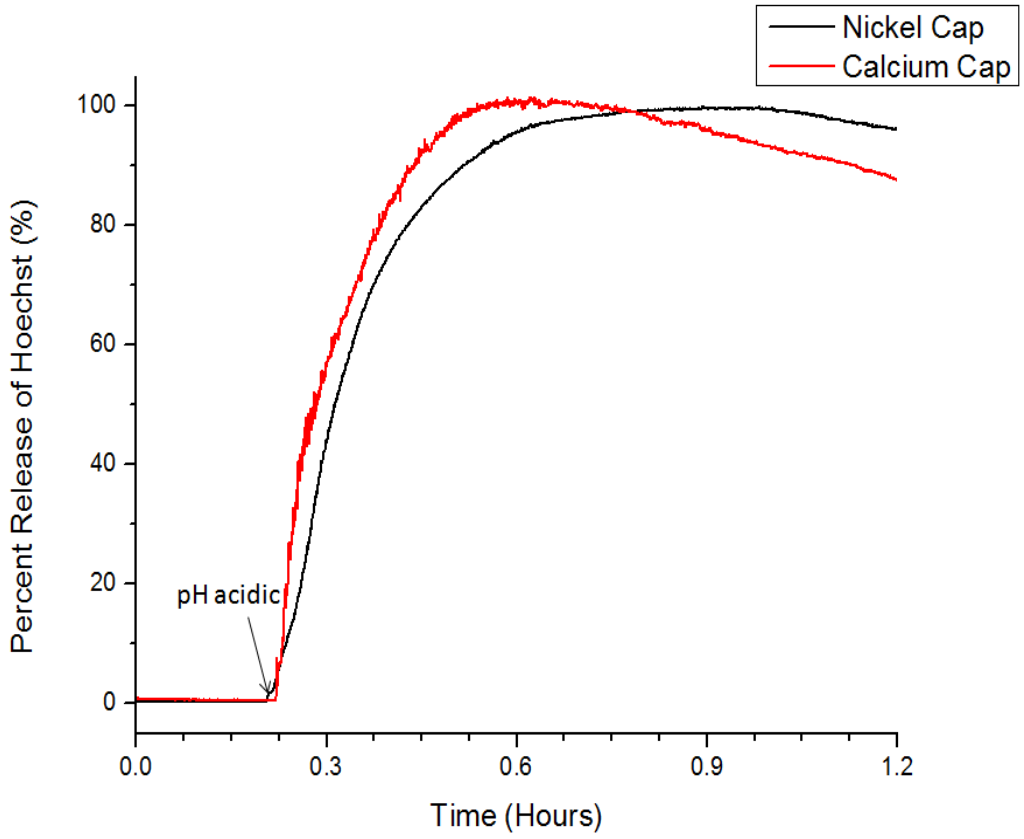

Figure 4.4. Time-resolved fluorescence spectra demonstrating the release of Hoechst cargo from nanogates assembled from nickel(II) (black trace) and calcium latches (red trace). No cargo release is observed from the nickel latched nanogates until the solution pH is adjusted to pH 5. Cargo release is observed from the calcium latched nanogates after adjusting the solution to a pH of 6, as a result of the lower binding constants between IDA and calcium. Release via competitive chelation is also demonstrated for the nickel latched nanogate (Figure 4.9).

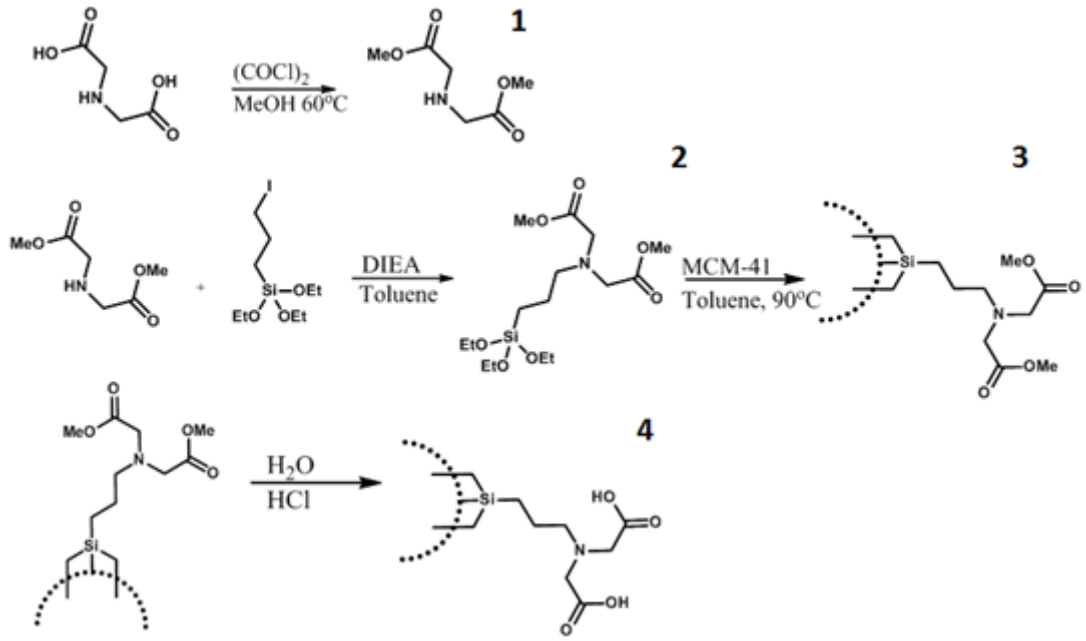

Scheme 4.1. Synthesis and attachment of nanogate machine. To make the IDA nitrogen more nucleophilic for halide displacement, IDA was first converted to a methyl ester. Halide substitution of 3-iodopropyltrimethoxysilane and silanol exchange with MSN resulted in successful grafting of IDA-OMe. The carboxylic acids were finally regenerated by acid hydrolysis after grafting onto MSN.

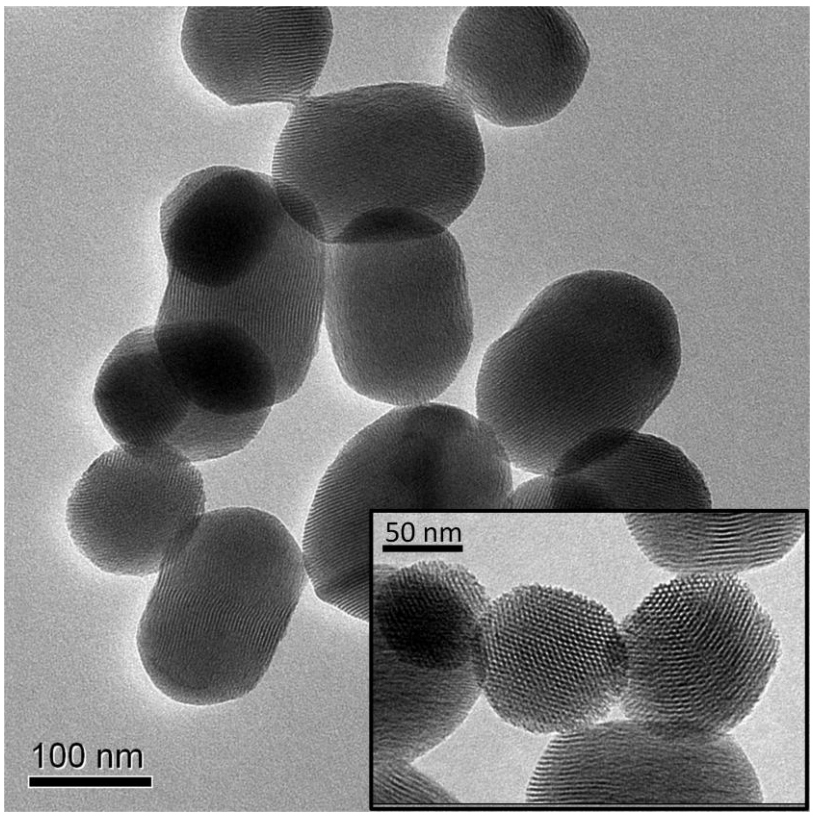

Figure 4.5. TEM image of a typical batch of synthesized and acid extracted MCM-41 nanoparticles. The average particle size is between 80-120 nm of highly monodisperse MSN. The hexagonally arranged pores are clearly visible when viewed directly down the pore axis.

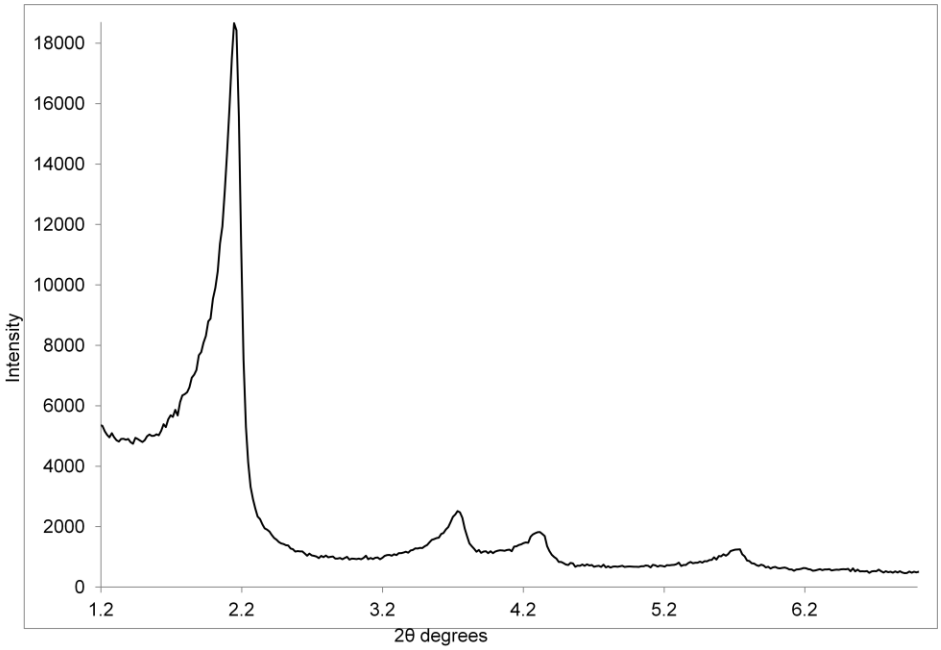

Figure 4.6. Powder XRD diffraction of synthesized MCM-41 nanoparticles.

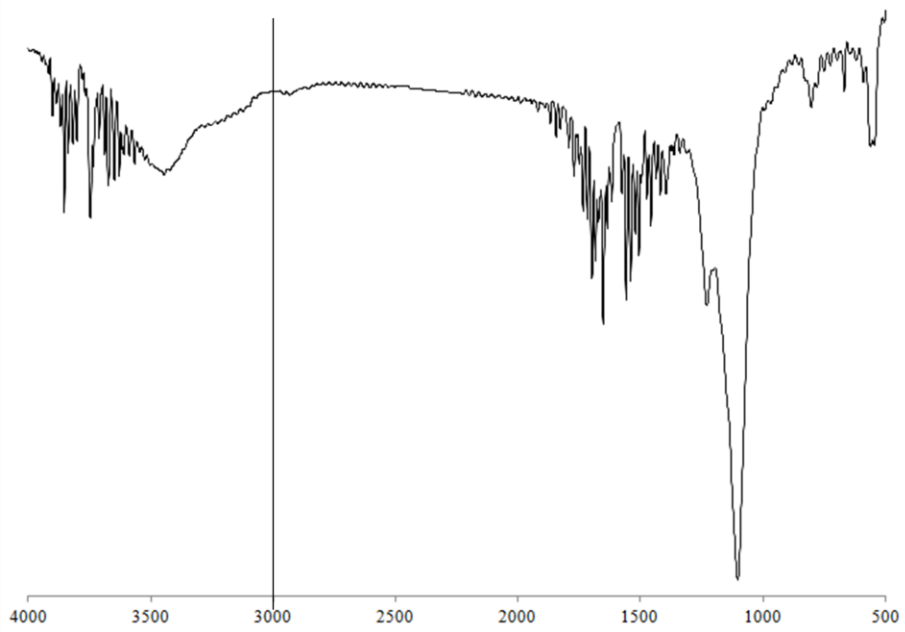

Figure 4.7. FTIR of surfactant extracted synthesized MSN. The disappearance of the C-H stretching peak (3000 cm^{-1}) indicates that the acid extraction procedures is successful in removing all of the templating agent.

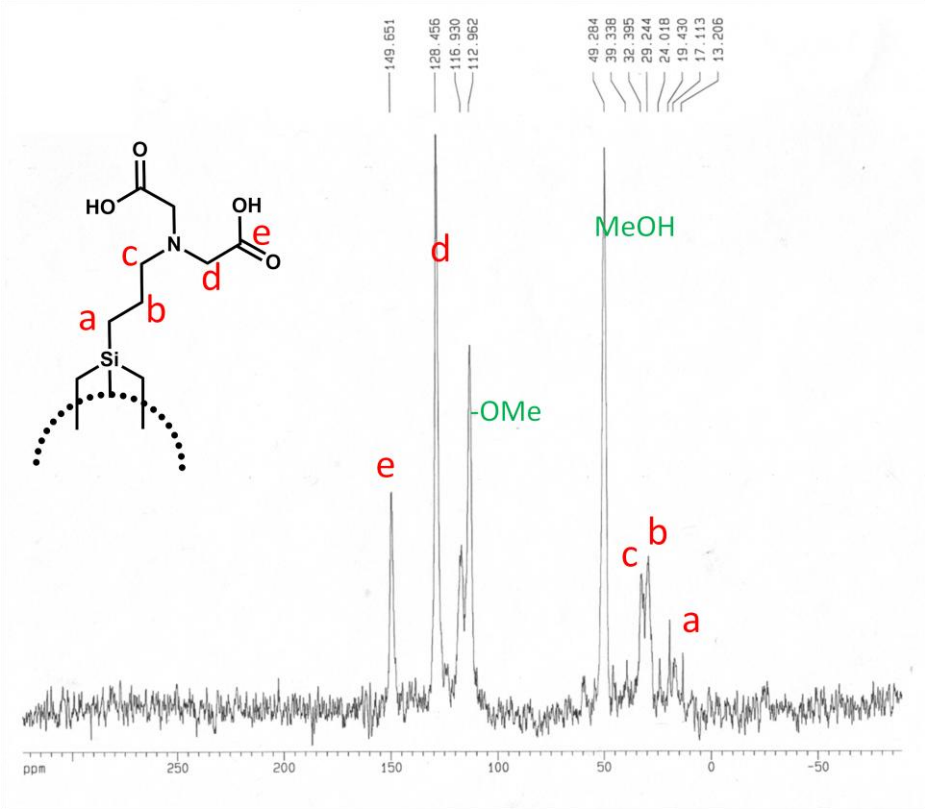

Figure 4.8a. SS ^{13}C NMR spectrum of iminodiacetic acid modified MSN. Peaks corresponding to IDA are observed in the region >50 ppm. Bare nanoparticles with –OMe terminated silanes do not show peaks in this region.

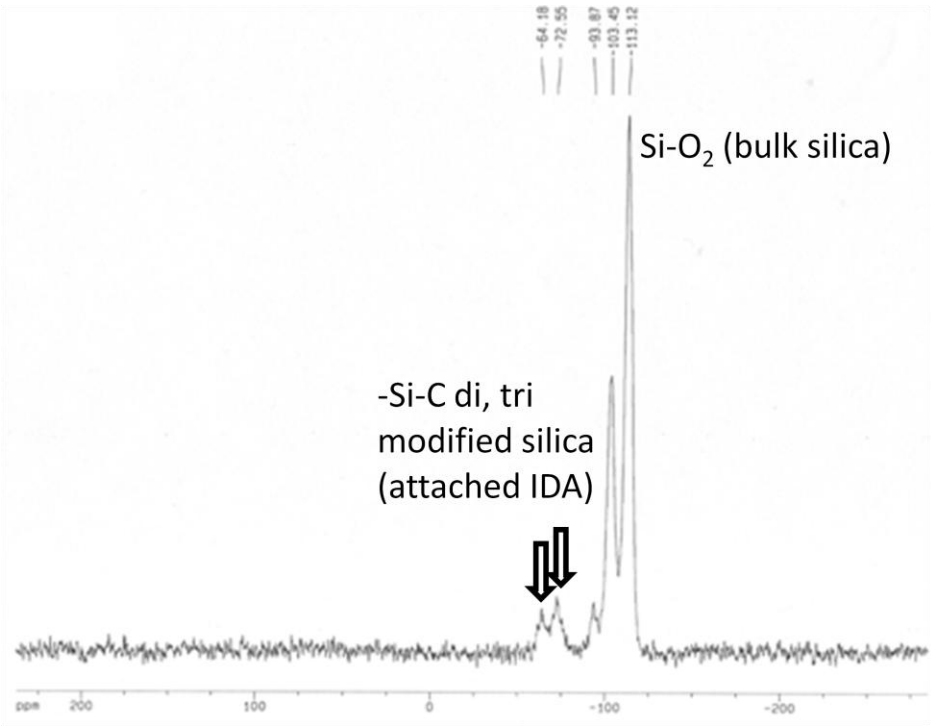

Figure 4.8b. SS ^{29}Si NMR spectrum of iminodiacetic acid modified MSN.

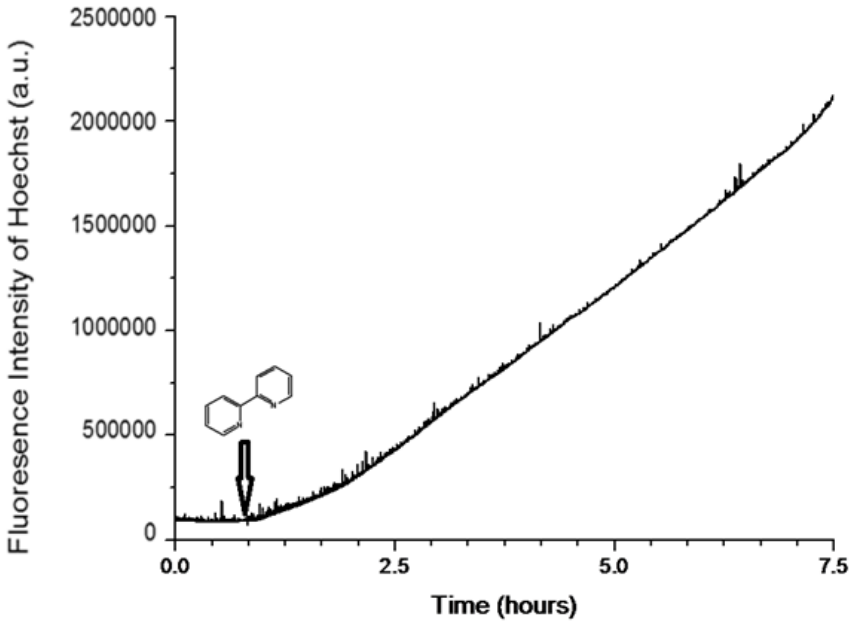

Figure 4.9. Time resolved fluorescent spectrum release profile of Hoechst 33342 cargo from a nickel latched nanogate machine. Solid 2,2'-bipyridine was added as a competitively binding ligand to remove nickel from the iminodiacetic acid nanogates and initiate cargo release. The slow rate of release was due to the low solubility of 2,2'-bipyridine in water.

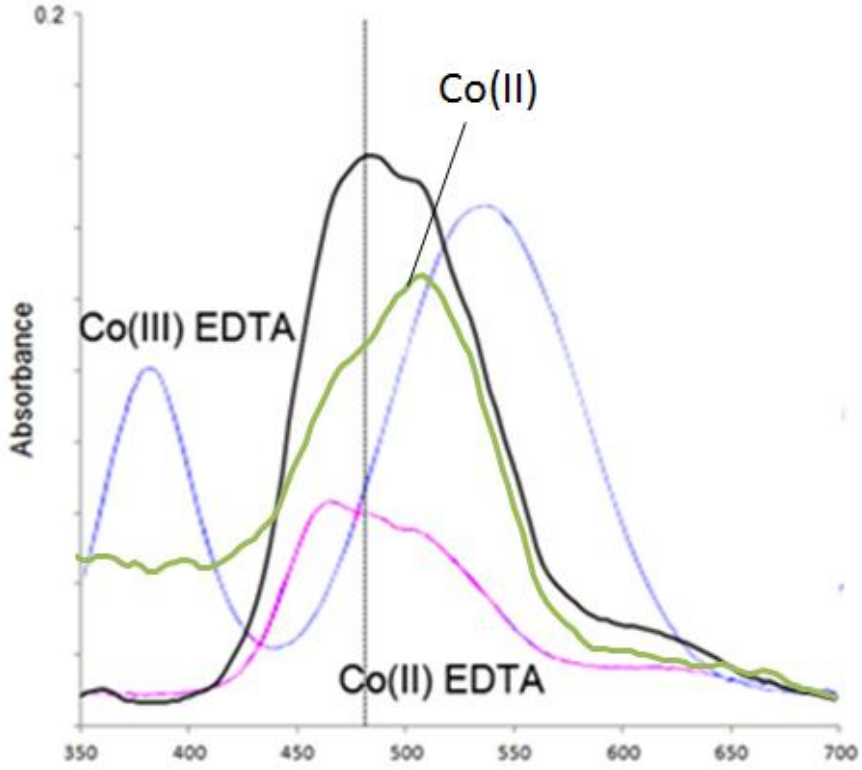

Figure 4.10. UV-Vis spectra of solution Co/EDTA complexes after simulated loading conditions. The oxidation state of cobalt was determined through spectroscopic methods after mimicking the loading and capping conditions of the nanoparticles. In green: UV-Vis spectra of a Co(II) solution in water. In pink: UV-Vis spectra of 5 mM Co(II)EDTA. In blue: Co(III)EDTA complex (Xue, Y.; Traina, S. J. *Environ. Sci. Technol.* 1996, 30, 1975-1981). In black: UV-VIS spectra of 10 mM cobalt/EDTA complex after undergoing similar conditions as used in the loading/capping procedures. After this process, the cobalt is bound to EDTA as shown in the increase in absorbance at 470 nm, and most of the cobalt/EDTA is still in the +2 oxidation state as indicated by the absence of a peak at 370 nm.

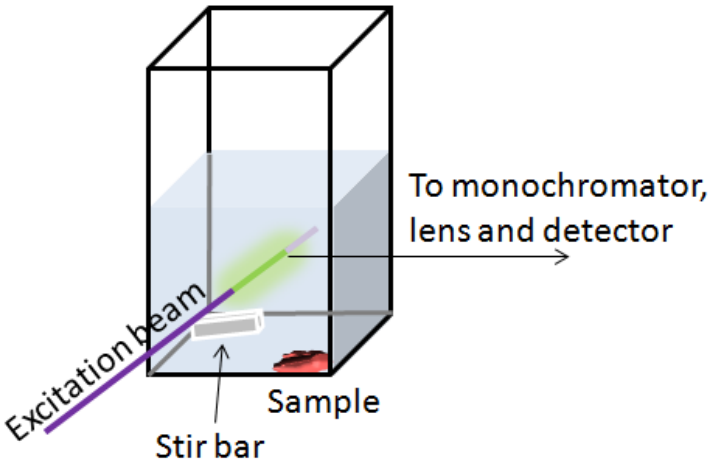

Figure 4.11. Experimental setup for time-resolved fluorescence spectroscopy. An excitation beam is aimed at the solution supernatant, exciting any dye molecules present. A CCD detector cooled to liquid nitrogen temperatures integrates intensities at a specified wavelength in real-time to generate a typical release profile curve.

4.7 References

(1) Browne, R. W.; Feringa, L. B. *Nat. Nanotechnol.* **2006**, 1, 25-35.

(2) Lin, Y-S.; Hurley, K. R.; Haynes, C. L. *J. Phys. Chem. Lett.* **2012**, 3, 364-374.

(3) Cheon, J.; Lee, J. H. *Acc. Chem. Res.* **2008**, 41, 1630-1640.

(4) Ambrogio, W. M.; Thomas, R. C.; Zhao, Y.; Zink, I. J.; Stoddart, J. F. *Acc. Chem. Res.* **2011**, 44, 903-913.

(5) Slowing, I. I.; Trewyn, G. B.; Giri, S.; Lin, S. V. *Adv. Funct. Mater.* **2007**, 17, 1225-1236.

(6) Davis, M. E. *Nature* **2002**, 417, 813-821.

(7) Zhao, S. X.; Lu, Q. G.; Whittaker, K. A.; Millar, J. G.; Zhu, Y. H. *J. Phys. Chem. B* **1997**, 101, 6525-6531.

(8) Vallet-Regi, M.; Ramila, A.; del Real, P. R.; Perez-Pariente, *J. Chem. Mater.* **2001**, 13, 308-311.

(9) Kruk, M.; Jaroniec, M. *J. Phys. Chem. B* **1997**, 101, 583-589.

(10) Slowing, I. I.; Escoto-Vivero, J. L.; Wu, C.-W.; Lin, V. S.-Y. *Adv. Drug Deliv. Rev.* **2008**, 1278-1288.

(11) Nguyen, T. D.; Tseng, H. R.; Celestre, P. C.; Flood, A. H.; Liu, Y.; Stoddart, J. F.; Zink, J. I. *Proc. Natl. Acad. Sci. USA* **2005**, 102, 10029-10034.

(12) Trewyn, B. G.; Slowing, I. I.; Giri, S.; Chen, H.-T.; Lin, V. S.-Y. *Acc. Chem. Res.* **2007**, 40, 846-853.

(13) Ferris, D.P.; Zhao, Y.-L.; Khashab, N.M.; Khatib, H.A.; Stoddard, J.F.; Zink, J. I. *J. Am. Chem. Soc.* **2009**, 131, 1686-1688.

(14) Zhao, Y.; Li, Z.; Kabehie, S.; Botros, Y. Y.; Stoddart, J. F.; Zink, J. I. *J. Am. Chem. Soc.* **2010**, 132, 13016-13025.

(15) Meng, H.; Xue, M.; Xia, T.; Zhao, Y.; Tamanoi, F.; Stoddart, J. F.; Zink, J. I. *J. Am. Chem. Soc.* **2010**, 132, 12690-12697.

(16) Coti, K. K.; Belowich, M. E.; Liong, M.; Ambrogio, M. W.; Lau, T. A.; Khatib, H. A.; Zink, J. I.; Khashab, N. M.; Stoddart, J. F. *Nanoscale* **2009**, 1, 16-39.

(17) Li, Z.; Barnes, J. C.; Bosoy, A.; Stoddart, J. F.; Zink, J. I. *Chem. Soc. Rev.* **2012**, 41, 2590-2605.

(18) Patel, K.; Angelos, S.; Dichtel, W. R.; Coskun, A.; Yang, Y.-W.; Zink, J. I.; Stoddart, J. F. *J. Am. Chem. Soc.* **2008**, 130, 2382-2383.

(19) Fu, Q.; Rao, V.-R.; Ista, L. K.; Wu, Y.; Andrzejewski, B. P.; Sklar, L. A.; Ward, T. L.; Lopez, G. P. *Adv. Mater.* **2003**, 15, 1262-1266.

(20) Vivero-Escoto, J. L.; Slowing, I. I.; Trewyn, B. G.; Lin, V. S.-Y. *Small* **2010**, 6, 1952-1967.

(21) Climent, E.; Martínez-Máñez, R.; Sancenón, F.; Marcos, M. D.; Soto, J.; Maquieira, A.; Amorós, P. *Angew. Chem. Int. Ed.* **2010**, 49, 7281-7283.

(22) Mal, N. K.; Fujiwari, M.; Tanaka, Y. *Nature* **2003**, 23, 350-353.

(23) Thomas, C. R.; Ferris, D. P.; Lee, J. H.; Choi, E.; Kim, E. S.; Stoddart, J. F.; Shin, J. S.; Cheon, J.; Zink, J. I. *J. Am. Chem. Soc.* **2010**, 132, 10623-10625.

(24) Lu, J.; Choi, E.; Tamanoi, F.; Zink, J. I. Small **2008**, 4, 421-426.

(25) Mal, N. K.; Fujiwara, M.; Tanaka, Y.; Taguchi, T.; Matsukata, M. *Chem. Mater.* **2003**, 15, 3385-3394.

(26) Lu, J.; Liong, M.; Zink, J. I.; Tamanoi, F. *Small* **2007**, 3, 1341-1346.

(27) Zheng, H.; Huang, Z.; Che, S. *Dalton Trans.* **2012**, 41, 5038

(28) Chouyyok, W.; Shin, Y.; Davidson, J.; Samuels, W.; La Fermina, H. N.; Rutledge, D. R.; Fryxell, G.; Sanvanich, T.; Yantasee, W. *Environ. Sci. Technol.* **2010**, 44, 6390-6395.

(29) Busche, B.; Wiacek, R.; Davidson, J.; Koonsiripaiboon, V.; Yantasee, W.; Addelman, R. S.; Fryxell, E. G. *Inorg. Chem. Commun.* **2009**, 12, 312-315.

(30) Young, R. S. *Cobalt in biology and biochemistry***,** Academic Press Inc: London, **1979**.

(31) Denkhaus, E.; Salnikow, K. *Crit. Rev. Oncol. Hematol.* **2002**, 42, 35-56.

(32) Mattson, M. P.; Chan, S. L. *Nat. Cell. Biol.* **2003**, 5, 1041-1043.

(33) Orrenius, S.; Zhivotovsky, B.; Nicotera, P. *Nat. Rev. Mol. Cell. Bio.* **2003**, 4, 552-565.

(34) Hofer, A. M.; Brown, E. M. *Nat. Rev. Mol. Cell. Bio.* **2003**, 4, 530-538.

(35) Rizzuto, R.; Pinton, P.; Ferrari, D.; Chami, M.; Szabadkai, G.; Magalhães, P. J.; Virgilio, F. D.; Pozzan, T. *Oncogene* **2003**, 22, 8619-8627.

(36) Bernauer, L.; Walz, D.; Fallab, S. *Helv. Chim. Acta.* **1958**, 41, 2094-2099.

(37) Schwarzenbach, G.; Anderegg, G.; Schneider, W.; Senn, H. *Helv. Chim. Acta* **1955**, 38, 1147.

(38) Irving, H.; Mellor, D. H. *J. Chem. Soc.* **1962**, 5222-5237.

(39) Angelos, S.; Liong, M.; Choi, E.; Zink, J. I. *Chemical Engineering Journal* **2008**, 137, 4-13.

(40) Hiemstra, T.; de Wit, J. C. M.; van Riemsdijk, W. H. *J. Colloid Interface Sci.* **1989**, 133, 105-117.

(41) Li, Z.; Nyalosaso, L. J.; Hwang, A. A; Ferris, P. D.; Yang, S.; Derrien, G.; Charnay, C.; Durand, J. O.; Zink, J. I. *J. Phys. Chem. C* **2011**, 115, 19496-19506.

(42) J. Lu, M. Liong, J. I. Zink and F. Tamanoi, *Small*, **2007**, 3, 1341–1346.

(43) Mattson, P. M.; Chan, S. L. *Nat. Cell Biol.* **2003**, 5, 12, 1041-1043.

CHAPTER 5

In Vitro Delivery of Calcium Ions

With Nanogated Mesoporous Silica Nanoparticles

to Induce Cancer Cellular Apoptosis

5.1 Abstract

A pH operated nanogate on mesoporous silica nanoparticles (MSN) capable of a simultaneous dual-cargo delivery of both 1-2 nm sized cargo and small metal ions was used to deliver both Hoechst 33342 nuclear stain and calcium ions to MiaPaCa-2 cancer cells. Treatment of cancer cells with Hoechst loaded, calcium latched nanogate modified MSN resulted in the autonomous release of both cargo types, as visualized by cell nuclei staining and calcium induced apoptosis. The delivery of calcium ions to the cancer cells caused cellular apoptosis as indicated with the presence of apoptotic bodies and high levels of cell killing.

5.2 Introduction

Mesoporous silica nanoparticles (MSN) have been shown to be readily endocytosed by cancer cells within a 30 minute period without apparent cytotoxicity.[1, 2] Once uptaken, the intracellular location of fluorescently labeled MSN can be determined by staining the cells with acridine orange.[1] Based on these results, the MSN are observed to localize in the cell lysosomes, where the pH is typically from 5-7.[3] In the previous chapter, we described the design, synthesis and operation of a pH operated nanogate consisting of iminodiacetic acid modified MSN. Because the IDA nanogate is a machine that is activated at low pH, it was envisioned that this design would be applicable to biology. Cells can be treated with IDA-MSN nanoparticles, and once endocytosed, the low lysosomal pH would cause release of both cargo types. Excess calcium is known to orchestrate cellular apoptosis.[4, 5, 6, 7]

Calcium's storage is normally highly regulated inside cells; the large presence of calcium in the cell cytoplasm induces a positive feedback loop that ultimately results in cell apoptosis (Figure 5.1). The release of calcium into the cytoplasm (which can be triggered through a broad variety of biological responses) causes a mitochondrial release of cytochrome C (Figure 5.1a). Upon finding its way to the endoplasmic reticulum (ER), where the majority of intracellular calcium is stored, binding of cytochrome C with receptors on the ER causes endoplasmic release of calcium (Figure 5.1b), which in return, results in additional cytochrome C release from the mitochondria (Figure 5.1c). This positive feedback loop results in toxic concentrations of cytoplasmic calcium, ultimately causing the formation of an apoptomer and cell apoptosis (Figure 5.1f). By artificially delivering calcium to the cell cytoplasm, we hope to stimulate this apoptotic cycle and induce cellular death via a delivery of calcium as an alternative to using traditional, more hazardous chemotherapy drugs.

5.3 Results and Discussion

5.3.1 Autonomous pH Activated Release of Cargo

To test the autonomous release of cargo by pH of the IDA-MSN, MiaPaCa-2 cells were treated with a sample of IDA modified MSN loaded with Hoechst 33342 nuclear stain latched with calcium. From these results, we see that the lysosomal pH causes cargo release, illustrated in the blue fluorescent nuclear staining observed in Figure 5.2a. To verify the calcium latch is necessary to hold back the Hoechst cargo, a control was performed where the cells were treated with IDA-MSN loaded with Hoechst but unlatched. In this sample, trivial Hoechst nuclear staining is observed, due to all of the Hoechst cargo being washed out of the nanoparticle pores during the washing steps (Figure 5.2b). This indicates that the calcium latch is responsible for successful cargo trapping inside the MSN pores. Cells treated with this sample show no fluorescence staining, confirming that the observed fluorescence in Figure 5.2a is due to released Hoechst. It is noteworthy to mention that signs of cellular apoptosis were present in the cells treated with calcium latched IDA-MSN (Figure 5.3). In this Hoechst stained sample, bright, condensed fluorescence was observed in a number of the treated cells (Figure 5.3), signifying collapsed nuclei and indicating the progression of cell death through an apoptotic mechanism.

5.3.2 Cell Killing with Calcium Delivery

To quantify the observed cell death, a cell viability assay was conducted (Figure 5.4). While control samples of unlatched Hoechst loaded IDA-MSN and plain IDA-MSN showed no toxicity within the dosage range, a sample of Hoechst loaded, calcium latched IDA-MSN demonstrated a high amount of cell killing at very low nanoparticle concentrations (1.5 μg/mL, Figure 5.4). Exclusion of calcium from the control samples resulted in no cell toxicity, suggesting that the observed cell killing is due to a controlled delivery of calcium. It is important

to note that the free chelating properties of unloaded IDA-MSN do not cause cell toxicity even at high dosages (100 μg/mL), making this design a viable option for biological use.

5.3.3 Lysosomal Neutralization and Suppression of Cargo Release

The pH activated mechanism of release was further corroborated by testing for cargo release after neutralizing the cell lysosomes. MiaPaCa-2 cells were stained with acridine orange, a pH indicating dye, before treated with bafilomycin A1 to neutralize the lysosomes. In Figure 5.5, the neutral cellular components of cells stained with acridine orange appear with green fluorescence (Figure 5.5 top right frame), while the acidic lysosomal compartments appear orange/red under confocal microscopy (Figure 5.5 top left frame). Once treated with bafilomycin A, the cell appears uniformly with green fluorescence (Figure 5.5 top right frame), indicating that the lysosomes have been neutralized. Dosing the pH neutralized cells with IDA-MSN loaded with Hoechst and latched with calcium resulted in very little nuclear staining (Figure 5.5 bottom right frame). Dosing a control group of cells not neutralized with bafilomycin with the same group of IDA-MSN resulted in Hoechst nuclear staining (Figure 5.5 bottom left frame). This indicated that neutralization of the cell lysosomes did not result in the release of Hoechst, and that the cell lysosomal compartments must be acidic in order to autonomously release cargo from loaded IDA-MSN, in good agreement with our solution study results (Chapter 4, Figure 4.3a, 4.3b).

5.4 Summary

In summary, after successful design, synthesis and operation of IDA nanogated MSN, this system was used to deliver both calcium and Hoechst 33342 nuclear stain to MiaPaCa-2 cancer cells. Treatment of the cells with IDA-MSN resulted in lysosomal localization of the nanoparticles. The intrinsic low lysosomal pH allows for the autonomous release of both cargo types, as visualized by Hoechst nuclear staining and calcium induced apoptosis. The delivery of calcium the cancer cells resulted in high amounts of cell killing, while a control set of particles which lacked calcium were found to be non-toxic.

5.5 Figures

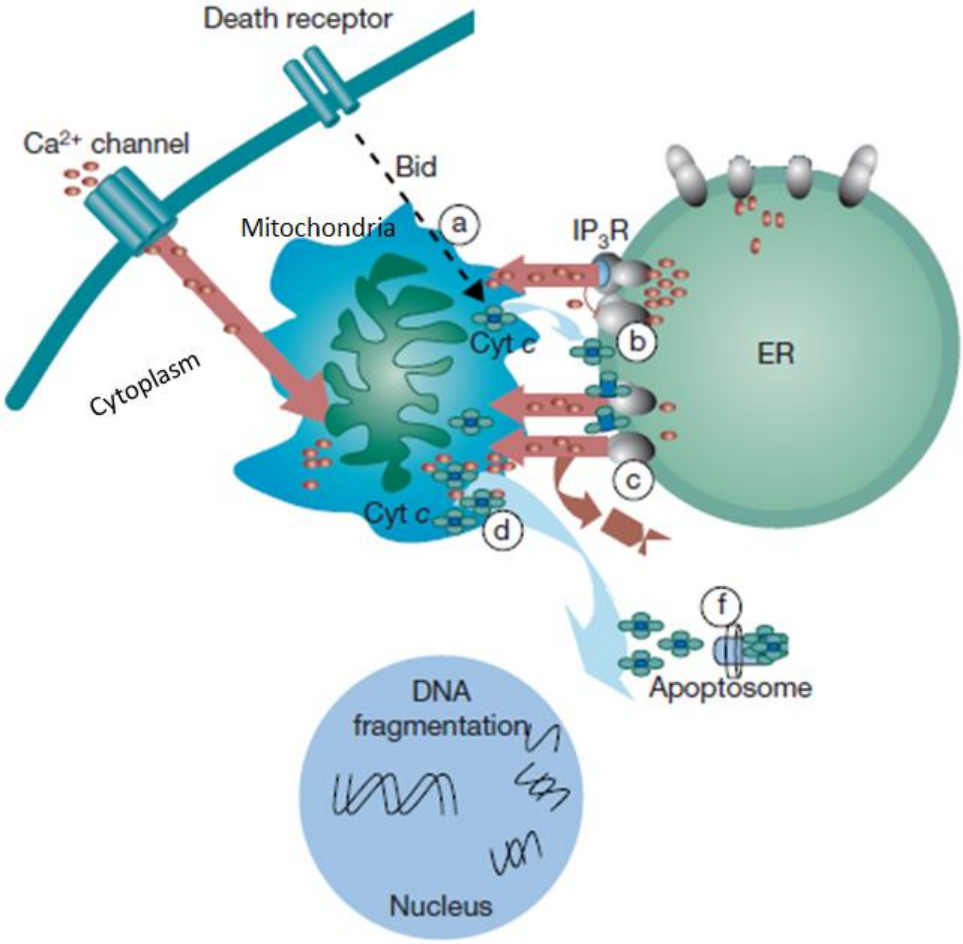

Figure 5.1. The role of calcium in orchestrating cellular apoptosis. (a) Release of the death receptor Bid or influx of calcium into the cell cytoplasm causes the mitochondria to release cytochrome c. (b) Some of the released cytochrome C ultimately binds to receptors on the endoplasmic reticulum (ER), causing an outflux of calcium to the cytoplasm. (c) An increased presence of calcium in the cytoplasm causes the mitochondria to release additional cytochrome C, generating a positive feedback loop. (d) Upon calcium concentrations reaching cytotoxic levels, an apoptosome (f) is assembled which leads to cell apoptosis. Adapted from reference 4.

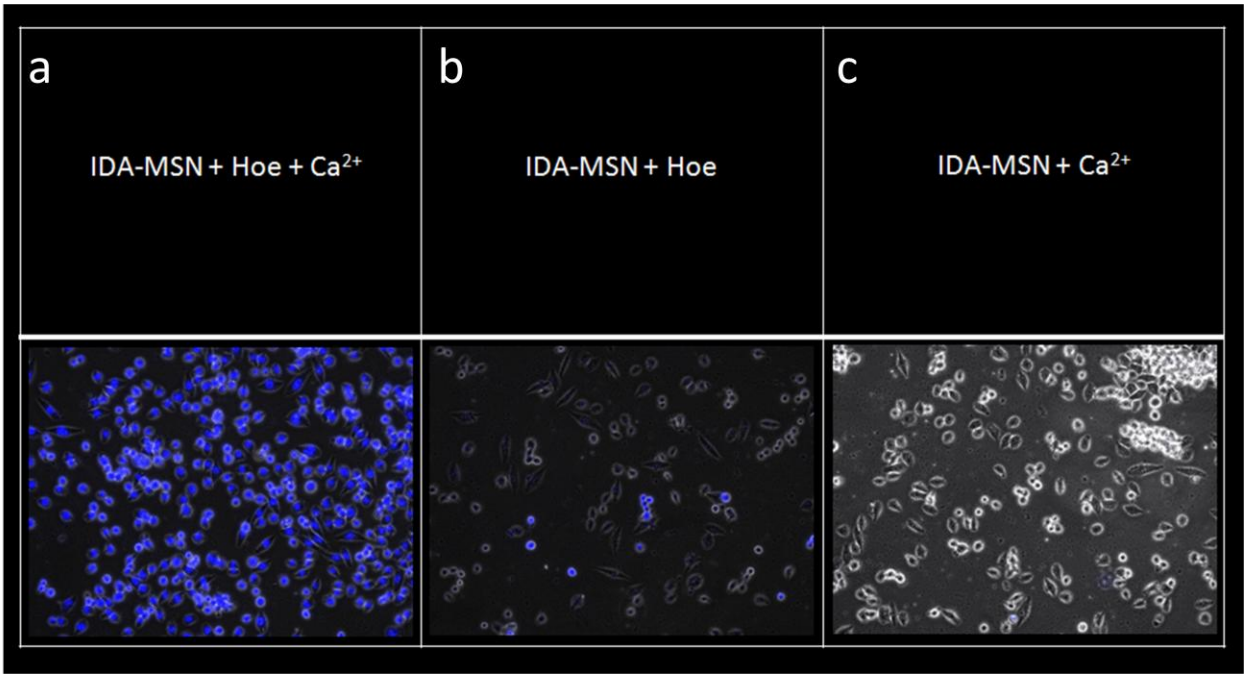

Figure 5.2. Hoechst 33342 nuclear staining of MiaPaCa-2 cells. (a) A cell sample treated with Hoechst loaded, calcium latched nanogates showing blue fluorescent staining of cellular nuclei caused by the autonomous release of Hoechst. Nanoparticles are uptaken by endocytosis and localize in the cellular lysosomal compartments. The lower lysosomal pH causes unlatching of calcium and release of the store Hoechst dye. (b) A control sample where the nanomachine was assembled and loaded with Hoechst, but the latching steps with calcium omitted. In this sample, most of the loaded Hoechst dye is removed during the washing steps, therefore, little cellular staining is observed after treatment to cells. (c) A control sample of calcium latched IDA-MSN not loaded with Hoechst to verify the observed blue fluorescence is due to the Hoechst dye.

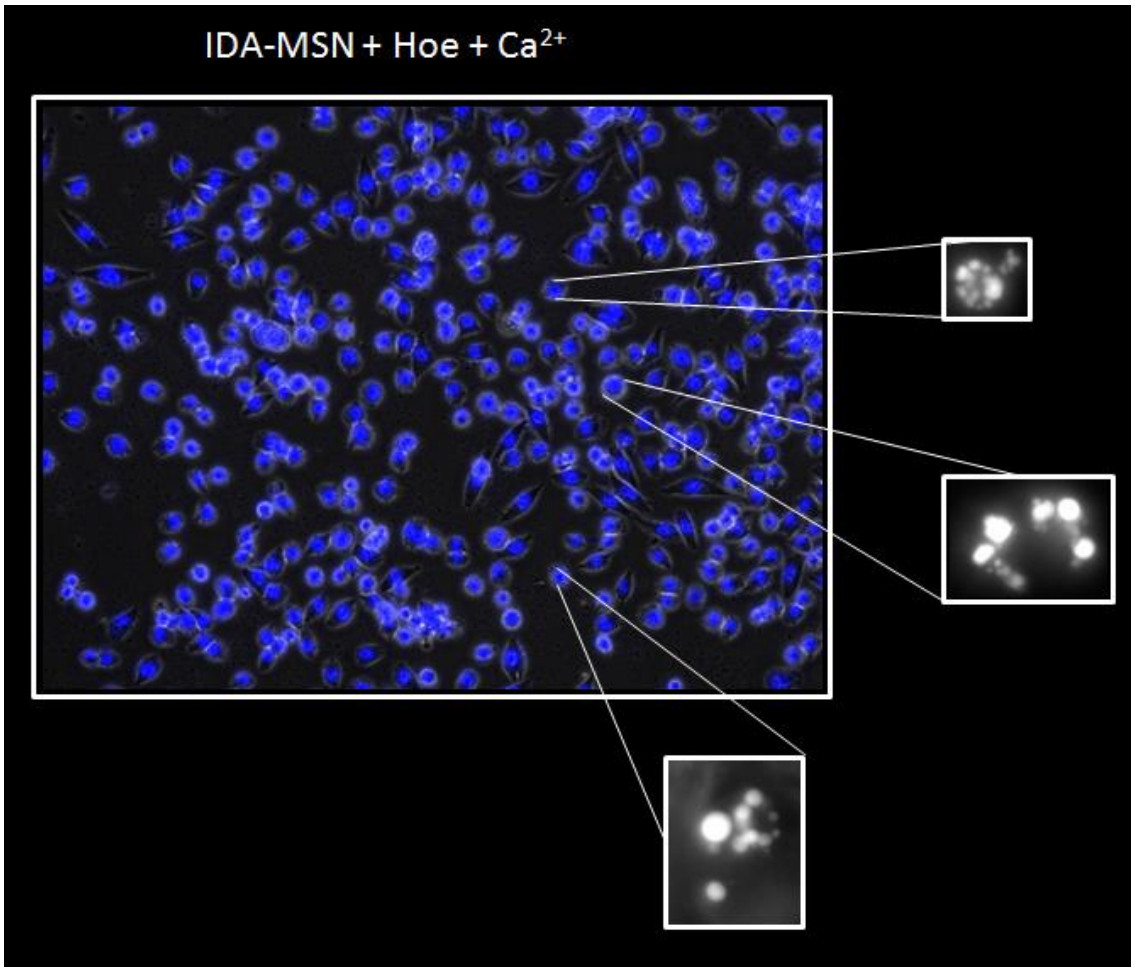

Figure 5.3. MiaPaCa-2 cells treated with IDA-MSN loaded with Hoechst and latched with calcium. The bright regions of highly condensed fluorescence are signs of a collapsed cellular nucleus, indicating a cell apoptosis process.

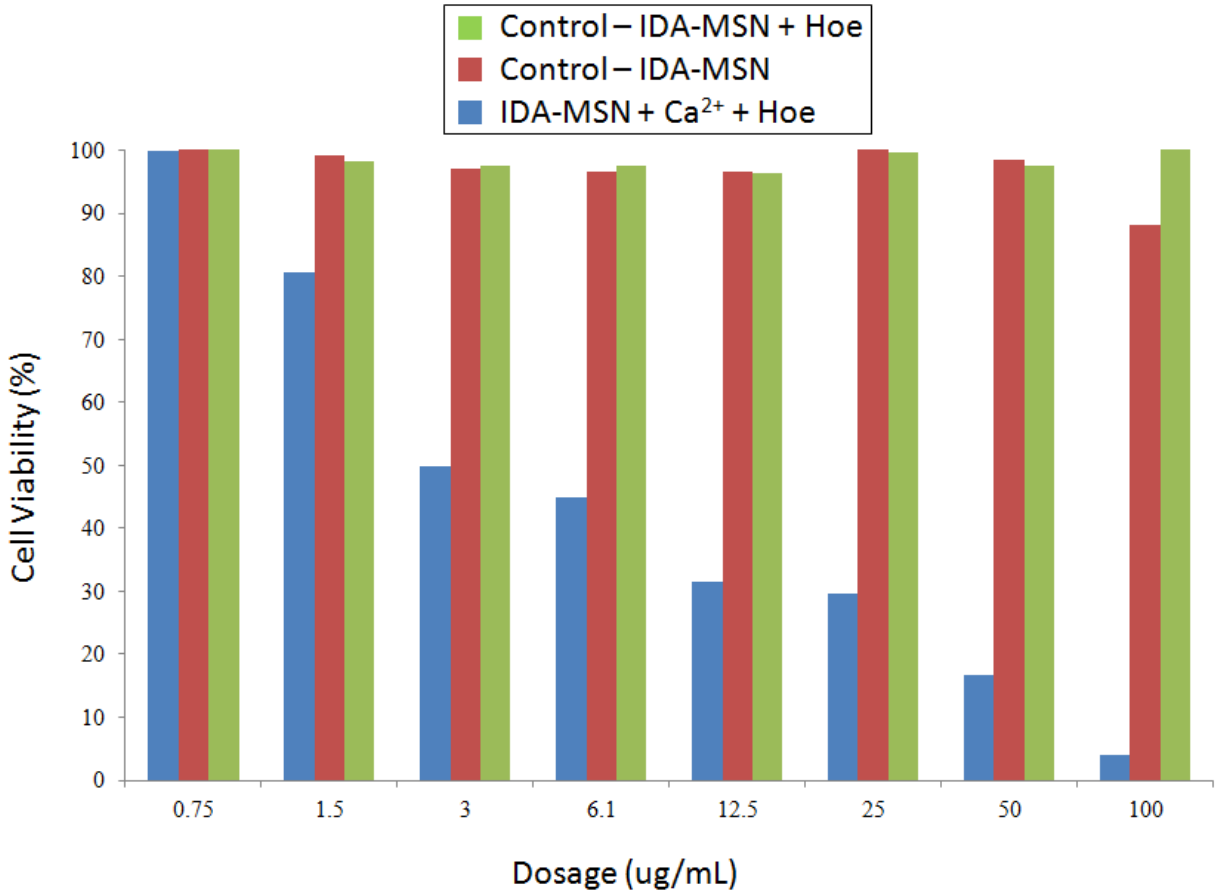

Figure 5.4. Cell viability assay of MiaPaCa-2 cells treated with (1) Hoechst loaded, calcium latched IDA-MSN, (2) Control - IDA modified MSN, and (3) Control - IDA modified MSN loaded with Hoechst but unlatched. Both control samples show no cell killing within the dosage applied. Cell death is only observed when the IDA-MSN is latched with calcium. This suggests that a delivery of calcium causes cell death. Signs of apoptosis shown in Figure 5.3 from a similarly treated cell sample suggest an apoptotic method.

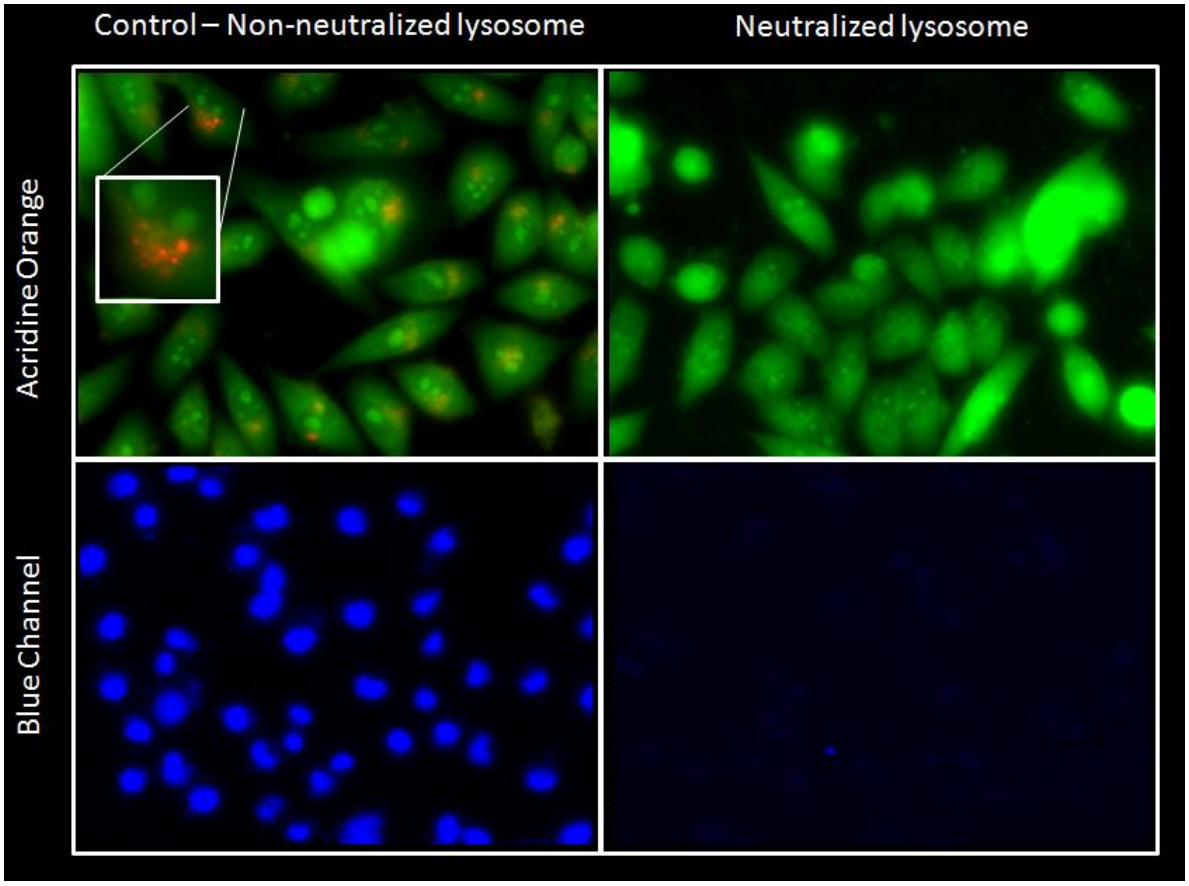

Figure 5.5. Confocal microscopy images of MiaPaCa-2 cells treated with Hoechst loaded, calcium latched IDA-MSN. The top frames show the outline of cells stained with acridine orange, a pH sensitive dye that fluoresces green at neutral pH, but red/orange at low pH. In the right frames, the cellular lysosome was neutralized by treatment with bafilomycin A1. In the green channel, the uniform presence of green fluorescence indicates that the lysosomes in this sample are of neutral pH. Subsequent treatment of these cells with Hoechst loaded, calcium latched IDA-MSN resulted in negligible Hoechst nuclear staining, which indicates that a low lysosomal pH is required to unlatch the nanogates and release cargo. In the left frames, a control shows that when the lysosomes are not neutralized with bafilomycin A1 treatment, Hoechst nuclear staining is observed. This demonstrates that the nanogates are activated by a low lysosomal pH.

5.6 References

(1) J. Lu, M. Liong, J. I. Zink and F. Tamanoi, *Small*, **2007**, 3, 1341–1346.

(2) Coti, K. K.; Belowich, M. E.; Liong, M.; Ambrogio, M. W.; Lau, T. A.; Khatib, H. A.; Zink, J. I.; Khashab, N. M.; Stoddart, J. F. *Nanoscale* **2009**, 1, 16-39.

(3) Li, Z.; Barnes, J. C.; Bosoy, A.; Stoddart, J. F.; Zink, J. I. *Chem. Soc. Rev.* **2012**, 41, 2590-2605.

(4) Mattson, M. P.; Chan, S. L. *Nat. Cell. Biol.* **2003**, 5, 1041-1043.

(5) Orrenius, S.; Zhivotovsky, B.; Nicotera, P. *Nat. Rev. Mol. Cell. Bio.* **2003**, 4, 552-565.

(6) Hofer, A. M.; Brown, E. M. *Nat. Rev. Mol. Cell. Bio.* **2003**, 4, 530-538.

(7) Rizzuto, R.; Pinton, P.; Ferrari, D.; Chami, M.; Szabadkai, G.; Magalhães, P. J.; Virgilio, F. D.; Pozzan, T. *Oncogene* **2003**, 22, 8619-8627.

CHAPTER 6

Coated Silicalite-1 Nanoparticles for the Controlled Delivery of Small Ions Including Oxidants

6.1 Abstract

Silicalite-1 nanoparticles (S1NP) are synthesized, characterized, and rehydrated to allow for the loading of small ionic cargo molecules including cobalt and a strong oxidizing agent, $KClO_4$. To allow successful storage and delivery of its cargo, after loading, S1NP are coated with a thin ~5 nm layer of long chain fully saturated hydrocarbons using a two-phase molten wax method. This coating is demonstrated to be able to seal in and release cobalt(II) ions and perchlorate upon heating (>50 ^{o}C). Even after storage, the delivered perchlorate retains its oxidative potential as shown in its oxidation of cyanine 3.

6.2 Introduction

Silicalite-1 nanoparticles (S1NP) are a zeolitic type of silica first characterized by Flanigen et al. are unique for their high level of crystallinity and hydrophobic nature.[1] Zeolites show a uniform micropore structure and have been widely employed for use as catalysts, molecular sieves or for ion-exchange applications.[2, 3] As a pure silica zeolite, silicalite-1 displays properties similar to MFI type-zeolites in its adsorption of molecules < 0.6 nm.[1, 4, 5, 6, 7] Its adsorption characteristics are unique when compared to other types of molecular sieves in that silicalite can adsorb both hydrophobic[1] and hydrophilic[4] cargo types. Despite being shown to be non-toxic to cells,[8, 9, 10] reported biological applications are very limited[11] and do not involve use of their micropores to achieve their goals.[12] This stems from the difficulty in both finding a useful cargo that can be efficiently included inside the pore structure, and in developing a system capable of trapping and releasing the cargo on demand.

The S1NP pore structure has been well-studied; it exists as an elliptical, 3D-interconnected channels varying from 0.5-0.6 nm (Figure 6.1d).[1, 13, 14, 15] This size restriction poses two problems when using S1NP as a cargo delivery vehicle: choosing a cargo molecule under 0.6 nm that can be efficiently loaded inside its pores, and developing a system that can hold back cargo of that size. While the most recent highlights of drug delivery designs have been centered on the delivery of chemotherapeutic drugs,[16, 17, 18, 19] there remains considerable interest in the delivery of small cargo as biorelevent ions; their delivery can be used to induce a cellular response[20, 21, 22, 23] or to probe ion specific cytotoxicity.[24, 25] In addition, strong, small oxidizing agents can be used to sanitize and to kill highly drug-resistant microbes.[26, 27]

Oxidizing agents have found therapeutic application as antiseptics and disinfectants.[28] An attractive advantage of its use is that a single oxidizer can act against multiple types of microbes;

hydrogen peroxide can be used to render working spaces sterile and even decontaminate robust anthrax spores.[29, 27] However, this property also makes them inherently toxic; this creates a need to encapsulate these as cargo to be safely stored away and released on command. While the delivery of small metal ions has recently been reported on mesoporous silica nanoparticles using coordinational chemistry,[30, 31, 32, 33] a strong oxidizing agent such as perchlorate would be incompatible with these systems as it can both potentially react with the surface derivitizations and are unable to form coordinational complexes with the reported ligands.

To create a versatile delivery system that can include both non-coordinating metal ions and strong oxidizing agents as cargo, S1NP can be encapsulated with an inert surface coating to seal in the loaded cargo molecules. Here, the use of a robust, hydrophobic long-chain hydrocarbon coating can accomplish the dual task of sealing in the small cargo molecules, and provide a chemically inert barrier for the storage of strong oxidizers. This provides an advantage to the chelation based designs; non-coordinating small cargo can be trapped along with metal ions. In addition, the exclusion of reactive organic functional groups allows for a higher level of chemical inertness, which can prevent undesired cargo reactivity. By introducing a method to allow S1NP to deliver small, reactive cargo molecules, we hope to broaden the appeal of silicalite-1 as a cargo delivery vehicle. In this chapter, we demonstrate that a simple solid coating of saturated hydrocarbons on S1NP can allow it to store and deliver small cargo molecules, including a strong oxidizing agent, perchlorate.

6.3 Results and Discussion

6.3.1 Synthesis of Silicalite-1

Silicalite-1 nanoparticles were synthesized using a commonly used sol-gel method by aging in basic conditions before initiating crystal growth.[1] The resulting microporous material was then calcined to remove the organic templating agent and allow for pore access. Micropore structure and crystallinity of the nanoparticles was verified through powder XRD, which exhibited characteristic sharp, well-defined peaks indicative of a high level of SiO_2 crystallinity (Figure 6.6). This result is also corroborated by high-resolution TEM, which displays characteristic diffraction patterns indicative of high crystal packing order (Figure 6.1b). SEM, TEM and DLS readings were also used to verify the particle sizes were between 50-70 nm (Figure 6.1a, Figure 6.1c) and monodispersity in aqueous environments rehydration (See Experimental Section, Figure 6.7).

As a result of being calcined, a majority of surface silanol (Si-OH) groups on S1NP were converted to siloxanes (Si-O-Si),[10] which caused the surfaces to be both relatively hydrophobic and unreactive. TGA analysis of calcined S1NP indicates a low weight percent of silanol groups, but upon rehydration of the silica surface, the usable silanol density increases by two-fold (Figure 6.8). The surface density of silanol groups is not only important for silanol exchange reactions, but for particle stability in aqueous environments (Figure 6.7). Once calcined, S1NPs are highly aggregated in water as a result of their hydrophobicity (Figure 6.9a), but regeneration of the surface silanols can allow for high dispersibility, and for the loading of small, hydrophilic cargo (Figure 6.9b).

6.3.2 Loading of Cobalt

To test the viability of the wax coating as a method to seal in and retain cargo, S1NP were loaded with cobalt(II) (ionic radii: 0.08 nm).[34] After rehydrating S1NP and restoring surface silanol groups (Figure 6.8), which ionize into $Si\text{-}O^-$ in neutral pH,[35] favorable electrostatics were introduced to aid inclusion of the cationic cobalt inside the pores. To prevent oversolvation and the formation of a water sphere around S1NP, the cobalt cargo was loaded in an ethanoic solution of cobalt(II) chloride. After loading, the nanoparticles were collected by centrifugation and vacuum dried to prepare them for surface coating.

6.3.3 Choice of Surface Coating

In order for the surface coating to be functional, it must be simultaneously inert against strong oxidizing agents, stable in aqueous conditions, and be removable under reasonable conditions to achieve cargo release. The high reactivity of strong oxidizing agents to many organic functional groups limits the types of cargo storing designs that can be used. To address this problem, a robust system was designed in which after loading the strong oxidizer, the nanoparticle is coated with a chemically inert hydrocarbon layer to seal in the cargo without itself being oxidized. While simple aromatic hydrocarbons such as benzene (which have been shown to adsorb strongly to silicalites)[36, 37] can theoretically be easily removed to release cargo, nanoparticles coated with benzene were found to be unstable for extended periods of time, especially when sonicated. Gas phase adsorption of volatile organics such as naphthalene did not provide a complete enough seal to prevent the leakage of cargo in aqueous environment. Therefore, a non-volatile solid coating was considered. Because commercially available paraffin wax is solid at room temperature and can be fractionated to melt at different temperatures, it was chosen as the wax coating. In addition, the completely saturated hydrocarbon composition of

paraffin wax makes it very difficult to oxidize. The paraffin wax used in this experiment has a melting point range from 52-57 ^{o}C. This range was chosen because we have previously shown it to be an obtainable temperature by inductive heating of silica nanoparticles with an iron-oxide core shell.[38]

Due to the relatively hydrophobic outer surface of S1NP,[1] it can be easily coated with a hydrophobic wax shell. The wax coating can be melted off with heat and allow the loaded S1NP to deliver its cargo (Figure 6.2a). This simple type of design can allow for the delivery of strong oxidizing agents; a coating of chemically inert paraffin wax can seal in highly reactive cargo without itself being oxidized. The methods of introducing surface coatings to nanoparticles range from solvent self-assembly,[39] chemical attachment,[40] electrostatic interactions,[41] and the use of emulsions.[42] The difficulty in modifying hydrocarbon wax to introduce a chemically inert, covalent attachment to S1NP or predicting it self-assembly behavior makes these routes infeasible. Therefore, a new method of dip coating in molten wax followed by rapid cooling was developed and used to ensure an even and thin coated S1NP. In this method, a two-phase system composed of a molten paraffin wax layer and a cooler aqueous phase is utilized. Loaded S1NP are suspended in the wax phase via sonication before centrifuging the nanoparticles down to the aqueous layer. Upon reaching the cold aqueous phase, rapid cooling of an adsorbed layer of molten wax solidifies a sphere of paraffin wax around S1NP (Figure 6.2b). In this way, a thin coating of wax can be introduced onto S1NP.

6.3.4 Coating the Surface

The wax coating was accomplished by suspending the cargo loaded, dried particles in dichloromethane (DCM) before mixing with molten wax. By controlling heating and sonication time, the DCM carrier solvent is selectively evaporated out of the wax suspension. To prevent

formation of a solid layer of wax at the water / wax interface, a buffer layer of hot water was added. After equilibrating the two phases, a layer of cold brine solution was injected with a hypodermic needle to the bottom of the aqueous phase before centrifuging down the suspended S1NP. Movement of the nanoparticles from the molten hot wax to the cooler water layer solidifies a shell of paraffin wax around S1NP, forming a thin coat around the nanoparticle (Figure 6.2b). Through careful temperature control of both the organic and aqueous phases, a thin coating of wax can be achieved. After a successful coating of wax, the nanoparticles were washed repeatedly with water to remove the excess.

To probe the thickness of the wax coating, a non-loaded S1NP sample coated with wax was analyzed through TGA. Compared to bare silica samples, TGA of this sample showed a 12% weight loss by heating to 500 ^{o}C which can be attributed to the loss of wax on this sample (Figure 6.12). Based on our calculations, this weight loss corresponds to a wax coating approximately 5 nm in thickness (Figure 6.18). This number is corroborated by TEM imaging. Figure 6.3a shows the image of a coated S1NP stained with uranyl acetate. In this sample, a high contrast outer shell can be observed surrounding each nanoparticle compared to uncoated S1NP also stained with uranyl acetate (Figure 6.19). Using image analysis software, the thickness of the dark shell was determined to be between 3-7 nm by TEM, which is in close agreement with our calculations from the TGA data (5 nm).

To further verify that the wax coating is a thin coating and not nanoparticles trapped in large wax agglomerates, a control was performed where S1NPs were suspended in a molten solution of paraffin wax. Upon cooling, this sample was crushed and analyzed with TEM and SEM. Without contrast staining, TEM imaging of this control sample showed large dark fringes (extending roughly 50 nm from each S1NP) around each individual nanoparticle suggesting the

nanoparticles are encased in large agglomerates of organic material. SEM of this sample also showed large wax chunks (>100 μm) which have surfaces textured with encased nanoparticles (Figure 6.11). Both these characteristics were not present in TEM and SEM imaging of S1NP coated with the thin wax method, as individual S1NP are easily distinguishable in both TEM and SEM images (Figure 6.3b). This agrees with the uranyl acetate staining results, confirming that the described method results in a thin ~5 nm wax coat on S1NP.

6.3.5 Release of Cobalt

After successful loading of cobalt and coating with a thin layer of wax, the assembled S1NP were tested using continuous spectroscopic monitoring (Figure 6.13). Due to the difficulty of monitoring cobalt(II) by absorption spectroscopy, its real-time release was indirectly measured through monitoring its fluorescence quenching effects on calcein dye. A control experiment demonstrates the fluorescence quenching effect of calcein with the introduction of cobalt(II); at a ratio of 1:10 (cobalt : calcein), an almost complete fluorescence quenching of calcein was observed (Figure 6.15). This method is demonstrated to be sensitive enough to detect μmolar quantities of cobalt (Figure 6.15). By monitoring the fluorescence decay of calcein dye in a TRFS spectroscopy setup, the real-time release of cobalt can be visualized.

Using the cobalt loaded, wax coated S1NP, a baseline fluorescence was collected prior to initiating cargo release through heating. The slope of the baseline is slightly increasing (corresponding to fluorescence decay) as shown in Figure 6.4a, but an increasing slope is also similarly observed when irradiating calcein dye with a probe beam in the absence of S1NP (Figure 6.14), suggesting that this decay is likely the result of photobleaching rather than from premature leakage of cobalt. Once heat is applied, an immediate increase in slope is observed due to the temperature dependence of calcein's fluorescence intensity. In Figure 6.14, a solution

of calcein dye (in which S1NP were excluded) was subjected to the same heating curve as used in the experiment. In these results, it was observed that, upon heating, calcein dye experiences a fluorescence quenching, but returns to its baseline fluorescence intensity upon cooling (Figure 6.14). Due to this heat dependence, it is not possible to conclude successful cobalt release by observing the immediate quenching effects on calcein when hot. Therefore, the sample was allowed to cool to room temperature after heating in order to compare the baseline fluorescence intensities with the post-heating and cooling intensities. When comparing the data shown in Figure 6.4a to those from a free calcein dye solution (Figure 6.14), the cobalt loaded sample initially follows the same fluorescence decay and regeneration curve from 15-60 minutes, but instead of returning back to its baseline fluorescence intensity after cooling (time = 60 minutes), the trace exhibits an inflection point and continues to decay in fluorescence intensity (Figure 6.4a). This suggests that in this sample, cobalt is actively being released as a result of the heating. When compared to a calcein control solution which excludes S1NP, within the same period of time, the fluorescence intensity of the control solution has already returned back to its baseline value, indicating that cobalt has been released in the heated S1NP sample. Because the intensity continues to decay even after cooling the solution to room temperature, this suggests that, once melted, the wax coating is no longer capable encasing the S1NP and prevent additional cargo from being released. The release of cobalt from the wax coated S1NP is visually corroborated in Figure 6.10; the fluorescence intensity of a solution of calcein dye is compared to a sample loaded with cobalt and coated with wax. A side by side image of these two samples under black light shows an initial near identical fluorescence brilliance for both samples prior to heating, but heating and allowing both samples to cool back to room temperature, the fluorescence intensity for the cobalt loaded sample has been noticeably quenched (Figure 6.10).

To directly measure release of cobalt from wax coated S1NP, ICP analysis was employed. After releasing the cobalt by heating and cooling, the supernatant solution was collected and analyzed with ICP-OES to quantify cobalt release. Compared to a control group of unheated cobalt loaded, wax coated S1NP stirred in water for 24 hours, Figure 6.4b indicates that ~10x more cobalt is detected in the heated sample over the control. This result demonstrates that heating causes the release of cobalt from the wax coated S1NP, confirming the results observed in the calcein quenching TRFS trials. As expected for a wax coated S1NP, cobalt ions stored within the S1NP pore structure are encapsulated at room temperature, but heating the sample melts the wax coating and releases cobalt. Based on these results, it was concluded that heating the wax coated S1NP melts the wax coat and releases cobalt.

6.3.6 Release of $KClO_4$

After the demonstrating a controlled release of cobalt from wax coated S1NP, the system was tested for the controlled storage and delivery of a strong oxidizing agent, $KClO_4$. Due to its negative charge, perchlorate loading was maximized when the S1NP were in a highly dehydrated state; the negative charge of ionized silanol groups prevent efficient loading of anionic cargo. Therefore, the S1NP loaded with perchlorate were not rehydrated before loading. The freshly calcinated S1NP were loaded by suspending the S1NP in a concentrated ethanoic solution of $KClO_4$. After allowing time for perchlorate to permeate into the pores of S1NP, the loaded particles were isolated via centrifugation and dried in vacuum to provide a clean outer surface for surface coating. The wax coating was introduced using a similar method as described to coat the cobalt loaded S1NP. To simultaneously determine the release of $KClO_4$ and to monitor its oxidative capability after storage and release, UV-Vis was employed to visualize a real-time release of perchlorate through its oxidation of cyanine 3 (cy3). Cyanine 3 is a dye reported to be

sensitive to oxidation.[43, 44] Oxidation of cy3 was monitored by measuring the absorbance change of the cy3 peak with the addition of $KClO_4$ (Figure 6.17), resulting in a steady decrease in its absorbance maxima (λ = 600 nm). Ratiometric measurement of decay peak and oxidized species growth peak (λ = 525 nm) can allow for real-time monitoring of perchlorate release (Figure 6.17). To verify that cy3 is heat stable, a control experiment was performed where a solution of cy3 was heated under the same heating curve used in experiment while tracking the absorption maxima (Figure 6.16). Monitoring the absorbance change in this sample shows that the absorbance of cy3 increases slightly upon heating, but returns to its original value after being cooled. Using this method, the release of perchlorate from the wax coated S1NP was visualized.

$KClO_4$ loaded, wax coated S1NP were added to a solution of cy3 dye. A baseline absorbance of cy3 was collected every 10 minutes for 30 minutes and shows a stable absorbance of cy3 (Figure 6.5a). Upon heating, the absorbance of cy3 remains stable until the temperature of the solution exceeds 50 ^{o}C, when the absorbance of cy3 begins to decline, suggesting that the melting point of the wax coating has been reached (Figure 6.5a). From 50-65 ^{o}C, a continuous decrease in the absorption maxima of cy3 is observed, indicating a steady release of $KClO_4$ after the wax coating has been removed. Due to the absorbance decrease of cy3, the released $KClO_4$ retains its oxidative ability after storage and delivery, indicating that it has not reacted with the wax coating. Even after cooling, decreasing slope in cy3 absorbance is observed, suggesting once melted, the wax cannot resolidify in a way to prevent cargo release (Figure 6.5a). This is in agreement with observations from the cobalt sample, where release of cobalt was seen even after cooling (Figure 6.4a, 6.5a). The decrease in absorbance at 600 nm due to oxidation of cy3 can be directly related to the growth of a new species at 525 nm (Figure 6.5b). By monitoring the ratiometric decay of the cy3 absorption maxima and growth of the 525 nm peak, we can confirm

this absorption decay is due to change in cy3 concentration and not from solution turbidity from suspended particles and/or wax.

6.4 Summary

In summary, a simple methodology of wax coating S1NP was used to allow for the storage and delivery of both a small metal ion ($cobalt^{2+}$) and a small, strong oxidizer $KClO_4$. Using a two-phased molten wax coating method, a thin, uniform ~5 nm coating of paraffin wax was introduced on S1NP which is hydrophobic enough to prevent cargo escape in an aqueous environment. By heating the coated S1NP over 50 ^{o}C, the wax shell can be melted and its loaded cargo released. Since the wax was comprised of fully saturated long chain hydrocarbons, it was inert towards the storage of strongly oxidizing perchlorate. The delivery of perchlorate was verified through monitoring the absorption change of a solution of cy3 as it is being oxidized by the delivered cargo. Upon its release with heat, the delivered perchlorate retains its oxidizing ability, indicating that the wax coating is chemically inert towards perchlorate. Currently, this system is being adopted onto iron oxide core-shelled nanomaterials, which can be actuated by an oscillating external magnetic field to induce heating directly to the nanoparticle. In this way, wax coated core-shelled nanoparticles can be remotely activated to release their payload on command.

6.5 Experimental

6.5.1 General Comments

All of the chemicals used in this study were used as purchased from major suppliers such as Sigma-Aldrich and Fisher Scientific. Release profiles were generated using a time-resolved fluorescence spectroscopy setup (Figure 6.13). A Coherent 377 nm CUBE laser was used as the probe beam (1-15 mW, 1 mm diameter), and the emission spectra monitored using a 300 nm window monochromator and Princeton Instruments Roper CCD detector cooled to -127 K. Heating was applied using a calibrated hot plate set to heat the sample to 65 ^{o}C at a rate of 2 ^{o}C/min. Powder X-ray diffraction measurements were made using a Panalytical X'Pert Pro diffractometer. TEM images were acquired on a JEM1200-EX microscope. SEM imaging was performed on a JEOL JSM-6700F instrument after sputtering with a ~3 nm thick gold layer. DLS and ZETA potential readings were collected on a ZetaPals DLS and zeta potential instrument. UV-Vis readings were acquired on an Agilent Cary 5000 instrument equipped with a Varian temperature controller. ICP-OES was acquired on a Shimadzu ICPE-9000 instrument in a 5% HNO_3 matrix. TGA readings were done with a heating curve of 2 ^{o}C/min to 200 ^{o}C, holding at 200 ^{o}C for 2 hours to remove surface adsorbed water, and heating at a rate of 3 ^{o}C/min to 500 ^{o}C and holding for 3 hours under air before cooling.

6.5.2 Synthesis of S1NP

Tetraethylorthosilicate (TEOS, 7.5 mL) was added to an aqueous solution of tetrapropylammonium hydroxide (1M, 10 mL) and stirred vigorously for 10 minutes. To this, distilled water was added (2 mL) and stirred until homogenous. The reaction vessel was sealed and stirred for 24 hours at room temperature before transferring to an oil bath maintained at 80 ^{o}C for 48 hours. After the allotted reaction time, the milky solution centrifuged down (1 hour,

15,000 rpm), washed with portions of methanol until washings were of neutral pH, and vacuum dried overnight to isolate silicalite-1 (1.2 g). The product size distribution and crystallinity was characterized using TEM and SEM microscopy, XRD and DLS.

6.5.3 Fluorescence Modification of S1NP

A small portion of the rehydrated S1NP (50 mg) were suspended in toluene (20 mL) distilled over calcium hydride. In a separate reaction flask, fluorescein isothiocyanate (2.5 mg) was dissolved in anhydrous toluene (1.5 mL) before mixing with 3-aminopropyltriethoxysilane (1.87 uL) and reacted under dry nitrogen atmosphere for 2 hours. After the allotted reaction time, the mixture was added to the nanoparticle suspension in toluene, and allowed to react overnight at 80 ^{o}C under a dry nitrogen atmosphere. The fluorescently labeled product was collected through centrifugation (5 min, 15000 RPM), washed with portions of toluene and methanol (2x 2 mL) before vacuum drying. Fluorescein attachment was verified through IR spectroscopy and UV-Vis spectroscopy.

6.5.4 Removal of the Templating Agent

Synthesized silicalite-1 nanoparticles (1 g) were lightly ground before heating to 550 ^{o}C for 3 hours in ceramic crucible at a rate of 2 ^{o}C/min. A steady air stream was applied to the sample during the heating process to ensure adequate oxygen supply. After calcination, the particles were washed with portions of anhydrous methanol (3x 20 mL washes) before drying. Complete removal of the organic template was verified through TGA and FTIR spectroscopy.

6.5.5 Rehydration of the S1NP Surface

Calcinated S1NP (100 mg) were suspended in water (40 mL) before acidifying with concentrated HCl (2.3 mL). The suspension was refluxed for 6 hours before isolating the S1NP via centrifugation (15 min, 15000 RPM). The sample was washed with portions of methanol

until the washings were of neutral pH. Confirmation of surface hydration was done through TGA analysis and TEM imaging.

6.5.6 Loading of Small Cargo

For cobalt loaded S1NP, a small sample of S1NP (10 mg) was suspended in an ethanoic solution of $CoCl_2$ (2 mL, 0.1 M). For $KClO_4$ loaded S1NP, S1NP (10 mg) was suspended in an ethanoic solution of $KClO_4$ (2 mL, 0.1 M) and stirred overnight. After loading, the particles were recollected through centrifugation before vacuum drying.

6.5.7 Coating with Paraffin Wax

A sample of S1NP (10 mg) to be coated with wax was suspended in dichloromethane (1 mL). To a microcentrifuge tube, 1 g of paraffin wax shavings was added and heated to 70 ^{o}C. The nanoparticle suspension was added to the molten wax and sonicated for 15 minutes at 70 ^{o}C where the dichloromethane boiled off. In a separate container, a small amount of water (100 μL) was heated to 60 ^{o}C before pipetting the solution to the bottom of the microcentrifuge tube. After equilibrating, a small amount of brine (400 μL) at 30 ^{o}C was gently added using a needle and syringe to the bottom of the tube before immediately centrifuging (2 min, 15000 RPM). The coated S1NP were washed with portions of water (5x 2 mL) before vacuum drying.

6.5.8 Monitoring Release of Cobalt

Cobalt loaded, wax coated S1NP samples (5 mg) was confined to the corner of a glass cuvette. An aqueous calcein dye solution (4 mL, 0.1 mM) was gently added to the particles at a rate to prevent particles from being resuspended into solution. A 377 nm excitation laser (1 mW) was aimed through the solution supernatant. Emission of calcein dye was monitored in real time by focusing the emitted light through a collecting lens, a 450 nm cutoff filter, and a monochromator (300 nm window) before integrating on a CCD detector (Figure 6.13). Calcein

dye emission was tracked by centering the monochromator window at 500 nm, and integrating the fluorescence emission from 550-580 nm. A baseline was collected over for 20 minutes to allow solution suspended particles to settle before applying a heating curve and initiating cargo release. Due to the quenching effect cobalt ions have on calcein dye (Figure 6.15), the observed fluorescence quenching of calcein was correlated to a release of cobalt.

6.5.9 Monitoring Release of Perchlorate

A small sample of perchlorate loaded, wax coated S1NP (5 mg) was confined to the bottom of a quartz cuvette. To this, an aqueous solution of cy3 (2 mL, 0.1 mM) was gently added to the nanoparticles. An absorption spectrum was collected of this sample from 500-700 nm at ~10 minute intervals to monitor the decay of the cy3 maxima at 600 nm. After collecting baseline absorption over 30 minutes, heat was applied using a water cooled Peltier heater at a rate of 2 ^{o}C/min before maintaining a temperature of 65 ^{o}C for 20 minutes. Absorption readings were acquired at 10 minute intervals for baseline reading, at 2 minute intervals after initial heat application, and at 10 minute intervals upon cooling. Because oxidation of cy3 by $KClO_4$ results in a decay of cy3 absorbance at 600 nm (Figure 6.17), the decay of this peak was correlated to the release of $KClO_4$ from S1NP.

6.5.10 ICP-OES Measurement of Cobalt Release

After complete TRFS monitoring of both heated and non-heated S1NP samples, the solution was collected and centrifuged (30 min, 15000 RPM) to remove suspended S1NP from the supernatant. The collected supernatant was diluted with HNO_3 (4 mL, 10%) and heated at 60 ^{o}C for 24 hours before analysis. Standards were made by serial dilutions from a stock solution of cobalt (1000 ppm, Sigma-Aldrich).

6.6 Figures

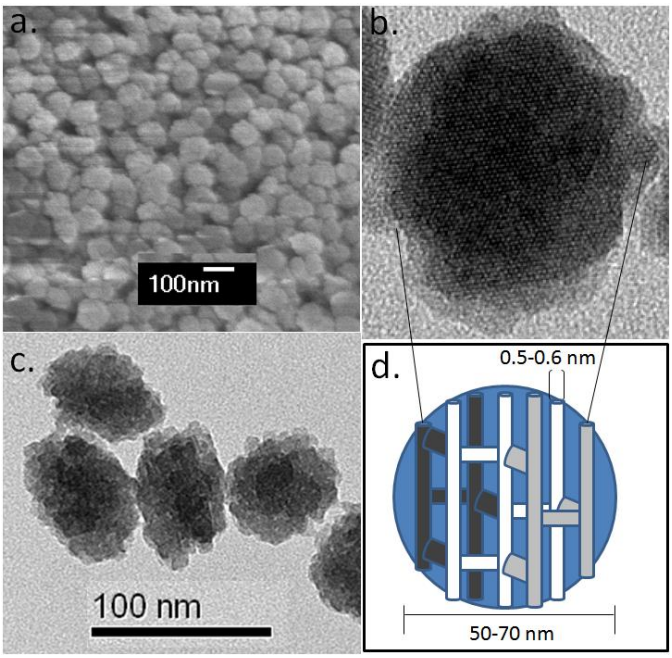

Figure 6.1. (a) SEM image of synthesized S1NP, indicating a narrow size distribution of S1NP. The TEM image (c) of S1NP is in close agreement with SEM data, showing a narrow size distribution of 50-70 nm nanoparticles. (b) Diffraction patterns in the high-resolution TEM image of synthesized S1NP indicates a high level of crystallinity in the sample. This result is supported by XRD (Figure 6.6). (d) Diagram illustrating the 3D zig-zag interconnected pore structure characteristic of S1NP.

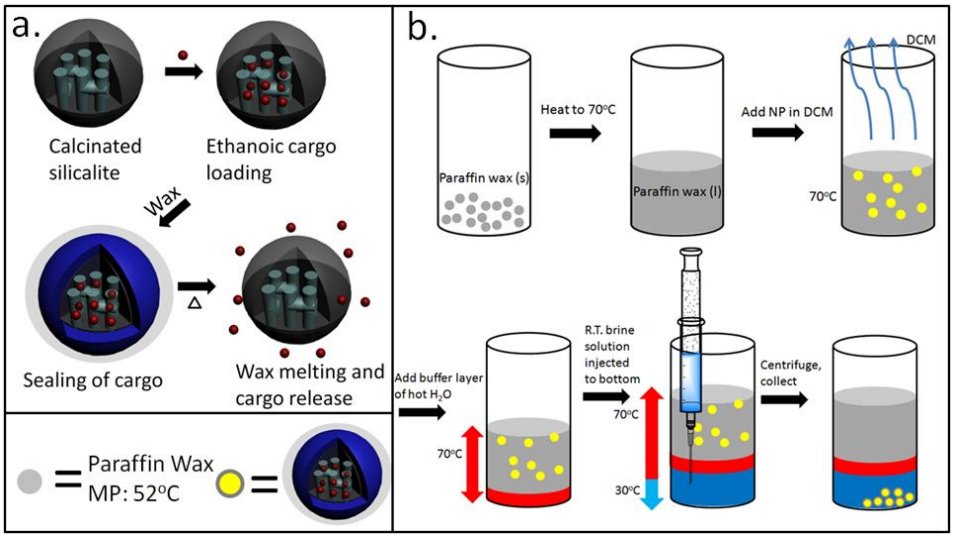

Figure 6.2. (a) Schematic for assembly of cargo loaded, wax coated S1NP. Calcinated S1NP are loaded with cobalt or $KClO_4$ in an ethanoic solution, dried, and coated with paraffin wax. The wax coating prevents cargo leakage until heat is applied, which melts the wax coat and allows the cargo to release. (b) Method for applying the thin wax coating to S1NP. Wax shavings are heated to 70 ^{o}C to form a liquid layer of paraffin wax. S1NP loaded with appropriate cargo are suspended in dichloromethane before adding to the liquid wax. A buffer layer of 60 ^{o}C water is added to the bottom of the microcentrifuge tube before brine at 30 ^{o}C is added to the bottom of the container using a needle and syringe. Centrifuging the S1NP in the molten paraffin wax layer causes the thin wax coat to solidify upon reaching the cold aqueous layer resulting in a thin coating of wax.

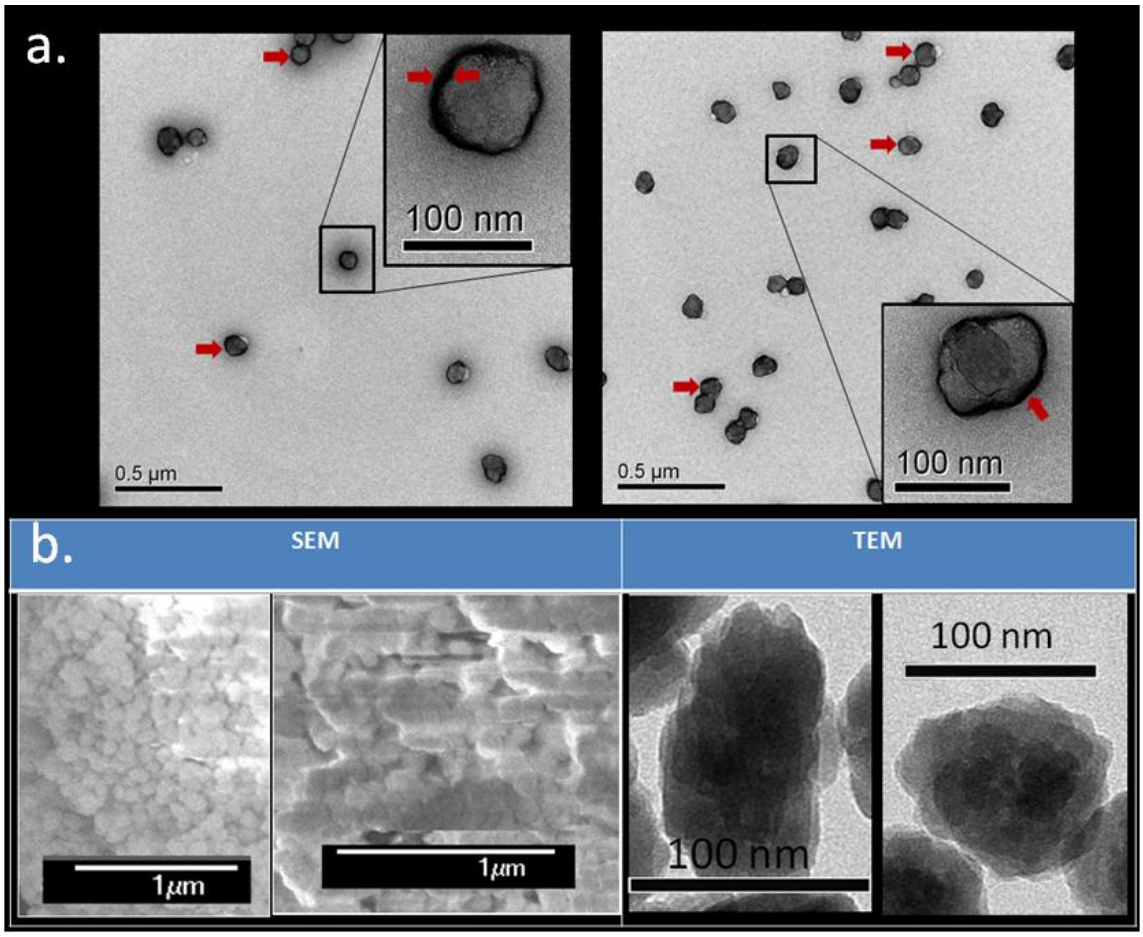

Figure 6.3. (a) TEM imaging of wax coated S1NP stained with a 2% uranyl acetate solution. Compared to a control of uranyl acetate stained S1NP not coated with wax (Figure 6.19), TEM imaging of the coated NP show a high contrast shell around each S1NP. The width of the observed wax coating (3-7 nm) is in close agreement with the calculated 5 nm thickness. (b) TEM and SEM analysis of an unstained sample of S1NP coated with a thin wax layer shows a distinction between a thin wax coating and TEM / SEM imaging of nanoparticles embedded in wax agglomerates (see Figure 6.11).

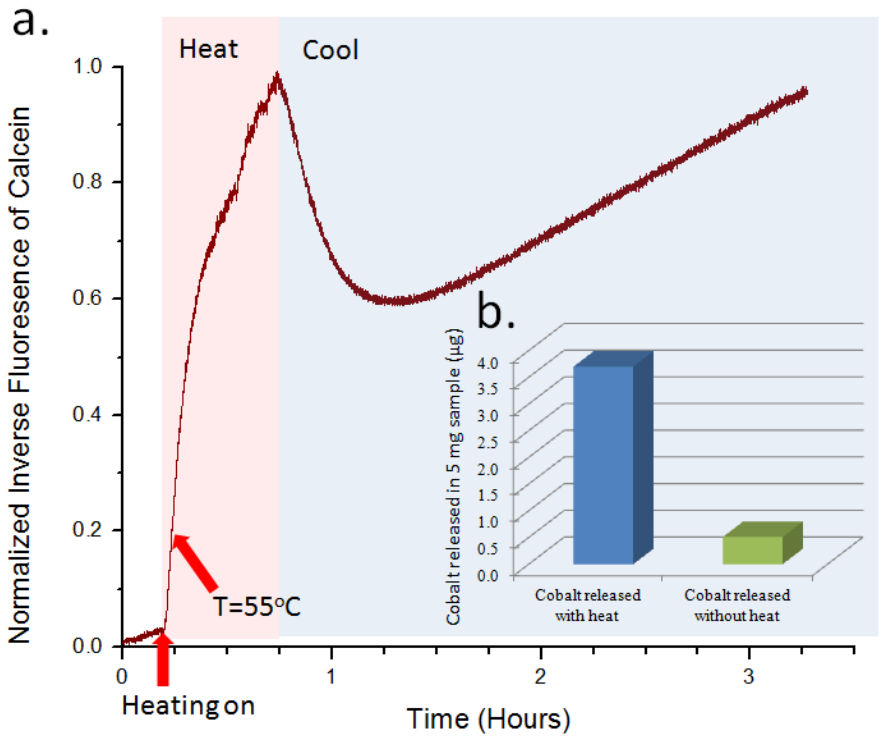

Figure 6.4. (a) Time resolved fluorescence spectra showing the fluorescence quenching of calcein dye as a result of cobalt released from loaded, wax coated S1NP. The relatively flat baseline slope prior to heating indicates that the wax coating is capable of sealing back cobalt ions. After applying heat, a large decrease in calcein fluorescence is observed; this can be correlated as a release of cobalt. This result is corroborated by (b) ICP-OES analysis of the release supernatant, in which significant cobalt release is observed only after heating, indicating that the wax coating must be removed before cargo can be delivered.

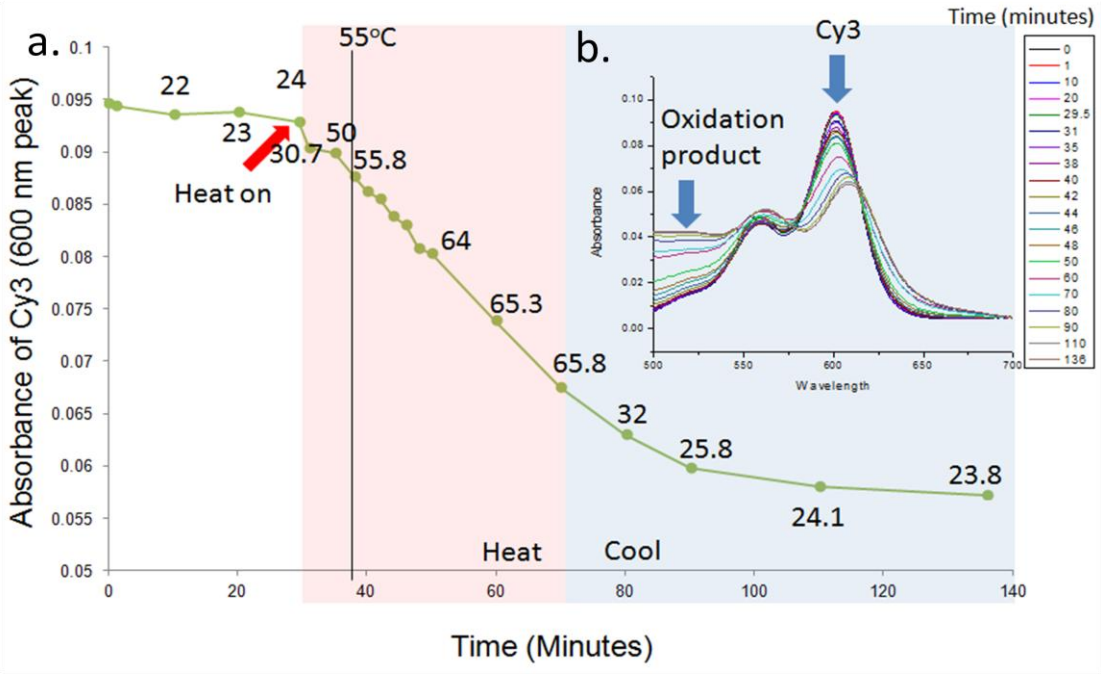

Figure 6.5. (a) Plot of the absorption maxima of cy3 (600 nm) with respect to time monitoring the oxidation of cy3 by $KClO_4$ released from perchlorate loaded, wax coated S1NP. The numbers listed at various points on the trace denote the solution temperature in Celsius. Prior to heating, the absorbance maxima of cy3 remains stable. Upon reaching temperatures >50 ^{o}C, a steady decrease of cy3 absorbance is observed. This decrease in absorbance is evidence for the release of $KClO_4$ from S1NP as a result of melting off the wax coat. (b) The absorption spectra of cy3 showing the decrease of the cy3 peak (600 nm) and the growth of a new species (525 nm) as a result of oxidation.

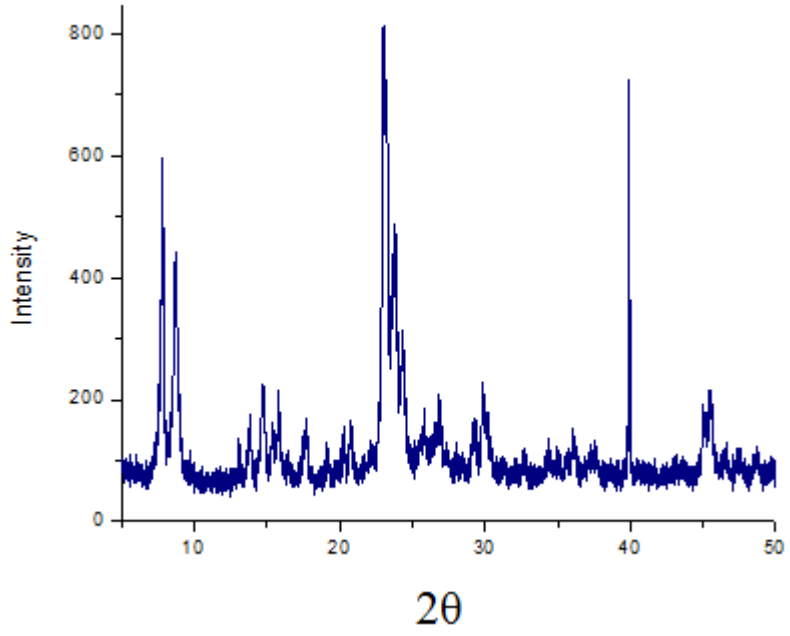

Figure 6.6. XRD of synthesized S1NP indicating high levels of crystallinity, consistent with silicalite-1.

Surface Treatment	DLS In Water	Zeta Potential
None	2081 nm	-1 mV
Calcinated	500 nm	-25 mV
Calcinated, selected	114 nm	-26 mV
Calcinated, selected and rehydrated	80 nm	35 mV
Rehydrated, FITC	99 nm	25 mV

*Samples Aged 3 days in H_2O. No sonication time applied prior to measurement.

Figure 6.7. Hydrodynamic radii and zeta potential of silicalite-1 nanoparticles after surface rehydration treatments.

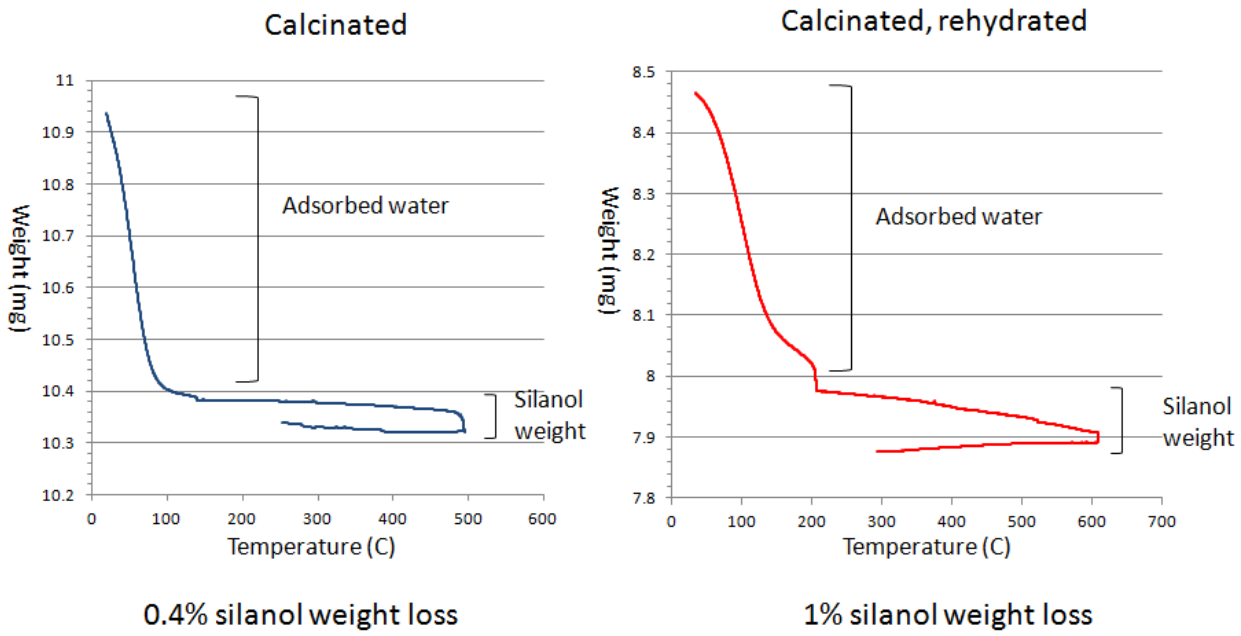

Figure 6.8. TGA curves for calcinated silicalite-1 and rehydrated silicalite-1 showing a ~2x increase in silanol density after rehydration. Rehydration of the surface allows for better dispersibility and loading of cationic small cargo.

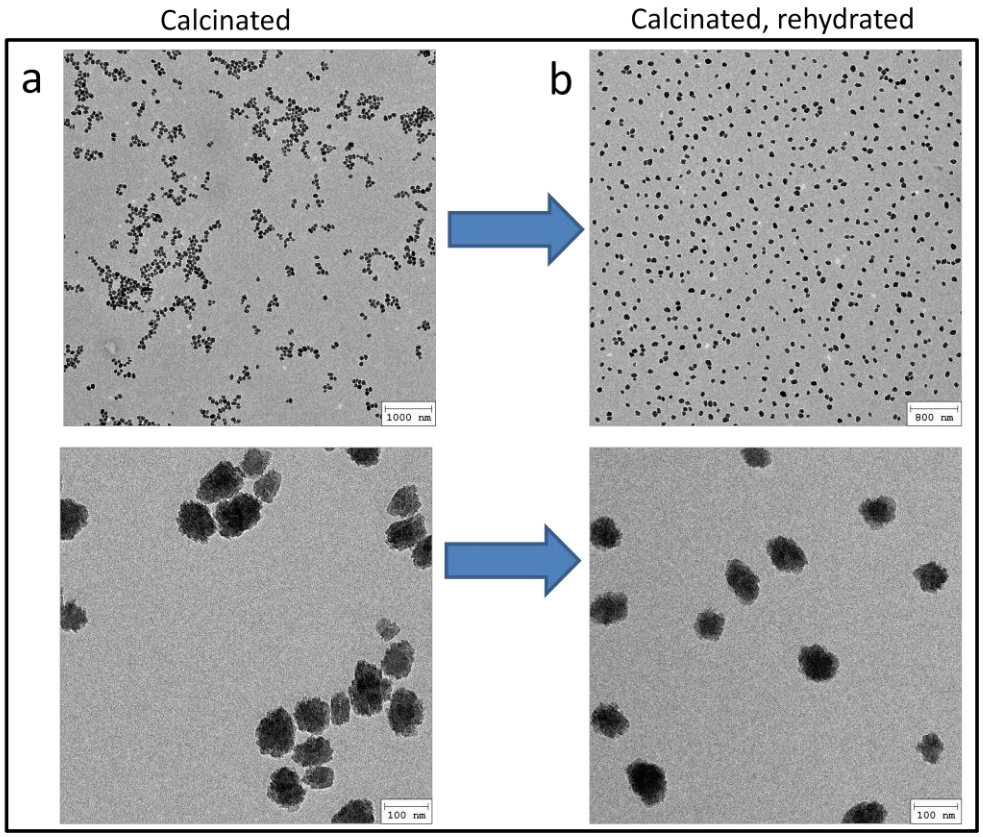

Figure 6.9. TEM image of calcinated S1NP and rehydrated S1NP. Calcinated S1NP are highly aggregated as a result of surface silanol loss. Rehydration of the silicalite surface allows high dispersibility.

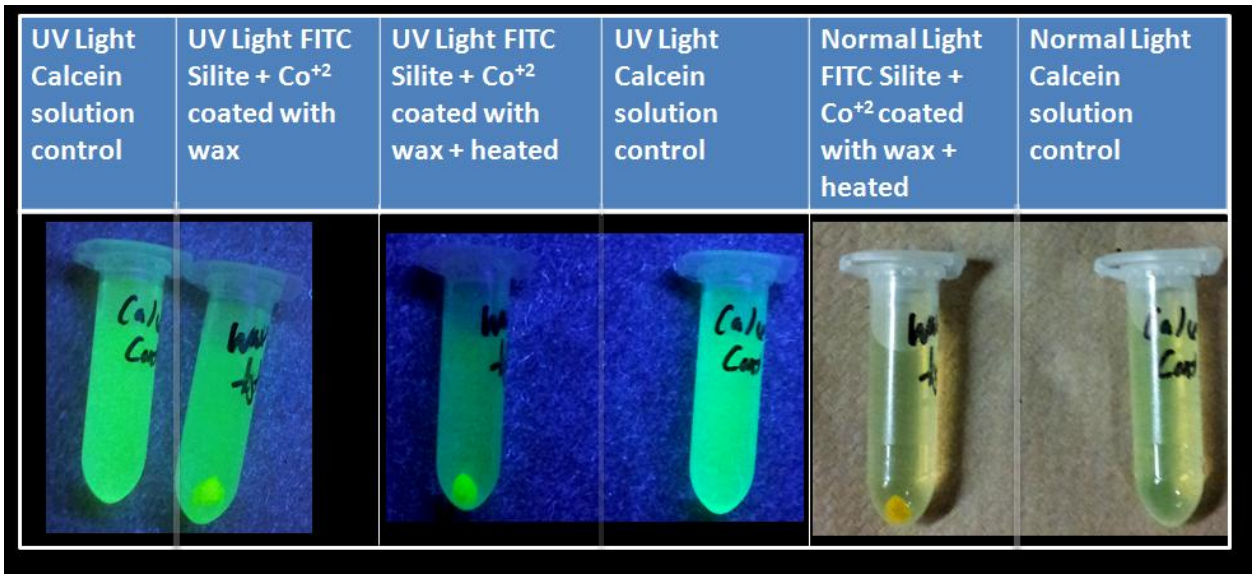

Figure 6.10. Qualitative evidence of the heat activated release of cobalt from cobalt loaded, thin wax coated S1NP. The fluorescence of a control solution of calcein dye is compared to a sample treated with S1NP loaded with cobalt and coated with wax (labeled with fluorescein for easy visual traceability) prior to heating, and after a heating and cooling cycle. In the middle frame, the fluorescence intensity of the calcein solution with the presence of cobalt loaded, wax coated S1NP is noticeably quenched compared to the control. In each frame, images of both samples are from a single image taken under uniform black light irradiation.

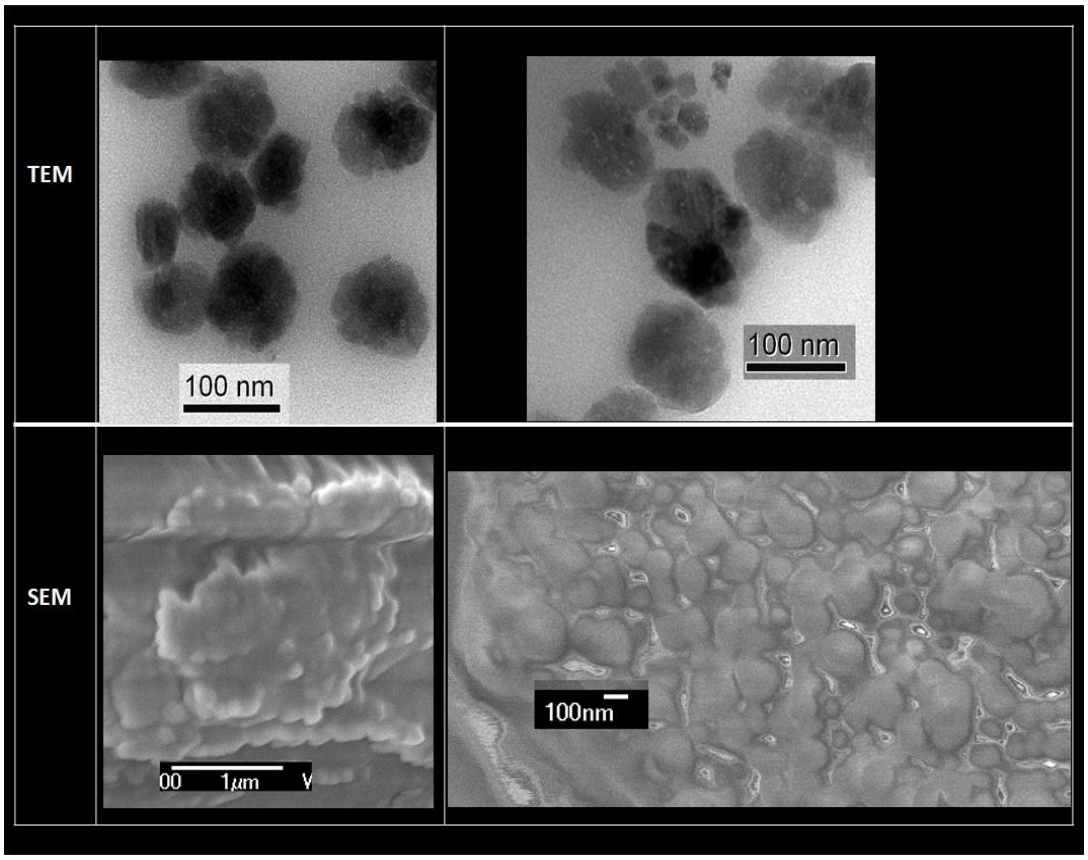

Figure 6.11. TEM / SEM images of a control group of S1NP without contrast agent staining. S1NP were suspended in molten paraffin wax before cooling and grinding the solid wax. Wax chunks were analyzed through TEM and SEM to compared with S1NP nanoparticles coated using the method described in experiment. Dark blurred contrast fringes extending from nanoparticles in TEM suggest the presence of organic material. Large wax agglomerates were observed in the SEM analysis; closer inspection of the wax surface revealed nanoparticles trapped within the wax globs.

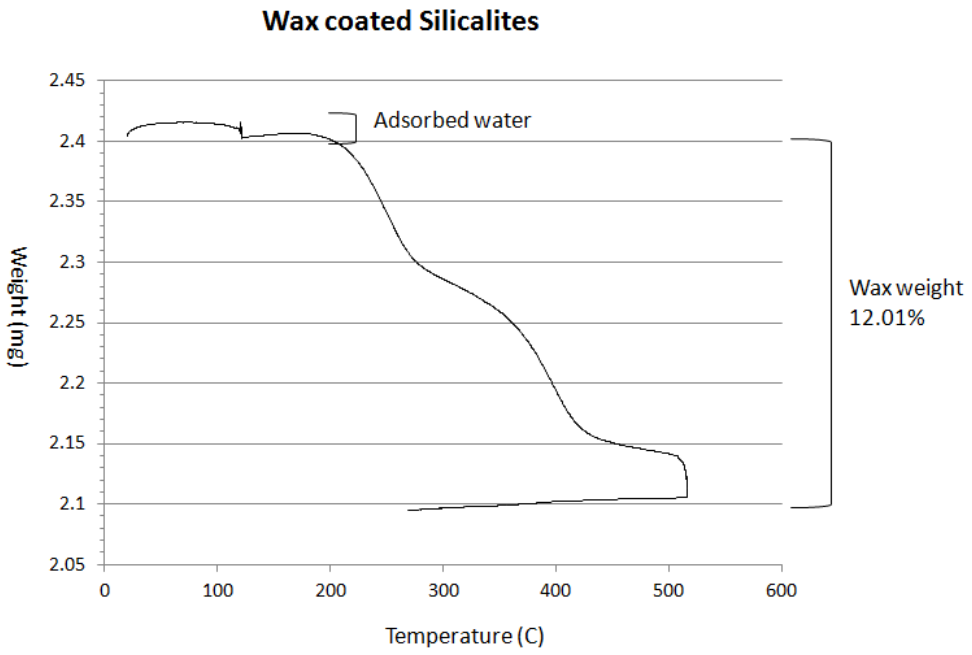

Figure 6.12. TGA analysis of thin wax coated S1NP. A 12% weight loss was observed after heating to 500 ^{o}C for 3 hours before cooling. This 12% weight lost was used to calculate an approximate wax coating thickness of 5 nm (Figure 6.19).

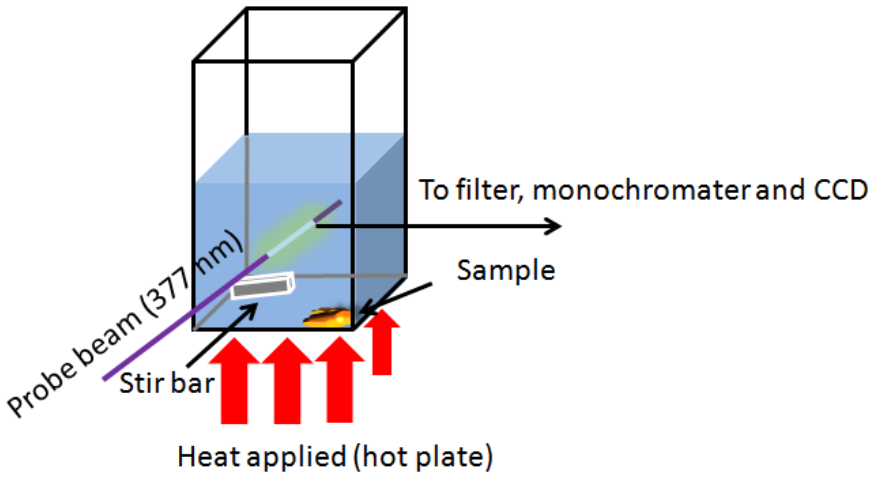

Figure 6.13. Schematic setup for time-resolved fluorescence spectroscopy measurements. An excitation beam is aimed at the solution supernatant, exciting the calcein dye solution. The emission of the dye is focused on a CCD detector cooled to liquid nitrogen temperatures. Integrated intensities are plotted in real-time to generate a typical release profile curve.

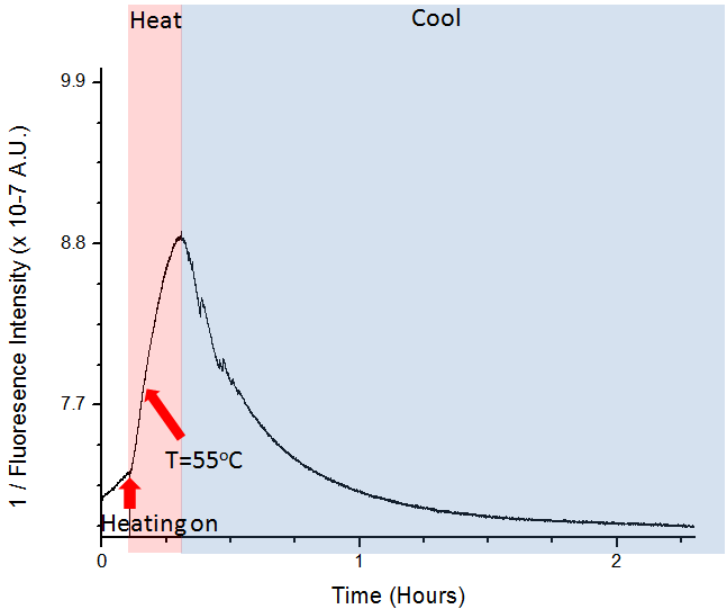

Figure 6.14. Control experiment of calcein dye fluorescence subjected to the same heating curve as used in the sample release experiment. A noticeable decay in fluorescence intensity is observed prior to heating due to photobleaching of the dye. Upon applying heat, the fluorescence intensity of calcein is diminished. However, after cooling, the fluorescence intensity of calcein is regenerated to its baseline value.

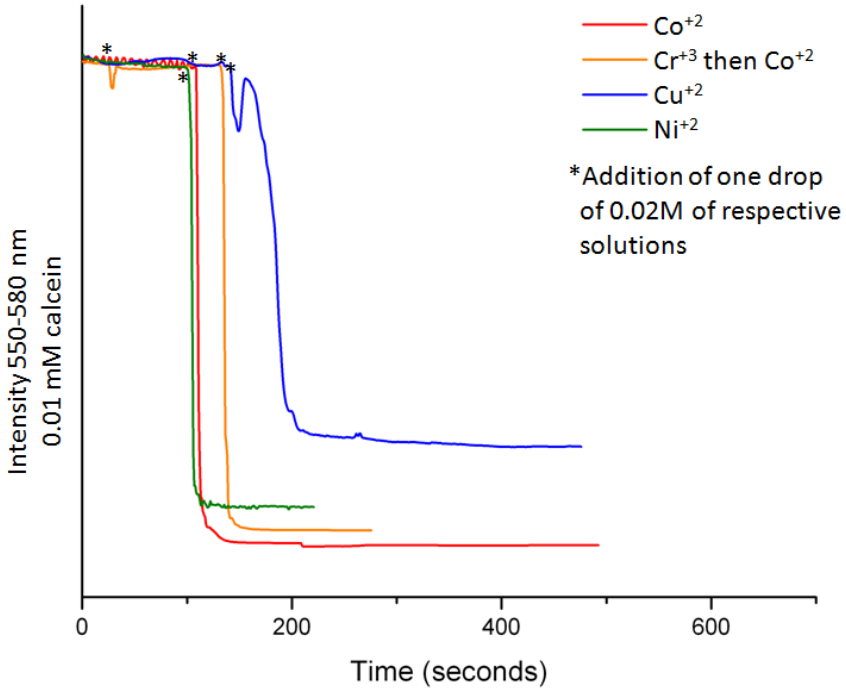

Figure 6.15. Fluoresence quenching of calcein dye with the addition of certain metal ions.

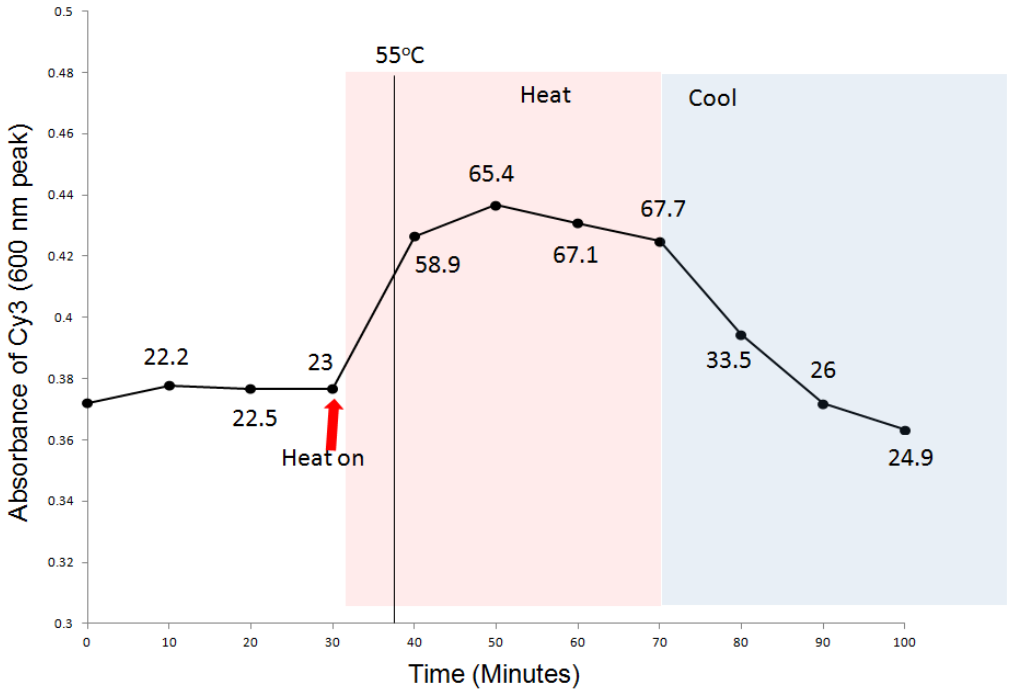

Figure 6.16. Control study of the heat stability of cy3 dye at the same heating curve used in experiment. Upon heating, the absorbance of cy3 increases slightly, but returns back to its original value when cooled back to room temperature.

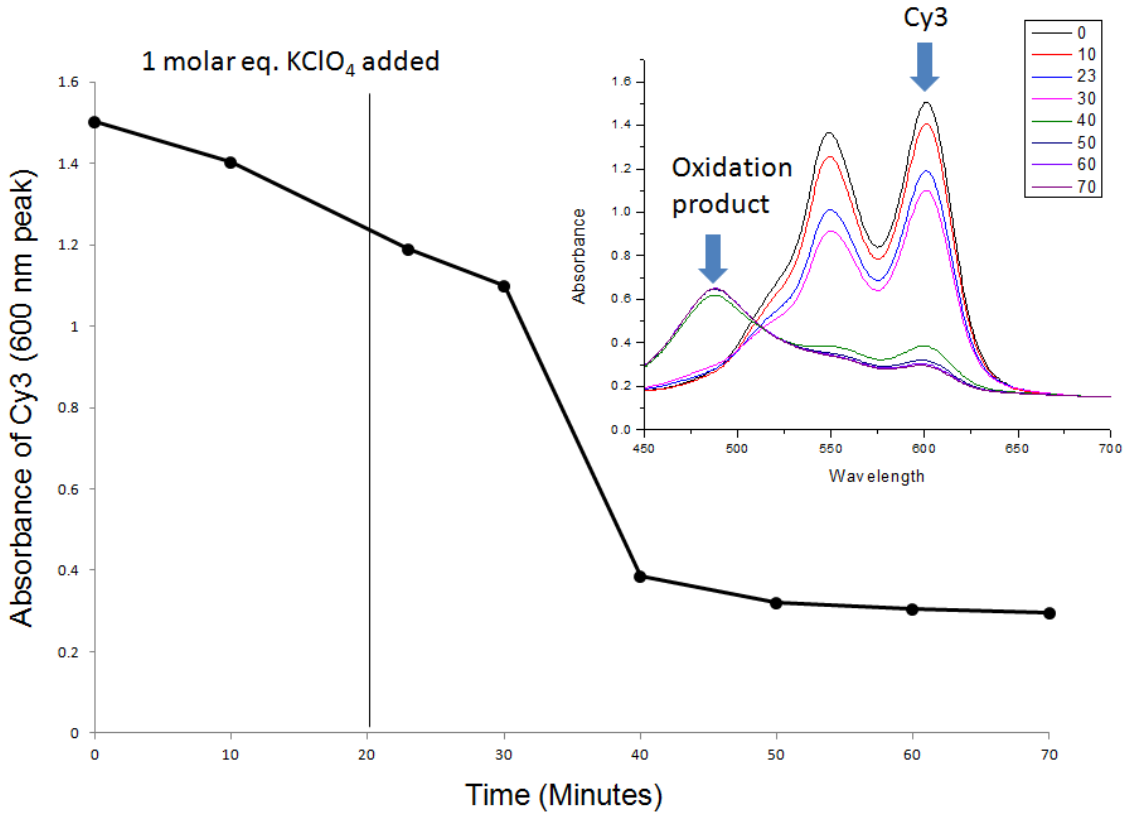

Figure 6.17. Absorbance change of cy3 dye with the addition of $KClO_4$. Upon the addition of perchlorate, a decrease in the absorbance peak of cy3 at 600 nm is observed. This absorbance decay is coupled with an increase in absorbance at 500 nm, corresponding to the generation of the oxidized form of cy3.

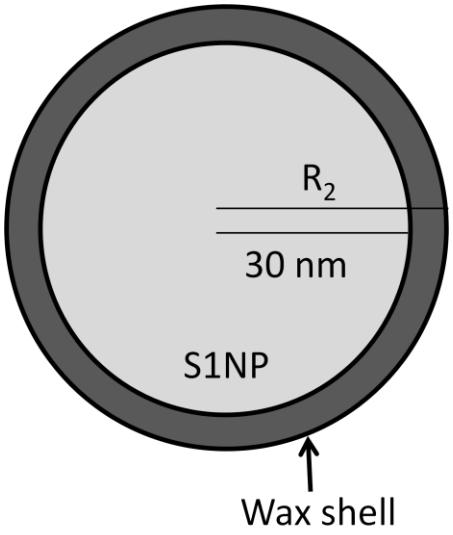

Figure 6.18. Approximation of Wax Thickness

Taking an average size for S1NP as 60 nm (corresponding to a radius of 30 nm), the volume of an individual S1NP particle is 1.13 x 10^{-16} cm^3. The density of silicalite is reported to be 1.76 g/cm^3, (Flanigen, E. M.; Bennett, J. M.; Grose, R. W.; Cohen, J. P.; Patton, R. L.; Kirchner, R. M.; Smith, J. V. *Nature* 1978, 271, 512-516) therefore the weight of an individual S1NP is 1.99 x 10^{-16} g. Because a weight loss of 12% of the total weight of S1NP and wax combined was observed in the TGA, we know that the approximate weight of wax per nanoparticle is 0.27 x 10^{-16} g. Taking the density of the paraffin wax as reported by the company to be 0.781 g / cm^3, this weight corresponds to a wax volume of 0.346 x 10^{-16} cm^3. If we assume that this volume is distributed as a concentric shell around a S1NP, we find that R_2, the radius of the wax coated S1NP, is 32.8 nm. This number corresponds to a total diameter increase of roughly 5 nm from the wax coating.

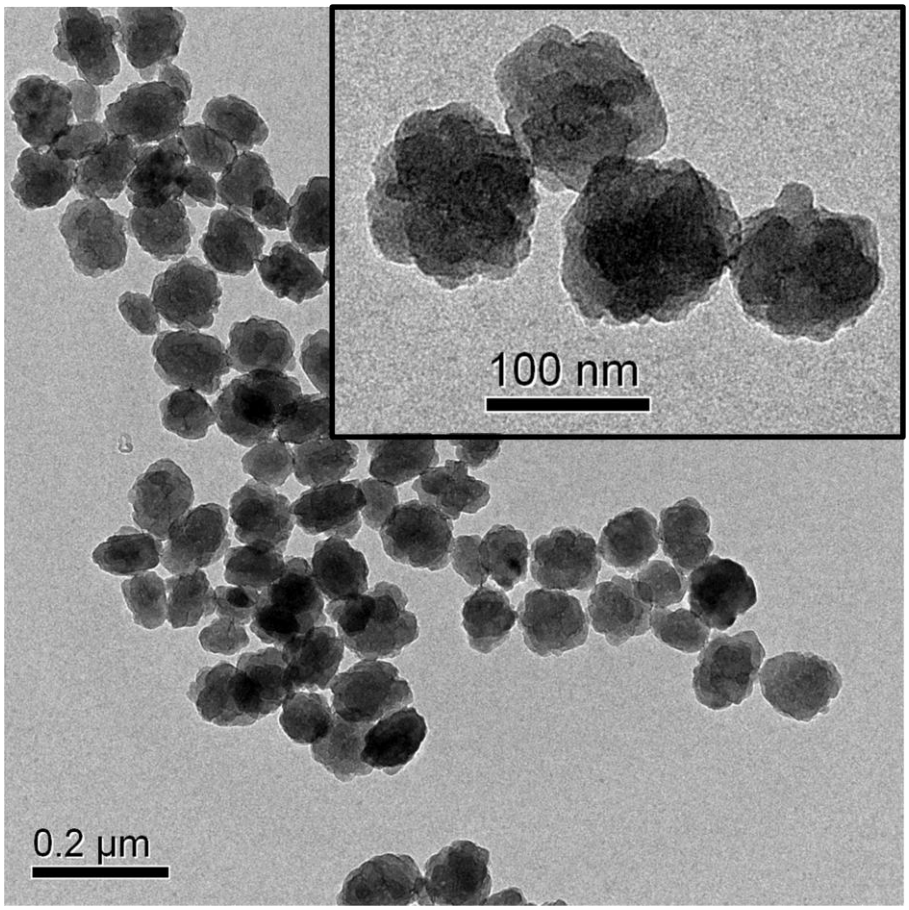

Figure 6.19. TEM images of non-coated S1NP stained with a 2% uranyl acetate solution. When compared to wax coated S1NP, the uncoated sample does not exhibit any high contrast outer shells observed in coated S1NP (Figure 6.3a).

6.7 References

(1) Flanigen, E. M.; Bennett, J. M.; Grose, R. W.; Cohen, J. P.; Patton, R. L.; Kirchner, R. M.; Smith, J. V. *Nature* **1978**, 271, 512-516.

(2) Tassel, P. R. V.; Phillips, J. C.; Davis, H. T.; McCormick, A. V. J. Mol. Graphics 1993, 11, 180−184.

(3) Cundy, C. S.; Cox, P. A. Chem. Rev. 2003, 103, 663−701

(4) S.-Sibbel, G. M. W.; Gjerde, D. T.; Chriswell, C. D.; Fritz, J. S. *Talanta* **1982**, 29, 6, 447-452.

(5) Sing, K. S. W.; Williams, R. T.; *Part. Part. Syst. Charact.* **2004**, 21, 71-79.

(6) Mériaudeau, P.; Thangaraj, A.; Naccache, C. *Microporous Mater.* **1995**, 4, 213-219.

(7) G-Pérez, E.; Schnell, S. K.; Castillo, J. M.; Calero, S.; Kjelstrup, S.; Dubbeldam, D.; Vlugt, T. J. H. *J. Phys. Chem. C.* **2011**, 115, 15355-15360.

(8) Pearce, M. E.; Mai, H. Q.; Lee, N.; Larsen, S. C.; Salem, A. K. *Nanotechnology* **2008**, 19, 175103.

(9) Petushkov, A.; Intra, J.; Graham, J. B.; Larsen, S. C.; Salem, A. K. *Chem. Res. Toxicol.* **2009**, 22, 1359-1368.

(10) Zhang, H.; Dunphy, D. R.; Jiang, X.; Meng, H.; Sun, B.; Tarn, D.; Xue, M.; Wang, X.; Lin, S.; Ji, Z.; Li, R.; Garcia, F. L.; Yang, J.; Kirk, M. L.; Xia, T.; Zink, J. I.; Nel, A.; Brinker, C. J. *J. Am. Chem. Soc.* **2012**, 134, 15790-15804.

(11) Fu, H.; Zhu, D.; *Anal. Chem.* **2012**, 84, 2366-2372.

(12) Kucherenko, I. S.; Soldatkin, O. O.; Kasap, B. O.; Öztürk, S.; Akata, B.; Soldatkin, A. P.; Dzyadevych, S. V. *Electroanalysis* **2012**, 24, 6, 1380-1385.

(13) Bakker, W. J. W.; Kapteijn, F.; Poppe, J.; Moulijn, J. A. *J. Membrane Sci.* **1996**, 117, 57-78.

(14) Groen, J. C.; Peffer, L. A. A.; P.-Ramírez, J. *Microporous Mesoporous Mater.* **2003**, 60, 1-17.

(15) Ravishankar, R.; Kirschhock, C.; Schoeman, B. J.; Vanoppen, P.; Grobet, P. J.; Storck, S.; Maier, W. F.; Martens, J. A.; De Schryver, F. C.; Jacobs, P. A. *J. Phys. Chem. B.* **1998**, 102, 2633-2639.

(16) Tarn, D.; Ashley, C. E.; Xue, M.; Carnes, E. C.; Zink, J. I.; Brinker, C. J. *Accounts* **2013**, 46, 792-801.

(17) Hoffman, A. S. *Adv. Drug Deliv. Rev.* **2012**, 64, 18-23.

(18) Rösler, A.; Vandermeulen, G. W.M.; Klock, H.-A. *Adv. Drug Deliv. Rev.* **2012**, 64, 270-279.

(19) Kataoka, K.; Harada, A.; Nagasaki, Y. *Adv. Drug Deliv. Rev.* **2012**, 64, 37-48.

(20) Orrenius, S.; Zhivotovsky, B.; Nicotera, P. *Nat. Rev. Mol. Cell. Bio.* **2003**, 4, 552-565.

(21) Denkhaus, E.; Salnikow, K. *Crit. Rev. Oncol. Hematol.* **2002**, 42, 35-56.

(22) Young, R. S. *Cobalt in biology and biochemistry***,** Academic Press Inc: London, **1979**.

(23) Mattson, M. P.; Chan, S. L. *Nat. Cell. Biol.* **2003**, 5, 1041-1043.

(24) Xia, T.; Kovochich, M.; Liong, M.; Madler, L.; Gilbert, B.; Shi, H.; Yeh, J. I.; Zink, J. I.; Nel, A. E. *ACS Nano* **2008**, 2, 2121-2134.

(25) Thomas, C. R.; George, S.; Horst, A. M.; Ji, Z.; Miller, R. J.; P.-Videa, J. R.; Xia, T.; Pokhrel, S.; Mädler, L.; G.-Torresdey, J. L.; Holden, P. A.; Keller, A. A.; Lenihan, H. S.; Nel, A. E.; Zink, J. I. *ACS Nano* **2011**, 5, 1, 13-20.

(26) C.-Barraud, C.; Gaubert, A.; Masson, P.; Vidal, D. *Appl. Environ. Microbiol.* **2004**, 70, 1, 635-637.

(27) Raber, E.; Burklund, A. *Appl. Environ. Microbiol.* **2010**, 76, 19, 6631-6638.

(28) Block, S. S. *Disinfection, Sterilization, and Preservation Fifth Edition;* Lippincott Williams and Wilkins: Philadelphia, PA, **2001**.

(29) Klapes, N. A.; Vesley, D. *Appl. Environ. Microbiol.* **1990**, 56, 2, 503-506.

(30) Busche, B.; Wiacek, R.; Davidson, J.; Koonsiripaiboon, V.; Yantasee, W.; Addelman, R. S.; Fryxell, E. G. *Inorg. Chem. Commun.* **2009**, 12, 312-315.

(31) Chouyyok, W.; Shin, Y.; Davidson, J.; Samuels, W.; La Fermina, H. N.; Rutledge, D. R.; Fryxell, G.; Sanvanich, T.; Yantasee, W. *Environ. Sci. Technol.* **2010**, 44, 6390-6395.

(32)Zheng, H.; Huang, Z.; Che, S. *Dalton Trans.* **2012**, 41, 5038

(33) Tarn, D.; Xue, M.; Zink, J. I. *Inorg. Chem.* **2013**, 52, 4, 2044-2049.

(34) Shannon, R. D. *Acta. Cryst.* **1976**, A32, 751-767.

(35) Hiemstra, T.; de Wit, J. C. M.; van Riemsdijk, W. H. *J. Colloid Interface Sci.* **1989**, 133, 105-117.

(36) Smur, R. Q.; Bell, A. T.; Theodorou, D. N. *J. Phys. Chem.* **1993**, 97, 13742-13752.

(37) Portsmouth, R. L.; Gladden, L. F. *J. Chem. Soc. Faraday Trans.***1995**, 91, 963-969.

(38) Thomas, C. R.; Ferris, D. P.; Lee, J-H.; Choi, E.; Cho, M. H.; Kim, E. S.; Stoddart, J. F.; Shin, J-S.; Cheon, J.; Zink, J. I. *J. Am. Chem. Soc.* **2010**, 132, 10623-10625.

(39) Ashley, C. E.; Carnes, E. C.; Phillips, G. K.; Padilla, D.; Durfee, P. N.; Brown, P. A.; Hanna, T. N.; Liu, J.; Phillips, B.; Carter, M. B.; Carroll, N. J.; Jiang, X.; Dunphy, D. R.; Willman, C. L.; Petsev, D. N.; Evans, D. G.; Parikh, A. N.; Chackerian, B.; Wharton, W.; Peabody, D. S.; Brinker, C. J. *Nature Mater.* **2011**, 10, 389-397.

(40) Meng, H.; Xue, M.; Xia, T.; Ji, Z.; Tarn, D. Y.; Zink, J. I.; Nel, A. E.: *ACS Nano* **2011**, *5*, 4131-4144.

(41) Xia, T.; Kovochich, M.; Liong, M.; Meng, H.; Kabehie, S.; George, S.; Zink, J. I.; Nel, A. E. *ACS Nano* **2009**, 3, 10, 3273-3286.

(42) Janes, K. A.; Calvo, P.; Alonso, M. J. *Adv. Drug Deliv. Rev.* **2001**, 47, 83-97.

(43) Branham, W. S.; Melvin, C. D.; Han, T.; Desai, V. G.; Moland, C. L.; Scully, A. T.; Fuscoe, J. C. *BMC Biotechnol.* **2007**, 7-8.

(44) Byers, G. W.; Gross, S.; Henrichs, P. M. *Photochem. Photobiol.* **1976**, 23, 37-43.